McGill University

Master's Thesis

Search for Gamma-ray and Optical Counterparts to FRBs using VERITAS

Author:
Matthew William Arthur Lundy

Supervisor:
Kenneth Ragan

A thesis submitted to McGill Unviersity in partial fulfillment of the requirements for the degree of Master of Science

Physics Department

Montreal, Quebec

CANADA

December 16, 2020

"As soon as you're sure you're right, there's no point in your being here."

Neal Stephenson, Anathem

Abstract

Many mysterious sources still exist within the realm of transient astronomy. As detectors across the electromagnetic spectrum continue to improve, new parameter spaces continue to open. Within these parameter spaces, many new source classes have appeared including the class of Fast Radio Bursts, or FRBs. These rapid bursts of extragalactic radio emission have been seen for over a decade, but the new CHIME telescope has caused the number of detected FRBs to increase by over an order of magnitude in just the past couple of years. This has allowed for novel opportunities to follow-up on these sources with other telescopes. Although many theories have been developed to try and explain these sources, the lack of solid counterparts in other wavelength bands has caused a complete explanation to remain elusive. The energetic nature of these sources suggests that two wavelength bands may be the ideal place to search. Observations of this emission, or lack thereof, in the optical and gamma-ray space serve as powerful tools to distinguish amongst these models. Due to independent development of a new backend, the Very Energetic Radiation Imaging Telescope (VERITAS) now has the capability to probe both domains simultaneously and has been running a campaign to observe FRBs for the past 4 years. In this thesis, the development of the software analysis systems and the early results of this observation campaign will be summarized. Specifically, observations of both repeating and periodic FRBs observed simultaneously with CHIME will be presented. Across all these observations there exists a persistent non-detection in both wavelength bands. The implications of this and how future observations may seek to improve these results will also be discussed.

Résumé

De nombreuses sources mystérieuses existent encore dans le domaine de l'astronomie transitoire. Alors que les détecteurs continuent à s'améliorer, de nouveaux espaces de paramètres continuent à s'ouvrir. Dans ces espaces de paramètres, de nombreuses nouvelles classes de sources sont apparues, notamment la classe des "Fast Radio Bursts", ou FRB. Ces salves rapides d'émissions radio extragalactiques sont observées depuis plus d'une décennie, mais le nouveau télescope CHIME a fait augmenter le nombre de FRB détectés de plus d'un ordre de grandeur. Cela a permis de nouvelles possibilités de suivre ces sources avec d'autres télescopes. Bien que de nombreuses théories soient apparues pour tenter d'expliquer ces sources, l'absence d'homologues solides dans d'autres bandes de longueurs d'onde a fait qu'une explication complète reste insaisissable. La nature énergique de ces sources suggère que deux bandes de longueurs d'onde pourraient être les endroits idéaux pour effectuer des recherches. L'émission, ou l'absence d'émission, dans les rayons optiques et gamma sont des outils puissants qui permettent de faire la distinction entre ces modèles. Grâce au développement indépendant d'un nouveau "backend", le Very Energetic Radiation Imaging Telescope (VERITAS), a maintenant la capacité de sonder les deux domaines simultanément et a mené une campagne d'observation des FRB depuis 4 ans. Dans cette thèse, le développement des systèmes d'analyse du logiciel et les résultats de cette campagne d'observation seront résumés. Plus précisément, les observations des FRB répétitives et périodiques observées simultanément avec CHIME seront présentées. Parmi toutes ces observations, il existe une non-détection persistante dans les deux bandes de longueur d'onde. Les implications de cette situation et la manière dont les observations futures pourraient améliorer ces résultats seront également discutées.

Statement of Original Contributions

The author, during their time as a M.Sc. student, has provided several individual contributions with regards to both the development of the Enhanced Current Monitor (ECM) and the analysis of the Fast Radio Burst data. Some of the author's contributions include:

- The FRB campaign, including the source selection, scheduling, and other administrative tasks had the author heavily involved.
- The software development for the analysis of the ECM was developed by the author independently. This also includes numerous data quality monitoring tasks to ensure that the data remained usable throughout the course of the campaign. Strategies and techniques to quantify systematic errors are also a product of the author's individual contributions. These contributions are included in Chapter 3.
- The statistical assessment of burst significances required supplemental codes, developed by the author, to work off the output of the scripts developed previously by the VERITAS collaboration (VEGAS). This includes all of the results and interpretation in Chapters 4 and Chapters 5.
- Multiple on-site trips were also undertaken by the author and some of the data in the paper was collected by the author. The trips also involved ensuring the overall functioning and operation of the VERITAS telescopes.
- The author is also actively involved in completing the analysis for numerous other projects in the collaboration not included in this thesis. These projects include (but are not limited to): OJ 287 analysis, HESS J0632+057, dark matter subhaloes, and bowshocks (the final two have the author as the PI).

Acknowledgements

I would like to thank my supervisor Ken Ragan for his tireless support even through my many diversions. It was his guidance that really helped to create this project and push it into a place from which this thesis could be created. My mother and father for housing me while I was unable to leave the house and in whose home I wrote most of this document. I would also like to thank my sister, for giving up her laptop in my time of need. Since my old laptop had a broken screen, there would have been many more typos in this document if she did not help. I would like to thank Micheal Daniels for his invaluable contribution to the development of the ECM and keeping the telescopes running. Jamie Holder for his comments and time to help complement this project. Greg Foote for his work behind and in front of the scenes. The VERITAS collaboration also deserves much thanks for maintaining a community of active and excited individuals who helped promote this project. I would also like to thank the many members of the CHIME collaboration whose knowledge and expertise on this topic helped immeasurably. I would also like the thank the many postdocs who helped me along my path of becoming a useful member: Ben Zitzer, Ste O' Brien, and Sajan Kumar. The other VERITAS graduate students were also of great assistance specifically the assistance of Tony Lin who though he may have mocked the astronomy part of the project, still provided assistance.

Contents

List of Figures

List of Tables

List of Abbreviations

AGN	**A**ctive **G**alactic **N**uclei
CCD	**C**harge **C**oupled **D**evice
CHIME	**C**anadian **H**ydrogen **I**ntensity **M**apping **E**xperiment
CTA	**C**herenkov **T**elescope **A**rray
DACQ	**D**ata **ACQ**uisition system
DM	**D**ispersion **M**easure
ECM	**E**nchanced **C**urrent **M**onitor
FADC	**F**lash **A**nalog-to-**D**igital-**C**onverters
FFT	**F**ast **F**ourier **T**ransform
FOV	**F**ield **O**f **V**iew
FPGA	**F**ield **P**rogrammable **G**ate **A**rray
FRB	**F**ast **R**adio **B**ursts
GRB	**G**amma-**R**ay **B**urst
HE	**H**igh **E**nergy (Roughly 100 MeV to 100 GeV)
HV	**H**igh **V**oltage
HESS	**H**igh **E**nergy **S**tereoscopic **S**ystem
IACT	**I**maging **A**tmospheric **C**erenkov **T**elescope
LAT	**L**arge **A**rea **T**elescope
LED	**L**ight **E**mitting **D**iode
LC	**L**ight **C**urve
MAGIC	**M**ajor **A**tmospheric **G**amma **I**maging **C**herenkov **T**elescopes
NSB	**N**ight **S**ky **B**ackground
PMT	**P**hoto**M**ultiplier **T**ube
SGR	**S**oft **G**amma-ray **R**epeater
SNR	**S**ignal to **N**oise **R**atio
VERITAS	**V**ery **E**nergetic **R**adiation **I**maging **T**elescope **A**rray **S**ystem
VHE	**V**ery **H**igh **E**nergy (Roughly 100 GeV to 100 TeV)

Chapter 1

Introduction

Some of the earliest records of the study of astrophysics come from the investigation of optical transients. Records as early as 48 BCE show nova being recorded by ancient Chinese astronomers (Göttgens et al., 2019). Through the development of more sophisticated techniques over the centuries, we has come to understand the origin of many of these phenomena. Many of these optical transients have now been associated with a broad suite of different astrophysical phenomena, and investigating them has provided key insights to fundamental physics. Just recently, in the field of high energy physics key insights on origins of the elements have arisen from supernovae (The LIGO Scientific Collaboration et al., 2019), the origin of the highest energy cosmic rays have been tied to the flaring of a blazar (Ansoldi et al., 2018), and gravitational waves have been tied to a neutron star merger (Abbott et al., 2017). To this day, some of the largest projects in astronomy are targeted around the investigation of optical transients and as we continue to explore different parameter spaces within the field, new

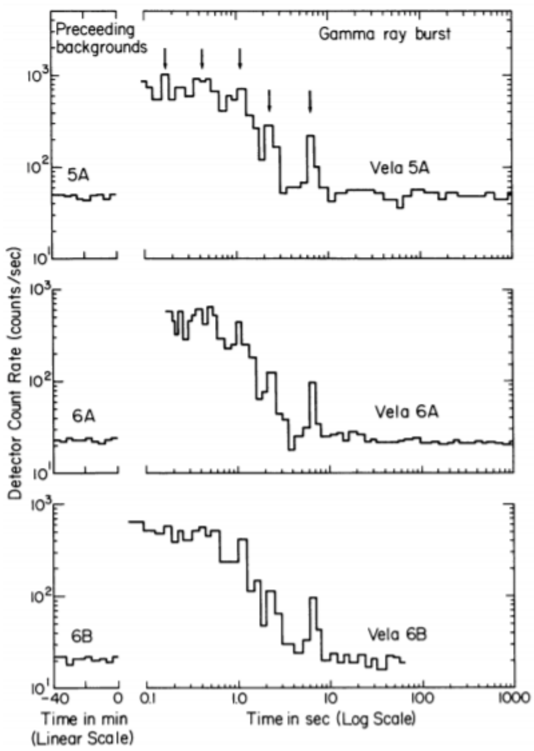

FIGURE 1.1: The original observation of a GRB from three Vela spacecrafts on August 22 1970. The plot shows the count rate over time, with the background count rate shown prior to the burst. Arrows highlight structures common in all three instruments. Figure is taken from (Klebesadel et al., 1973).

scientific questions continue to emerge. Looking to the future it appears as if optical transients will continue to dominate much of the field; the Vera Rubin Observatory has been specifically designed as a large field of view survey telescope with the expressed purpose of providing a deeper study of the classes of optical transients that we know well (Ivezić et al., 2019).

Gamma-ray transients have a much more recent history, although equally impressive. The advent of space-based instrumentation allowed for such detectors as Vela-X to leave the confines of the atmosphere and be exposed to high-energy radiation from space. With it came the first mystery of the field, a brief second-long gamma-ray burst (GRB) coming from the direction of extra-solar space (Klebesadel et al., 1973). These original observations can be seen in Figure 1.1. Our understanding of the origin of GRBs has advanced greatly in recent decades with many GRBs being associated with supernovae. Transients of other durations have also emerged, ranging from month-long flaring accretion events from active galactic nuclei to sub-second bursting events from pulsar systems (Abdollahi, Ackermann, et al., 2017). However, the progenitors of many gamma-ray sources remain illusive. The most complete catalog of known gamma-ray emitting sources is the 4FGL catalog from the Fermi-LAT satellite (Abdollahi, Acero, et al., 2020). Out of 5064 LAT sources in 4FGL, 1336 are unassociated, which represents $\sim$26.4% of the catalog. Some of these sources are not associated with a multiwavelength counterpart due to incomplete follow-up campaigns, but with such a large fraction the potential for many new source classes remain. The distribution of these sources across the sky can be seen in the projection shown in Figure 1.2. Fermi-LAT observes in the energy range $\sim$10 MeV to 100 GeV, which is typically referred to as the high energy range (HE). When we move to very high energies (VHE$\sim$100 GeV-100 TeV), the gamma-ray catalog dwindles even further. Due to the limited field of view of the instruments of the highest sensitivity that can measure photons in this range, the ability to conduct all sky surveys becomes untenable. Low-sensitivity survey can be conducted with water based detectors but only a small fraction of the sky has been probed with deep exposures, leaving the potential for many new VHE sources to be discovered in the next decade.

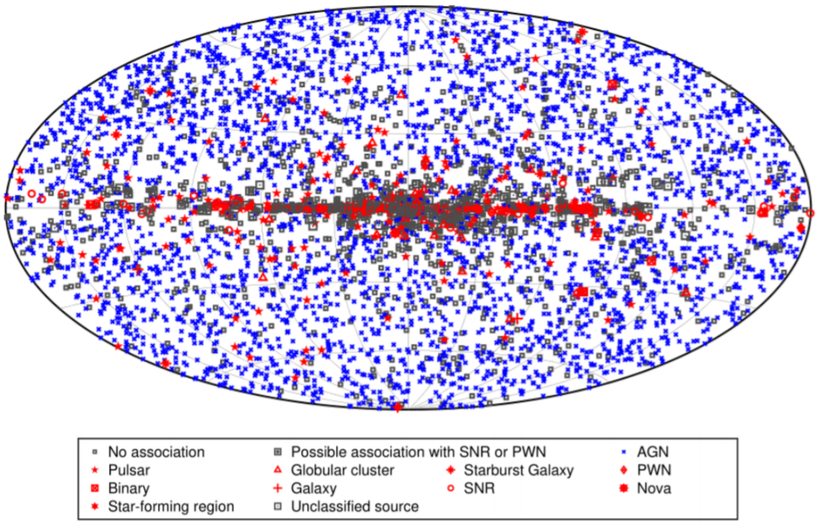

FIGURE 1.2: The positional information of the 4FGL projected into the galactic coordinate reference frame (Abdollahi, Acero, et al., 2020).

Although these wavelength bands, the optical and the gamma-ray, have a differing history, in this thesis we hope that through modern instrumentation we can bridge the gap between the two and demonstrate the use of joint optical/gamma-ray observations with a single instrument, the Very Energetic Radiation Imaging Array System. Modern upgrades to this telescope have allowed for the creation of a complementary independent backend of optical data out of a traditionally gamma-ray based instrument which has opened up a new window to probe rapid transient phenomena. In this thesis, and with this tool, we will search for multi-wavelength counterparts to Fast Radio Bursts, a 21st century transient source class whose progenitors remain elusive (see Petroff, Hessels, et al. (2019) for a review). We will place some of the most competitive limits on a variety of the most well-studied periodic and repeating FRBs, as well as outlining how potential future surveys of these objects can improve upon this search.

1.1 Fast Radio Bursts

Fast radio bursts are short extra-galactic bursts of radio emission that occur at a high rate across the entire sky. In this section, several important properties of FRBs will be highlighted. A brief history, and the status of the FRB field will also be presented. At the time of writing, there exist just over 100 individual bursts published (Petroff, Barr, et al., 2016).

The earliest bursts that began the study of FRBs were discovered by Duncan Lorimer and his colleagues using the 64-m Parkes radio telescope (Lorimer et al., 2007).[1] The properties of this burst have been used to define the class of objects known as FRBs. It was rapid, with the pulse itself lasting less than 50 ms. It was also very bright, with the flux in one beam reaching ∼30 Jy. It also carried a sweeping frequency (ν^{-2}) dependence in arrival time. This is due to a propagation effect seen in FRBs known as dispersion.

The quantity which is used to measure dispersion is the dispersion measure (DM). DM scales with the integrated electron density between the observer and the source. The refractive index of a plasma (like that in interstellar medium) is frequency dependent, with low energy radio waves experiencing a higher refractive index than the higher energy photons. This causes a delayed arrival time of the low energy photons that scales with distance (since travelling through a larger volume of plasma will increase the delay). To quantify this effect DM can be defined as:

$$\mathrm{DM} = \int_0^d n_e \mathrm{d}l, \tag{1.1}$$

with n_e being the number density of electrons along the path whose length is defined as d. One may expect the units of path length to be defined like a common column density (cm^{-2}) however the conventional units for DM are pc cm^{-3} (which is the column density scaled by a factor). This pseudo CGS unit is easier to implement when converting DM into a distance estimate by making an assumption about the extra-galactic electron density. DM can indirectly be measured by the time delay between different frequencies. This is given by

$$t_d = \frac{e^2}{2\pi m_e c} \frac{\mathrm{DM}}{\nu^2}, \tag{1.2}$$

[1]The author would like to give a brief aside to perytons. Perytons were millisecond duration transients also observed at the Parkes radio telescope as early as 1998. They showed many similarities to the early FRBs in terms of duration (∼250 ms) and apparent DM (clustering within 10% of the Lorimer Burst). However, after about 25 perytons were discovered, they noted a temporal clustering on weekdays (a stubbornly non-astrophysical concept). The fact that these were only seen at the one radio telescope was also a cause for concern. A study of the surrounding area revealed that observers were able to replicate perytons in their data using the on-site microwaves. The fact that Parkes was also the site of the earliest FRB observations was a cause for concern, but now FRBs have been solidly confirmed to be of astrophysical and not of kitchen-appliance based origins (Petroff, Keane, et al., 2015).

$$t_d \approx 4140 \left(\frac{DM}{\text{cm}^{-3}\text{pc}}\right) \left(\frac{\nu}{1\ \text{MHz}}\right)^{-2} \text{sec}, \tag{1.3}$$

with m_e being the mass of the electron, c being the speed of light, and e being the charge of the electron. This ν^{-2} dependence leads to the characteristic sweep seen in frequency/time plots. These plots are referred to as "waterfall plots" in the pulsar field, an assortment of which can be seen in Figure 1.3. All of these plots show the characteristic FRB sweep that is not seen in local pulsars (which would appear as vertical line in the above plot) as those pulses do not typically travel an extra-galactic distance as compared to FRBs. For context, the DM of the Lorimer burst was measure to be ~ 375 pc cm^{-3}. Early measurements of DM were the best evidence that FRBs originated from extra-galactic sources. Large dispersion measures either mean that the plasma surrounding the source is very dense, or that the system is located at a large distance (both of these scenarios have an equivalent integrated electron density).

This great extra-galactic distance was not confirmed until the discovery of FRB 121102. Before FRB 121102, it was very difficult to localize FRBs to a host galaxy. If one could localize an FRB to a host galaxy, then one could break the degeneracy in the contributions to the DM from having a dense local medium and being at a large distance. FRBs left no apparent afterglow, and the pulse itself was so rapid that follow-up observations appeared difficult for modern instruments. Most FRBs were also identified through archival searches, which rendered follow-up searches even more challenging. FRB 121102 changed this because multiple FRB pulses appeared from the same sky location and with the same DM. The source appeared to sporadically repeat. This lead to the moniker "the repeater" for FRB 121102. The repeater allowed for many radio telescopes to follow-up the same FRB source and cross-correlate burst properties of a single source. This also allowed for interferometric observations of an FRB (which did not previously occur since these instruments have small FOVs), which led to the localization of FRB 121102 to a host galaxy (a low metallicity dwarf galaxy at $z \approx 0.19$), which confirmed the extra-galactic nature of FRBs.

Although there existed great interest in these bursts, the decade from 2007-2017

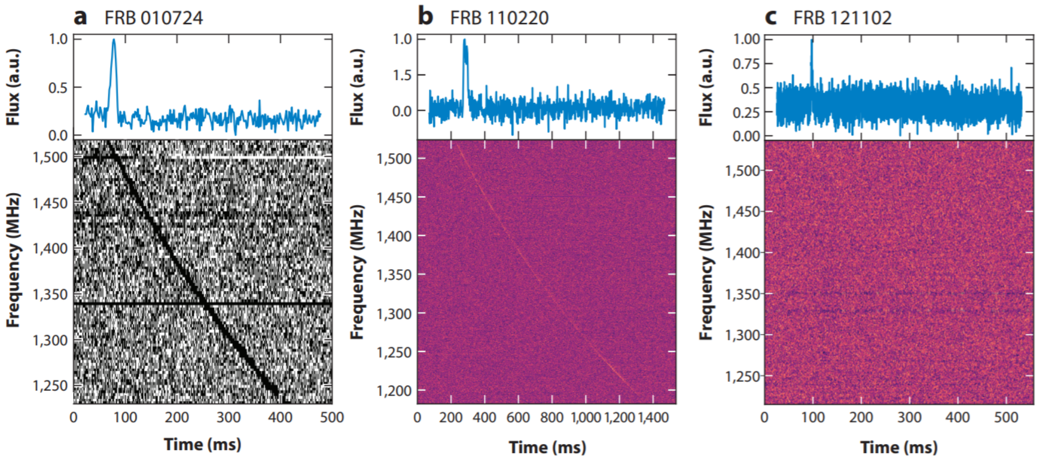

FIGURE 1.3: Figure taken from Cordes et al. (2019) and containing data from Lorimer et al. (2007), Thornton et al. (2013), and Spitler et al. (2014). Shown are the dynamic spectra for a series of FRBs. This style of plots is referred to as "waterfall" plots. The top panel shows the de-dispersed pulse (after applying the correction for the time delay and integrating along the frequency axis). The bottom figure, the time-frequency plane, shows the characteristic sweep of an FRB signal. *a)* FRB010724 is the first observed fast radio burst. *b)* FRB 110220 is a Parkes observed radio burst that helped to confirm the astrophysical nature of FRBs. *c)* FRB 121102 is the first repeating FRB discovered.

was quite slow in expanding the population of FRBs, mostly driven by single dish radio telescopes (like the aforementioned Parkes telescope which dominated the field in the early years) and pulsar detection pipelines. The small FOV of many of these instruments meant that only small part of the sky was being monitored for FRBs at any given time. If one calculated an all-sky FRB rate (at the Parkes frequency), one would find that the all-sky rate of detectable FRBs should be $\sim 3.3 \times 10^3$ events per day (Crawford et al., 2016). What future surveys needed was an expanded FOV and more dedicated time with an active FRB detection pipeline.

One telescope became a clear candidate for modifications, the Canadian Hydrogen Intensity Mapping Experiment, or CHIME (Amiri, K. Bandura, Berger, et al., 2018). As its name suggests, CHIME was originally designed as a cosmology mapping experiment, however it also contained the necessary properties for becoming an FRB telescope. CHIME is composed of four antennas which are made of 1024 dual-polarization radio receivers placed over four 100 x 20 meter^2 cylindrical parabolic reflectors. This can be seen in Figure 1.4. CHIME is a drift scan telescope, which means that the instrument has minimal pointing. Instead, it only observes the region around the local zenith using the earth's rotation to survey a large region of

FIGURE 1.4: A photograph of the CHIME telescope, from (Amiri, K. Bandura, Berger, et al., 2018). The large cylindrical dishes can clearly be seen, as well as the FRB backend stored in the adjacent white shipping containers.

the sky. Its FOV is effectively greater than 200 square-degrees. The only modification required for the telescope to become an FRB detector was a powerful computer backend for the real time analysis of the beams. This would allow CHIME to monitor FRBs in real time over a large swath of sky, and instead of dozens of FRB detections in a decade, estimates showed that CHIME should be able to detect dozens of FRBs in a week (Amiri, K. Bandura, Bhardwaj, Boubel, Boyce, Boyle, Brar, et al., 2019b).

After CHIME began its commissioning it rapidly discovered 13 single burst FRBs (Amiri, K. Bandura, Bhardwaj, Boubel, Boyce, Boyle, Brar, et al., 2019b), followed by the discovery of a second source of repeating FRBs (Amiri, K. Bandura, Bhardwaj, Boubel, Boyce, Boyle, . Brar, et al., 2019a). Since then CHIME has continued to release data on a series of repeating FRBs discovered in the first two years of operation. This increased number of FRBs has allowed, for the first time, a study of the statistical properties of these sources. This has led to many interesting discoveries about the properties of these sources, including the periodic nature of at least one repeater. At the time of writing, CHIME has not yet published a catalog of single burst FRBs, although estimates place the number of observed bursts at well over 1000 (Amiri, K. Bandura, Bhardwaj, Boubel, Boyce, Boyle, Brar, et al., 2019b). In addition, the increased number of repeating FRBs has allowed for an extensive multi-wavelength community to form. More repeaters mean that large surveys of archival data are also more likely to find serendipitous bursts. In addition, real time alerts of individual CHIME bursts are planned for the near future (through VOEvents).

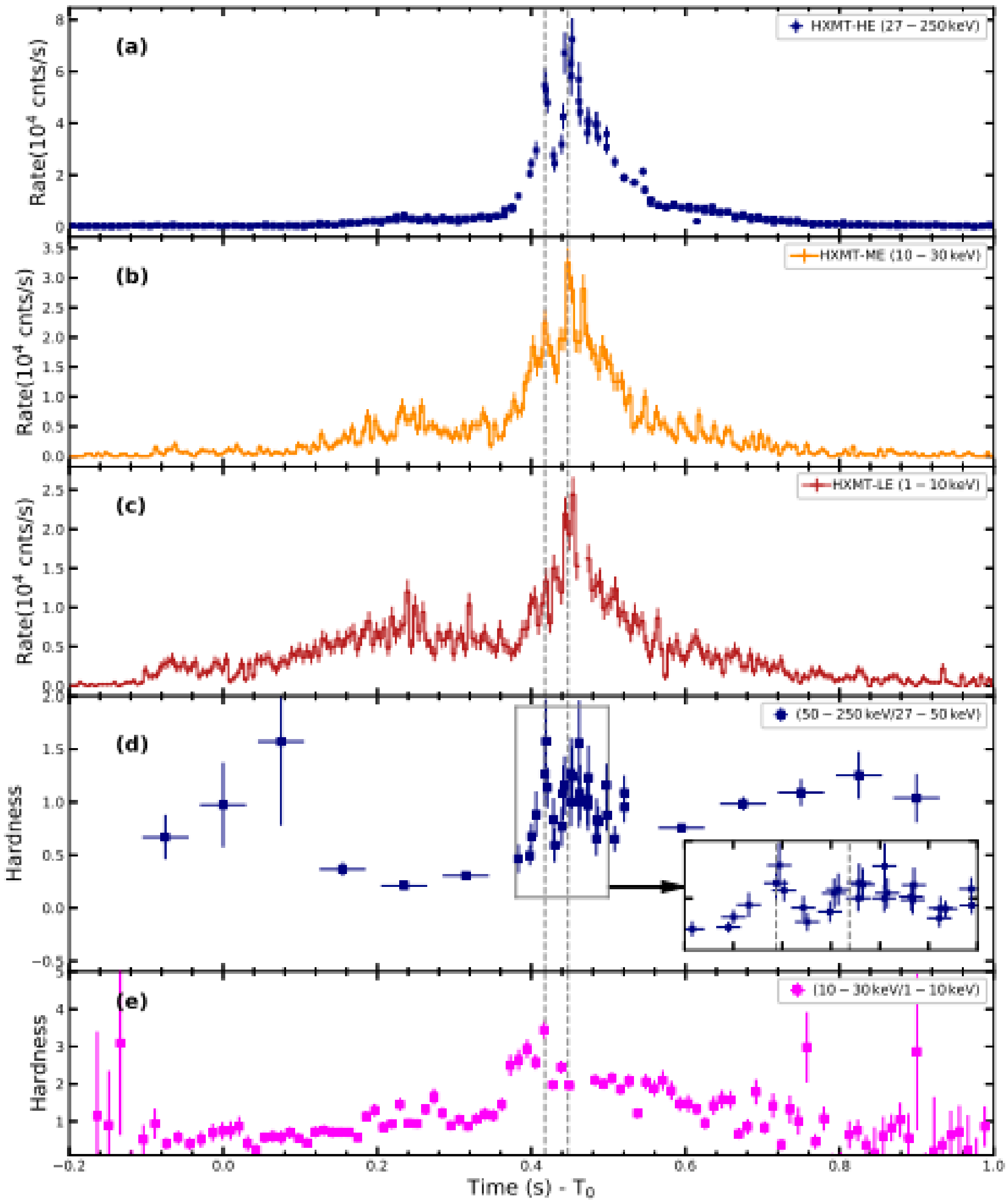

FIGURE 1.5: *Insight*-HMXT Observation of SGR 1935+2145 (Li et al., 2020). The energy ranges in plots a), b), and c) refer to the specific energy ranges on *Insight*-HMXT. The final two plots show the ratio between the counts within specific energy ranges. The dashed line in the figure represents the time of the two CHIME bursts.

The multi-wavelength search is a well motivated effort. As will be briefly discussed, many FRB models predict multi-wavelength counterparts. A conclusive simultaneous detection of an FRB with any counterpart remains elusive although there are a couple observations of note. The first and most recent observation is that of a soft gamma-ray repeater burst from SGR 1935+2154 in the X-ray band along with the observation of a low dispersion FRB-like pulse, FRB 200428 (Andersen, K. M. Bandura, et al., 2020). The FRB-like pulse was observed in two radio telescopes, CHIME (Andersen, K. M. Bandura, et al., 2020) and STARE2 (Bochenek et al., 2020). This was temporally and spatially coincident with the galactic magnetar flares observed by *Insight*-HMXT, shown in Figure 1.5 (Li et al., 2020). Additionally, the flare was observed by INTEGRAL (Mereghetti, Savchenko, Ferrigno, Götz, et al., 2020b) and Konus-*Wind* (Ridnaia et al., 2020). Although this discovery is a significant step forward towards the association of FRB with magnetar activity, the biggest discrepancy between this radio observation and FRBs is the flux. The least energetic FRB observed is still 3 orders of magnitude brighter than the $1.6(3) \times 10^{26}$ erg Hz^{-1} observed by STARE2. This still remains $\sim$10 orders of magnitude brighter than typical pulsar or RRAT transients, which makes its association with FRB-like phenomenon very likely (Bochenek et al., 2020).

The second potential observation is a much weaker detection of a sub-threshold GRB with a single burst FRB 131104 (DeLaunay et al., 2016). This *Swift* gamma-ray event was detected with a 3.2σ significance. The event was not triggered by *Swift* due to the low significance and the event was near the edge of the detector where there is a lower sensitivity. This transient shares no properties with the more significant recent detection (much longer duration, different spectral properties, etc). Follow-up observations also found that the transient is most likely associated with an unrelated AGN flare although this still remains controversial (Shannon et al., 2017).

Many theories attempt to model the phenomena surrounding FRBs. The lack of any potential multi-wavelength counterpart (until recently) combined with the low number of FRBs published pre-CHIME led to a very open parameter space (Platts et al., 2019). This in turn led to a vast number of models to describe FRBs. Many of these models now have difficulty in describing all FRB phenomenon but it is possible that sub-classes of FRBs may be attributed to these older models. For an overview of many of these models see (Platts et al., 2019). Some of the challenges that FRB models have to overcome is the all-sky rate, repetition/non-repetition, periodicity, and energetics. Very few models cover all of these phenomenon, with periodicity proving especially challenging. Only one periodic FRB is currently known, FRB 180916.J0158+65, whose $\sim$16 day period was discovered by CHIME (Amiri, Andersen, K. M. Bandura, Bhardwaj, P. J. Boyle, Brar, Chawla, T. Chen, Cliche, Cubranic, Deng, Denman, Dobbs, Dong, Fand ino, et al., 2020a). There is also an indication that repeating and non-repeating FRBs may have different spectral properties, which may suggest they originate from different progenitors (Andersen, K. Bandura, et al., 2019).

Two models which have received particular attention are the asteroid+neutron star model and the magnetar maser model. Both of these models require a highly magnetic neutron star to be the origin of the bursts but they differ on the mechanism of the emission. The asteroid+neutron star model seeks to explain all of the aforementioned FRB features in a unified self-consistent model. In this model the emission is due to coherent curvature radiation from ultra-relativistic electrons accelerated during the impact between an asteroid and a highly magnetized neutron star. The model explains the repeating FRBs as neutron stars moving through dense asteroid fields, which would also explain the non-poissonian distributions of the observed burst times. The $\sim$16 day periodicity seen in the one periodic FRB is explained through a neutron star in a tight orbit with a stellar object containing a debris disk. The model predicts that there should be no observable gamma-ray emission detectable by modern instrumentation. Due to the uncertainties in the distribution of asteroids around different stars, this model contains many parameters which are not well constrained (Geng et al., 2020; Dai, 2020; Dai et al., 2016).

The other FRB model of particular note is that of flaring magnetars. One mechanism that is favored by modelers is FRBs being produced through flare-induced synchrotron maser emission (Metzger et al., 2017). The model predicts that in the ejecta surrounding highly magnetized neutron stars, flares from the central object can induce a population inversion in the electron population which will produce a FRB. The flare itself should also be observable. Many properties of FRBs motivate this model, including the high polarization and rotation measure of FRBs, which is indicative of a dense, and highly magnetized environment (Michilli et al., 2018) and the FRB rates (Nicholl et al., 2017). Some tension continues to exist between the exotic properties of some of the repeaters, and the galactic magnetar population. FRB 121102 has been active since its discovery which is highly puzzling as one would expect that this should only occur in the early stage of a magnetars' birth and the FRB rate should fade over time (Metzger et al., 2017). The recent CHIME detection is in line with the early predictions of this model, namely that there should exist a rapid high energy counterpart. The model has very specific predictions on the flux and spectral shape of the multi-wavelength emission expected to be produced from synchrotron emission in these extra-galactic FRBs; they have recently been refined based on the observations of CHIME (Margalit et al., 2020). Although the galactic magnetar flare was only observable in the X-ray band, the same model is extended to the derived shock properties of the more energetic FRBs, and the peak of the synchrotron emission shifts to the HE and VHE regimes. This millisecond duration emission has yet to be observed; a detection of rapid simultaneous VHE emission from any FRB would strongly support this model. Figure 1.6 shows those predictions, namely the peak energy of the HE emission for a series of localized repeaters and non-repeaters.

With regards to this thesis there are also several limits placed by other experiments with similar capabilities to our system that one should note. MAGIC and a series of Fermi-LAT analyses completed by independent teams have all placed upper limits on the persistent and afterglow emission for a variety of repeating FRBs. There currently exists no gamma-ray association with FRBs (see 5 for a summary of these studies).

There also exists a wealth of literature discussing the potential rapid optical emission for FRBs from a variety of models including the synchrotron maser emission model described above (Metzger et al., 2017). There are also many studies using conventional optical telescopes to search for counterparts, yet none have been successful (see G. Chen et al., 2020 for a summary). The sensitivity of VERITAS to detect rapid optical transients, as compared to current and future generations of telescopes, will be discussed in depth in Chapter 3.

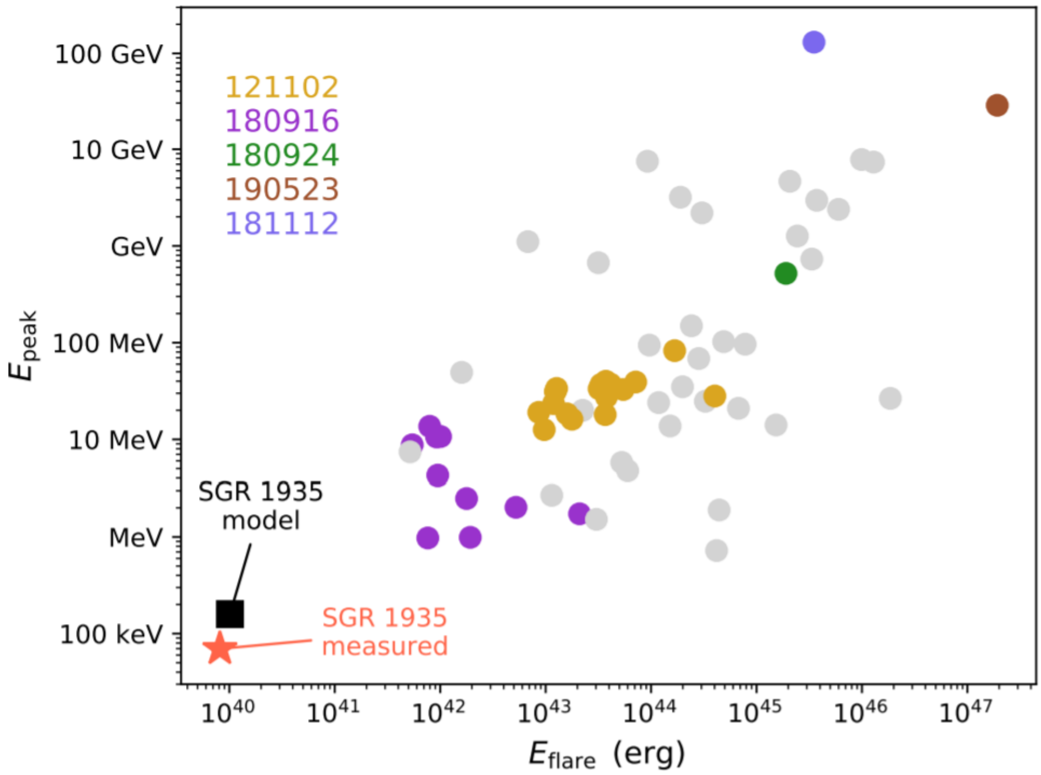

FIGURE 1.6: The predicted energetic properties of the high energy counterparts to FRBs predicted in the synchrotron maser emission model based on radio observations. The model predictions and the observations of SGR 1935+2154 are shown and are in close agreement. Figure taken from (Margalit et al., 2020).

FIGURE 1.7: Photograph of the four VERITAS Telescopes in addition to the central control building. The main control room is the building with the white roof just left of center. A museum and administrative building with a green roof is also pictured. Image Credit: Larry Ciupik.

1.2 VERITAS Instrument

The VERITAS telescope is an array of four 12m diameter Imaging Atmospheric Cherenkov Telescopes (IACTs) located in southern Arizona, USA. The array is located at the base of Mount Hopkins at the Fred Lawrence Whipple Observatory. The array can be seen in Figure 1.7. The details of how the detector operates will be discussed in depth in Chapter 2. All observations processed in the following chapters will utilize data from the VERITAS telescope.

1.3 Gamma-ray Transients

The phrase "gamma-ray transients" usually refers to the class of objects known as gamma-ray bursts. Within this class however there exists a diversity of phenomena and progenitors. The vast majority of GRBs are categorized as long GRBs, tied to supernova, or short GRBs, associated with neutron star mergers. There also exist subclasses of each of these and exotic GRBs which have been associated with other energetic phenomenon. Classic phenomena that are associated with GRBs are not the focus of this thesis. Because a FRB counterpart may resemble a classical GRB, many of the techniques used to place limits on FRBs were first used in the context of GRBs. For a recent review of long gamma-ray bursts in the context of supernovae, see (Cano et al., 2017). For similar review for short gamma-ray bursts and neutron star mergers, see (Baiotti et al., 2017). There are also many FRB models that stem from classic GRB phenomena and as such predict a GRB counterpart. These "cataclysmic models" are becoming disfavoured in the literature due to difficulties in reproducing periodicity and repetition of FRBs.

1.4 Transients with IACTS

There exists a long history of hunting transients with IACTs. Gamma-ray bursts were predicted to be energetic enough to produce an observable flux in the VHE regime early in the history of IACTs (B. Zhang et al., 2004). But these observations come with some large difficulties. Firstly, the field of view of IACTs is much smaller than the scintillator based technology used in instruments like Fermi-GBM. This means that the expected number of serendipitous GRBs is much smaller than that of the Fermi-GBM instrument. Fermi-GBM effectively observes over eight steradians of the sky and has a rate of around 15 GRBs per month. The $\approx$ 10 degree-squared FOV of an instrument like VERITAS is less than 1 percent of that; this results in less than one expected GRB in 5 years of observation time. Also, from the GRBs that have been observed with space-based instruments only the brightest and hardest are expected to be observable with ground-based instruments. This lowers the number of serendipitous observations even further. Additionally, the observation time of VHE instruments is only approximately 1000 hours per year. All of these factors combine to make serendipitous observations a very poor strategy for detecting GRBs with the current generation of ground-based IACT instruments.

The solution is to use an external trigger from these lower threshold, wider FOV instruments, and follow-up the source position in realtime. This strategy also allows for independent verification that the signal observed is indeed a GRB. Systems like this rely on the GCN (Gamma-ray Coordination Network), a system which publishes GRB alerts with position information on these bursts in realtime. The latency

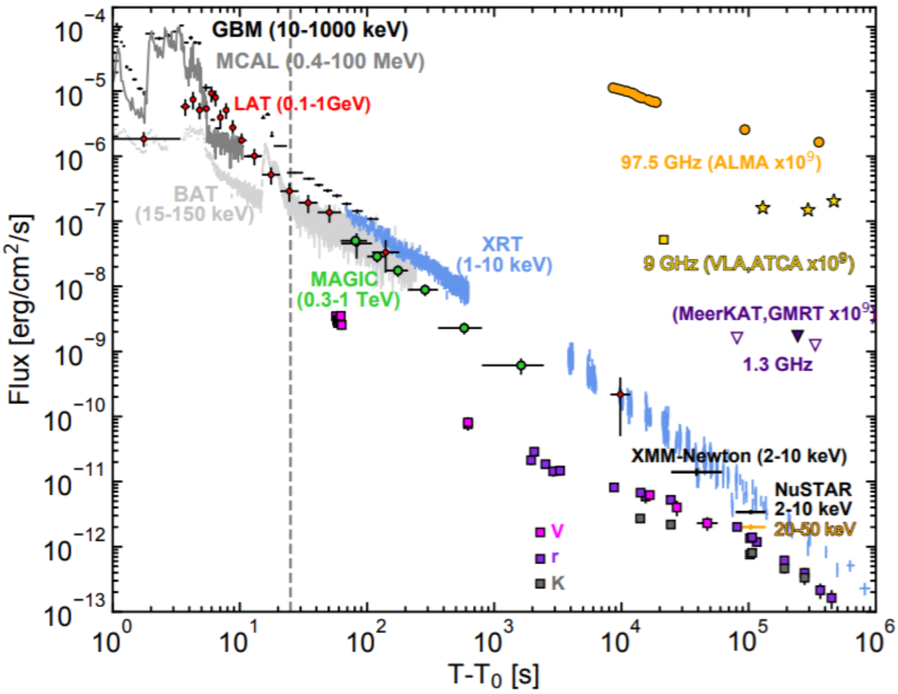

FIGURE 1.8: The multi-wavelength lightcurves for the GRB first observed by MAGIC. The TeV points can be seen after 10s although this is due to observing delays; emission is expected to peak in the LAT and GBM data. Figure taken from (Veres et al., 2019).

of these systems remains an issue, and although the systems themselves have an increased degree of automation, it is still common to see delays from several minutes to several hours in the GCN from the time of the burst to a precise position for the GRB. In addition, there is a delay introduced by the need for human confirmation of the burst and the time needed to slew, which at VERITAS can last up to 15 minutes. In spite of these challenges, in the past couple of years we have seen numerous GRB detections published by a variety of IACTs (MAGIC Collaboration, Acciari, Ansoldi, Antonelli, Arbet Engels, Baack, et al., 2019; MAGIC Collaboration, Acciari, Ansoldi, Antonelli, Engels, et al., 2019; Rhodes et al., 2020; Abdalla et al., 2019; de Naurois et al., 2019). One such GRB observed by MAGIC, along with the multi-wavelength observations, can be seen in Figure 1.8.

Optical transient searches also have a history with IACTs. The current generation of IACTs is dominated by three telescopes: MAGIC (Aleksić et al., 2016), H.E.S.S. (Ashton et al., 2020), and VERITAS (Holder et al., 2006). In recent years each of these systems has been modified to implement an optical system. The earliest of these was installed by H.E.S.S. This system involved a new camera placed in front of the

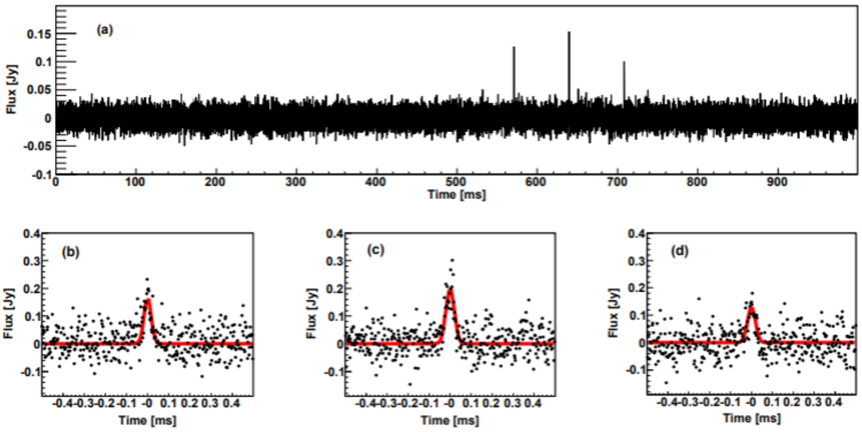

FIGURE 1.9: A light curve from the H.E.S.S optical system in the direction of V4641 Sgr (an X-ray binary). Figure a) Shows 1s of the raw data, with the following sub-figures highlighting the area around the clearly visible flares along with an over-plotted Gaussian fit. Figure is taken from Deil et al. (2009).

existing chrenekov camera (Deil et al., 2009). The camera was composed of 7 PMTs, with a central PMT located at the primary focus position for the object under study. The wavelength range 350-550nm was used, which is approximately in the range of traditional Johnson-Cousins B band (Bessell, 1990). The 6 outside pixels were used as a veto system to reject terrestrial transients. As will be described later in this thesis, a flare-finding and vetoing algorithm was used to detect optical flares. The system operated with 2.56 μs sampling detecting flares with durations as short as $\sim$20 μs and as faint as 0.1 Jy. The system was used to detect rapid optical flaring from an X-ray binary, an example of which can be seen in Figure 1.9. Although successful as a proof-of-concept in the use of IACTs as rapid optical photometers the system did have some significant limitations. This system was installed only on one telescope, and had difficulties in rejecting terrestrial transients like meteors. It also required the installation of a secondary camera over the Cherenkov camera (obscuring the primary camera), which meant that simultaneous gamma-ray and optical observations were not possible. As such, the system has not seen much use in recent years beyond this early proof-of-concept.

MAGIC also independently developed an optical system and has performed a similar study of fast radio bursts as will be completed in this thesis, although less extensive (MAGIC Collaboration, Acciari, Ansoldi, Antonelli, Arbet Engels, Arcaro, et al., 2018). The non-detection light curves can be seen in Figure 1.10. This system was installed in the central pixel of MAGIC-II (Hassan et al., 2017). The system is capable of detecting 1-ms optical flashes down to ∼8 mJy around ∼350nm. Faint meteor flashes were also a large contribution to their irreducible background, similar to H.E.S.S. This system does improve over the H.E.S.S. system by allowing for simultaneous observations, however due its installation only on MAGIC-II, vetoing and sensitivity are still persistent issues.

VERITAS itself has at least 4 different implementations of optical systems. These systems will be described in Chapter 3, along with optical system used in this thesis. The VERITAS optical system will also be shown to have major advantages over not only traditional optical systems, but also the systems used by other IACTs.

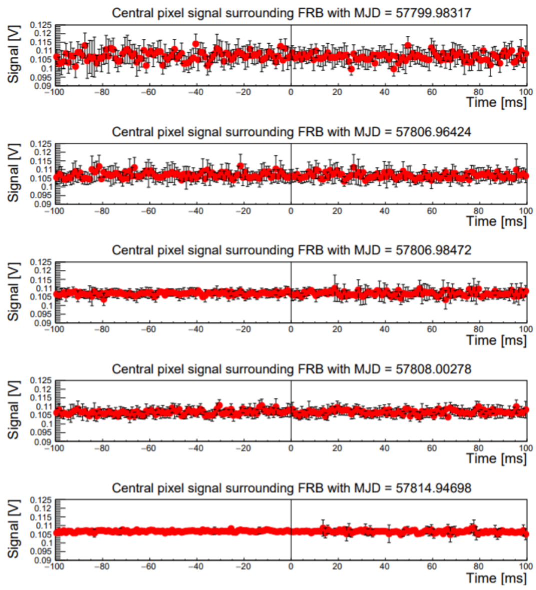

FIGURE 1.10: MAGIC optical observation of FRB121102. Multiple bursts are centered in the 5 plots. The vertical axis is plotted as the voltage response which is proportional to U-Band flux. Figure taken from MAGIC Collaboration, Acciari, Ansoldi, Antonelli, Arbet Engels, Arcaro, et al. (2018).

1.5 Thesis Overview

The rapid development of optical capabilities in IACTs now allows for an exciting class of new multi-wavelength observations with a single instrument. The perfect candidate for these observations are FRBs, as both rapid optical flaring and VHE emission are of interest in constraining theoretical models. This thesis will show the result of a study involving 5 repeating FRBs monitored using VERITAS. The structure of the thesis is as follows:

- In Chapter 2 the gamma-ray system in VERITAS will be described. This includes the triggering, description of Hillas parameters, and description of hardware.

- In Chapter 3 the optical system including its hardware and calibration will be described. The sensitivity of the system will be highlighted and contrasted to previous optical monitoring at VERITAS.
- In Chapter 4 a summary of the results of the FRB observing campaign will be presented.
- In Chapter 5 the implication of these FRB observations will be discussed in the context of FRB models and previous observations.
- In Chapter 6 a summary of this thesis will be presented.

Chapter 2

VERITAS Instrumentation

In this section, the VERITAS instrument will be presented as well as some of the theory behind Cherenkov astronomy. The section should not be considered a complete summary of VERITAS's abilities and functions, but rather a focused picture of VERITAS capabilities that are relevant to fast radio burst observations. The chapter will begin by outlining the Imaging Atmospheric Cherenkov Telescope (IACT) technique for observing gamma rays and end by highlighting the new optical system.

The IACT technique and the underlying physics behind extensive air showers are presented first in Section 2.1. This is followed by a description of the hardware in the VERITAS telescope, specifically a description of the camera and telescope design which is presented in Section 2.2. The classical data acquisition is described in Section 2.3, and is followed by a description of the new current monitor in section 2.4. All of the offline data analysis is presented later in Chapter 3 (ECM Analysis) and Chapter 4 (Gamma-Ray Analysis). The present chapter elucidates the structure of the instrument itself, and highlights some of the unique aspects of the design which affect the optical data analysis in ways different from that of traditional optical telescopes.

2.1 Imaging Atmospheric Cherenkov Technique

The challenge in gamma-ray astronomy is one of very low fluxes that are naturally difficult to detect. In the very-high-energy regime (E>100 GeV), spaced-based detectors like Fermi-LAT (Atwood et al., 2009) no longer have the interaction volume to produce meaningful results. Instead, one of the most effective solutions is to turn to natural volumes, like the atmosphere, and indirectly detect particles based on the secondary particles produced by interactions in these volumes. These interactions of a high energy particle with the atmosphere are collectively referred to as Extensive Air Shower (EAS).

When considering an EAS, the simplest interactions to consider are those in purely electromagnetic cascades. These are the types of cascades created by gamma-rays. These interactions are governed by only 4 particles and 2 fundamental interactions. The first of these interactions is pair production which involves the incoming photon, an electron and positron, and a mediator nucleus in the following way:

$$\gamma + M \longrightarrow e^{+} + e^{-} + M^{*}, \tag{2.1}$$

where M is the mediator nucleus and M* is an excited state. The mediator nucleus is present in the atmosphere, and is necessary for momentum conservation to hold. On average this will occur after one radiation length in the atmosphere, with radiation length being defined as the thickness of a material over which a particle's energy is reduced by a factor of e, such that we can define the current energy of a particle in the form:

$$E = E_0 \mathrm{e}^{-x/X_0}, \tag{2.2}$$

with X_0 being the radiation length, E_0 being the original particle energy, and x being the distance travelled by the particle. In air this radiation length is $\sim$ 37 g cm^{-2}. Since the vertical thickness of the atmosphere is $\sim$1000 g cm^{-2}, it becomes clear why the atmosphere is opaque to this radiation. Once the original pair production has occurred and the forward moving electron-positron pair has traveled another radiation length a second process, bremsstrahlung [1] radiation will begin to dominate. Qualitatively, this form of radiation occurs when a charged particle is deflected in the electric field of a target nucleus. In a purely classical treatment of this interaction the acceleration, which is proportional to the amplitude of the electromagnetic radiation, is proportional to Ze^2/m (with Ze being the charge of the nucleus, and m_e being the mass of the incident particle of charge e). In the case of particles in an EAS, the electron and positrons produced will produce secondary gamma-rays via this process.

[1] German for "braking radiation".

All of these emission mechanisms will have a typical angle of emission of order $m_e c/E$ rad, with E being the electron energy and m_e being the rest mass of the electron. This means that for purely electromagnetic cascades the resulting air shower is a very tightly collimated. As the EAS continues to propagate through the atmosphere it will excite the electrons in the nuclei of the surrounding atoms. This will also cause a loss of energy, known as the ionization loss, which follows the so-called Bethe formula. As the particles continue to lose energy to processes, eventually the subdominant ionization loss becomes equal to the radiation losses. The peak in the number of particles, often referred to as the "shower max", happens at an altitude of $\sim$10 km.

EAS are not only produced by gamma rays but also hadronic particles from cosmic rays. These EAS contain the aforementioned electromagnetic processes but also contain other processes, like pion production, with diffrent properties. The large number of secondaries include pion, muons, and electrons, all of which will continue to interact as they move through the atmosphere. The resultant air shower profile will be dramatically different, as can be seen in the Monte Carlo simulations shown in Figure 2.1. This difference in profile allows one to veto the much more common charged cosmic rays from the gamma-rays. One does not actually measure these particle profiles directly; instead there is another process by which an observable photon is produced.

The secondary charged particles ($e^{\pm}, \pi^{\pm}, \mu^{\pm}$) produced in EAS are often at high enough energies to be moving faster the speed of light in air, and they emit a form of radiation called Cherenkov radiation. Although the first observation preceeded him, the effect is named after Pavel Cherenkov whose extensive experimentation in the 1930s and 1940s was critical in connecting the effect to the theoretical predictions made by others (Jelley, 1958). The effect is qualitatively very simple to grasp, and can be viewed as a "sonic-boom" but for superluminal charged particles in a dielectric medium, as shown Figure 2.2.

Cherenkov radiation begins when a particle exceeds the threshold velocity $v/c > 1/n$ where v is the velocity of the particle and n is the refractive index of the medium. When a charged particle passes through a dielectric medium, molecules surrounding the charged particle experience an electric potential, causing a polarization. As

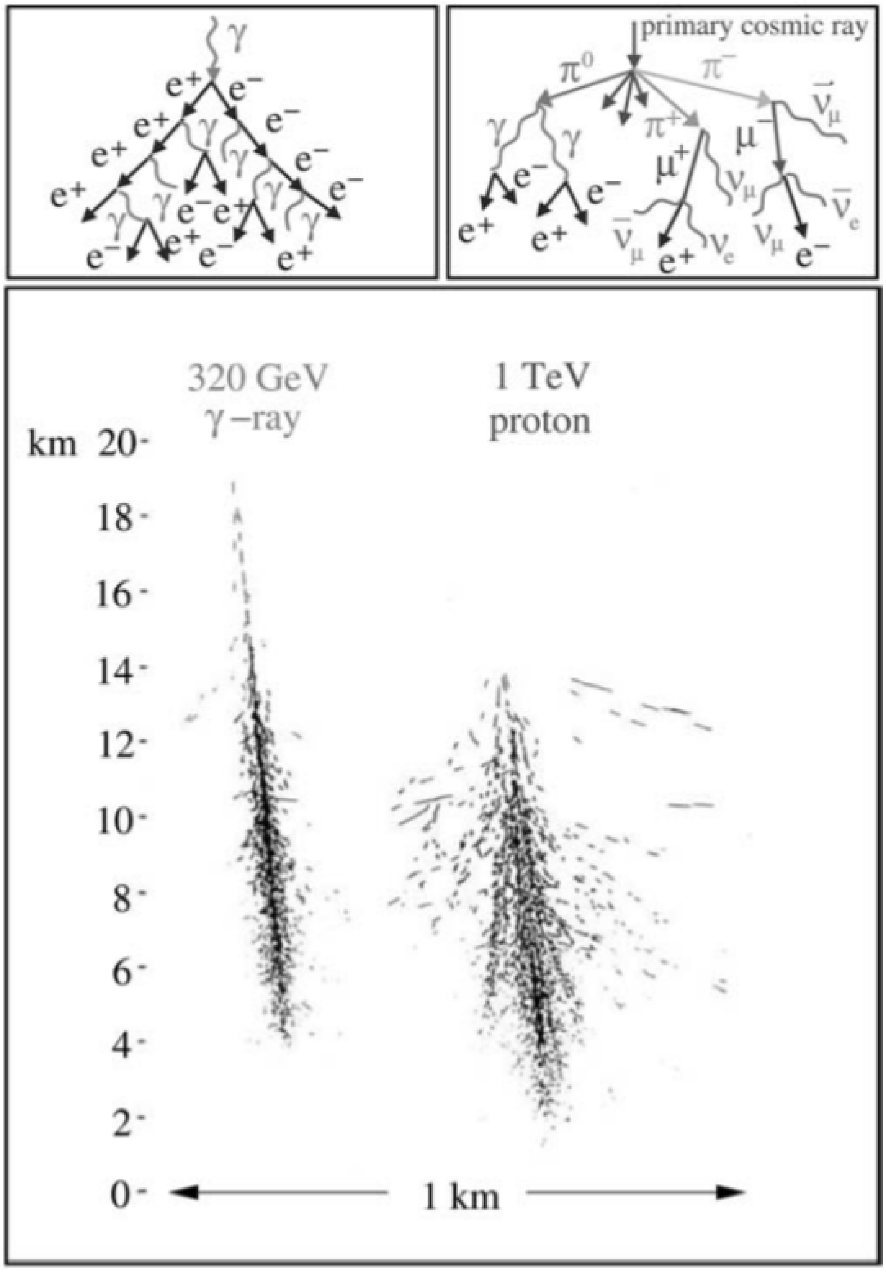

FIGURE 2.1: Monte Carlo simulation for a 320 GeV gamma-ray shower (left) and a 1 TeV proton shower (right). For illustration the horizontal scale is magnified by five. Figure taken from (Weekes, 2003) who credits D Horan.

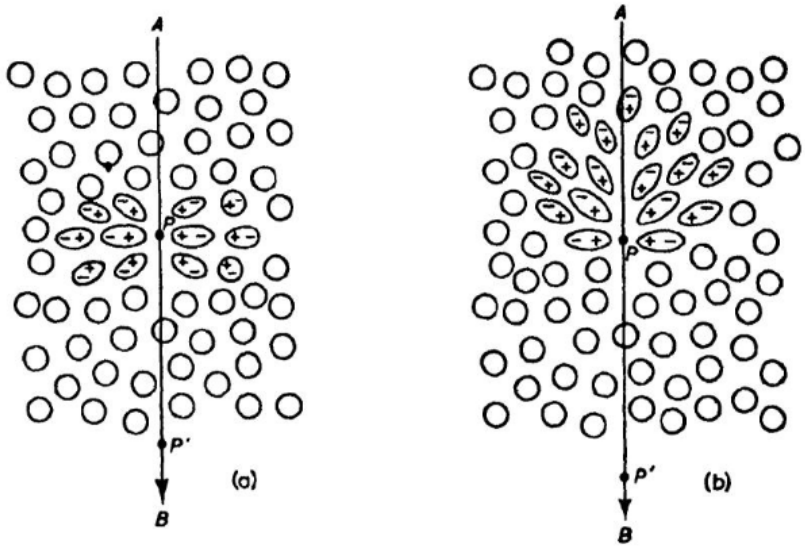

FIGURE 2.2: An illustration of the effect of a charged particle moving through a dielectric medium. On the right is a superluminal particle, and on the left is a low velocity particle. (Jelley, 1958).

the particle passes, the molecules radiate and return to a non-polarized state. If the particle is travelling slowly, then the electric field is symmetric and there is no residual radiation.

This symmetry in broken when the particle moves relativistically. In cases where the particle exceeds the speed of light in the medium, the polarization and restoration will occur on a slower time scale relative to the motion of the particle. This is due to electric fields propagating at the speed of light in the medium. Along the axis of the particle motion, a dipole will form that will produce an observable electromagnetic pulse. If one considers the interference patterns of the individual dipoles that form along the trajectory of the particle then it is a straightforward to show that the opening angle of the Cherenkov emission is $\cos\theta = (c/n)/v$, with θ being the angle between the trajectory of the particle and the Cherenkov wavefront. It is also simple to see from this formula where the threshold velocity for this emission comes from. For the refractive index of the atmosphere, the Cherenkov angle is $\sim 1^{\circ}$.

In an EAS, the primary and many of the secondary particles will be above the Cherenkov threshold. The majority of the particles that meet this criteria will fall in the core of the shower which at high energies typically develops closely along the trajectory of the original particle. The shower core itself is also quite small, for a typical 1 TeV EAS the shower will be ~4 km in length with a radius of ~21 m at a height around 10 km. This will produce a Cherenkov flash of radius $\sim$100 m when the Cherenkov light reaches the ground. Since the particles are travelling close to the speed of light, the Cherenkov photons that are produced during the early stage of shower development arrive at roughly the same time as the photons produced towards the end. This temporal spread is typically 3-5ns.

The Cherenkov emission will peak in the blue range of the optical spectrum. The blue peak is a result of to both the λ^{-2} dependence of Cherenkov light and the atmospheric absorption at UV wavelengths. The principle of an IACT is that one can image this Cherenkov light from the EAS once it reaches the ground. With multiple telescopes, separated by $\sim$100 m, one can image the shower from different angles. With these multiple images one is able to stereoscopically reconstruct many parameters of the EAS based on the properties of these images. Properties like arrival direction, energy, and particle type of the original cosmic-ray can all be reconstructed. An example of a gamma-ray image is shown in Figure 2.3. In this image pixels of an IACT are shown with a color representing the incident light on the camera from a gamma ray shower. The reconstructed position of the shower is also shown. The elliptical shape shown in the cameras is used to characterize a gamma-ray event.

2.2 Camera and Telescope Design

VERITAS is an array of four telescopes located at 31°40’30"N 110°57’07"W at the basecamp of the Fred Lawrence Whipple Observatory (FLWO) at an altitude of 1,268 m. The telescope mirrors are divided into 345 hexagonal shaped spherical mirrors arranged in a Davies-Cotton design (Davies et al., 1957). At the focal point of each telescope is a camera composed of 499 PMT pixels. The telescopes each have an electronic trailer where low level triggers are processed. These electronic trailers are linked together and the inputs are processed through a higher level of trigger in the main control room. The VERITAS array has been operating since 2007 and has gone through 3 major upgrades in the past decade. The first upgrade was updating the array configuration. In order to increase the effective area of the experiment, the telescope labelled T1 was moved in 2009. The old and new configurations are shown

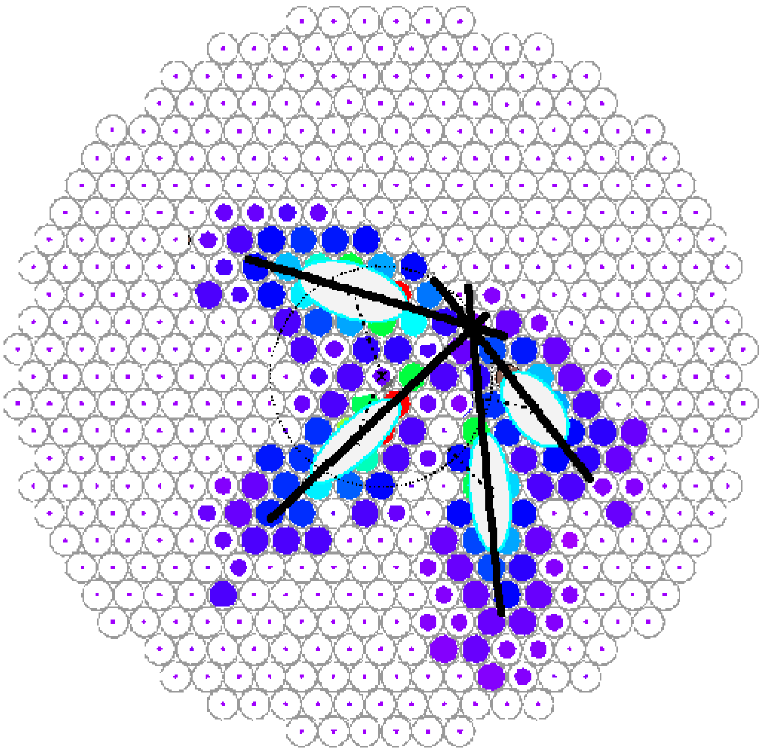

FIGURE 2.3: A four-telescope event as seen in the cameras of the VERITAS telescope. The four telescope images are stacked, and the charges of the event are shown in the effective pixels. The reconstructed position of the shower is shown as the intersection of the black lines (VERITAS Internal, 2010).

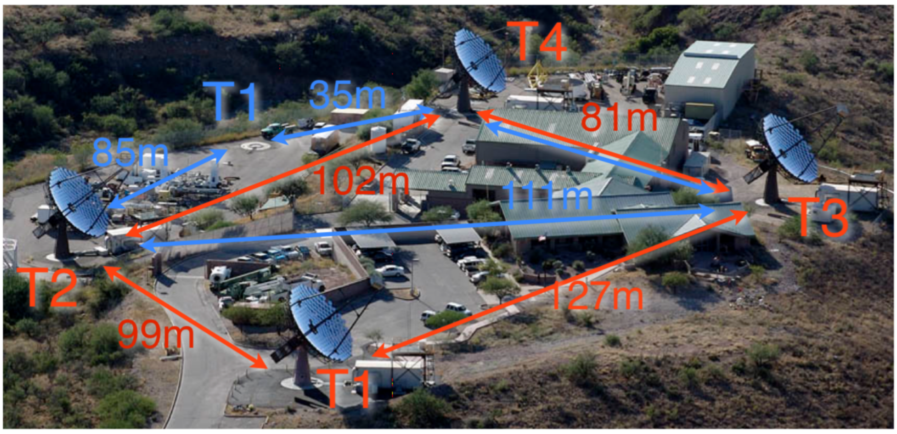

FIGURE 2.4: Aerial view of the V4 and V5 configurations. The current array is shown in red. The older configuration is shown in blue (Perkins et al., 2009)

in Figure 2.4. Data taken with the old array is referred to as V4 data and the post-upgrade data is referred to as V5. The current status is V6, which is post the PMT upgrade. The original Photonis XP 2970 PMTs were replaced by the current R10560-Hamatsu PMTs. When comparing the current analysis to previous VERITAS optical searches it is important to recognize in what period data was taken. Data reported in this thesis comes from the V6 period (post PMT upgrade).

As is common for IACTs, the mirror is not built out of a single reflector but instead has 345 facets. A larger light-collecting surface is formed by this arrangement of smaller mirrors, however this does increase the optical point spread function of the instrument as the focus and alignment of the facets will have random error. The benefit of such a system is primarily cost and maintenance. The individual mirror facets can be removed and replaced, allowing for continual polishing and re-coating of mirror facets with minimal impact on the instrument. The telescope itself has no protective dome like a conventional optical telescope and thus experiences a gradual weathering over time due to exposure to dust and rain. This will affect the reflectivity of the mirror facets as they degrade over time. On average, one of the four telescopes has a third of its mirrors replaced with newly re-coated mirrors each year.

Gamma-ray observations do not require as precise an optical point spread function as optical telescopes[2]. The point spread function (PSF) of an instrument is the

[2]It is easy to confuse the optical point spread function with the gamma-ray point spread function. The optical point spread function is only affected by the optics of the telescope: the mirror alignment, the facet shape, and the focal position. The gamma-ray point spread function is a measure of the size of a gamma-ray point source as measured by VERITAS. This is affected by our ability to reconstruct and

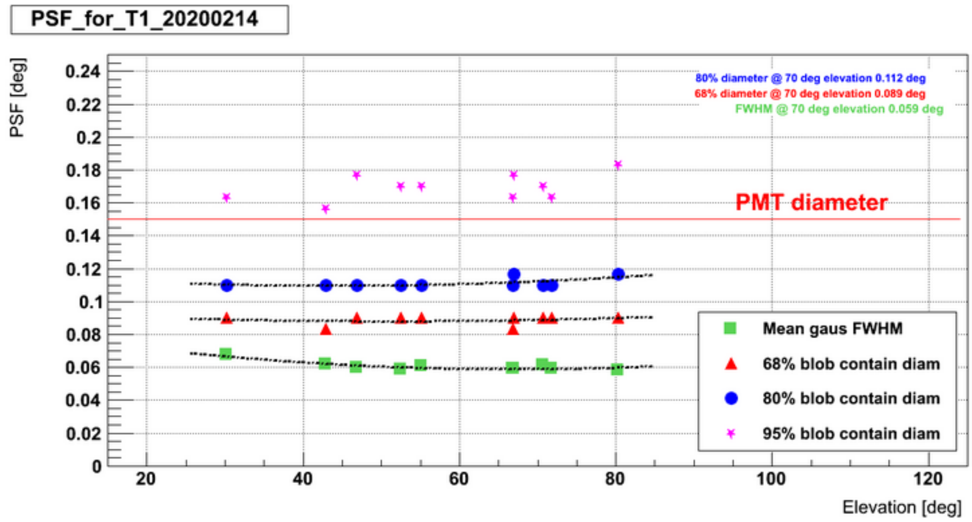

FIGURE 2.5: The optical PSF of the VERITAS T1 telescope in 2020. The PMT size is also shown. Other telescopes show a similar trend (VERITAS Internal, 2020).

size and shape of a point source imaged by the telescope. The PSF of most well-aligned telescopes is symmetric and can be modeled with a 2D Gaussian. Here, it is not photons from the objects itself being measured but instead large extended optical air showers, so the sacrifice to the PSF due to using the uncertainty present in a faceted mirror instead of a single reflector is not an issue for gamma-ray observations. Most shower events are spread over multiple pixels as can be seen in Figure 2.3.

The point spread function of the instrument is measured on a regular basis at VERITAS. Example results can be seen in Figure 2.5. The measurements of the PSFs are performed by covering the VERITAS Cherenkov camera with an opaque screen and using a CCD camera directed towards the focal plane to measure the image of a series of bright stars. The proper alignment of the individual facets assures that over 80% of the light falls in a circular region 0.15° in diameter. 0.15° is the size of the individual pixels of the camera projected onto the celestial sphere, beyond which an improved alignment does not increase the performance of the instrument for optical or gamma-ray observations. For reference the PSF of a single reflector telescope is usually sub-arcsecond.

measure the properties of the EAS. The gamma-ray PSF is 68% containment within a ∼0.16° diameter at 1 TeV. This is much larger than the ∼0.09° 68% containment diameter of the optical PSF.

Although having a relatively poor optical PSF does not affect gamma-ray observations, it does impact the capability of VERITAS to act as an optical telescope. Most optical telescopes have a very small point spread function (∼arcsecond resolution) which allows them to easily distinguish between sources and reduce the integrated night sky background (NSB).

The VERITAS cameras are composed of 499 pixels containing R10560-Hamatsu PMTs and a pre-amplifier. This gives the camera a 3.5° field of view. The pixels are topped with a Winston cone in order to help mitigate the effect of background light from external sources and to increase the effective area of the pixels. These are referred to as light cones.

The PMTs that are used in VERITAS follow a simple operating principle. A diagram of the PMT schematic structure is shown in Figure 2.7. The diagram should be read from left to right. Photons entering the camera create photoelectrons that are ejected in the evacuated glass tube. These electrons are accelerated and focused by an electrode onto a dynode. This multiplies the electron population by secondary electron emission. This secondary emission process is then repeated across multiple dynodes. A final collection onto an anode ends the process and outputs a current to an external circuit. The overall process results in a single photon being converted into an observable current.

In the VERITAS telescopes this PMT current is converted to a voltage and these signals are then amplified and sent to the trailer.

PMTs were selected for use in the gamma-ray telescope for their ability to detect low amounts of light in the correct wavelength regime (∼200-400 nm). PMT responses typically peak in the blue/UV; the VERITAS PMTs were measured prior to the upgrade, and the results are shown in Figure 2.6. The spectral response peaks at around 350 nm, and extends from beyond the capabilities of the measurement apparatus (250 nm) in the UV to ∼600 nm in the red. However they are not without their issues. Each PMT shows a unique conversion between photon to current, a quantity referred to as gain. These gain values are also not constant over time, and steadily degrade. Due to these effects, a series of multiple calibration runs are done throughout the year. These runs rely on the use of the "flasher" (Hanna et al., 2010). Flasher runs are the primary form of calibration with the VERITAS telescope and

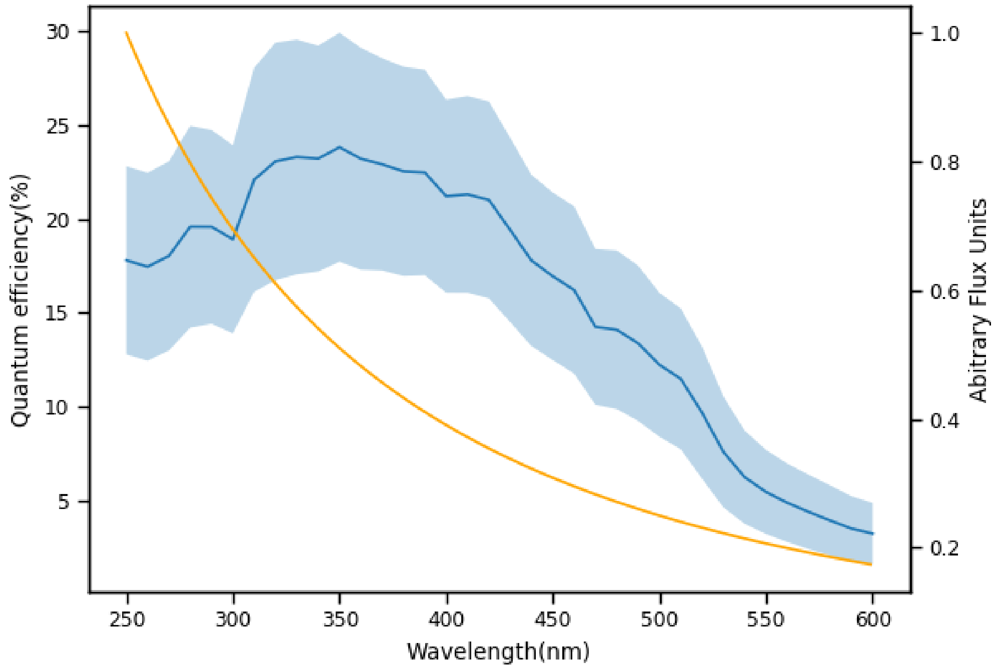

FIGURE 2.6: The spectral response for the Hamatsu PMTs used by VERITAS. The measurements were made by the Washington University VERITAS group. The solid blue line shows the quantum efficiency for the PMTs, with the error band showing the spread of the measurements amongst the PMTs. The orange line shows the typical un-absorbed Cherenkov spectrum of an extensive air shower as reference (Image generated by author).

they are done on a night by night basis. The flasher is a collection of 15 LEDs. Event triggers are synchronized with flashes of increasing intensity from the LEDs. Then each individual channel's relative gain can be calculated with respect to the mean value across the telescope. This allows for small corrections to the gain on a night by night basis. It also provides measurements to re-normalize gains through "flatfielding", where the HV supplied to each PMT is modified to bring the individual gains into alignment. This process occurs a few times throughout the year.

2.3 Data Acquisition and Triggering

Continuous storage of all of the PMT data would be a challenging task, and also not very useful. Since the rate of air showers is small (∼300 Hz), a triggering system is used so that data is only stored in regions surrounding a Cherenkov-like signal.

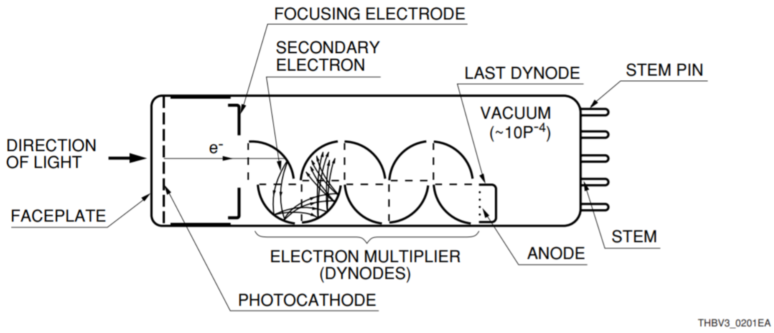

FIGURE 2.7: Diagram of a photomultiplier tube taken from (Hamamatsu Photonics, 2007).

During these short periods the PMT signals are digitized on a time scale commensurate with the Cherenkov signal time. These packets of data are called events. A Cherenkov-like signal would be expected to be bright in multiple pixels in multiple telescopes simultaneously. On the hardware level these triggers are implemented in 3 stages.

The firsts level of trigger, L1, is a constant fraction discriminator. A CFD is a triggering technique that acts as a variable threshold cut always triggering at a certain fraction of the total amplitude (to remove amplitude/timing issues that occur with normal threshold cuts). This occurs on a channel-by-channel basis and is built into the FADC boards. Every 2 ns the voltage is sampled from the FADC board and an 8 bit sample is recorded. Since the Cherenkov pulse lasts 4-8 ns the 8 bit sample is more than sufficient to fully sample the pulse.

The L2 trigger for a telescope compares the L1 trigger status of all neighbouring pixels. If three adjacent pixels have met the L1 trigger critereon then the L2 trigger is satisfied. The time window for the L2 trigger is 8 ns. L2 triggers occurs roughly at $\sim$kHz frequencies.

The L3 array trigger is the final trigger and it is implemented in the primary control room at the center of the array. All L2 triggers are sent to this central location. If two or more L2 triggers fall in a 100 ns window the L3 trigger is satisfied. Once this final trigger is satified, the flash analog-to-digital convert (FADC) memories of all PMTS on all telescopes are read out. A typical rate of L3 triggers is $\sim$ 300 Hz.

The events are stored in a custom Veritas Bank Format (VBF) format which can then be processed through custom software tools to produce higher level data products.

2.4 Enhanced Current Monitor

The enhanced current monitor (ECM) is one of the newest additions to the VERITAS instrument and works as an external and direct measurement of the incident light on the camera. This allows for parasitic observations of optical light from the sky of sources being observed by the four telescopes. A parasitic observation means that while normal gamma-ray observations are being performed, ECM data can be collected with no interruption to the normal DAQ processes. Instead of triggering and saving data only during the Cherenkov pulses, the ECM provides a continuous stream of measurements. This new system has many advantages over traditional optical cameras. The benefits and calibration of this system will be described in Chapter 3. This section will describe the hardware components.

Early installation of the system began in 2018 on the central pixel of telescope 1 (T1). In 2019, the system was fully installed on all 4 telescopes. This system is based on the DI-710 commercial data logger, a product of DATAQ Instruments[3]. A current monitor system, called VDCMON, has been implemented in VERITAS prior to the ECM which means that the ECM can simply branch off the VDCMON output of each PMT pre-amplification circuit in order to acquire the necessary signals from the camera PMTs. A circuit diagram showing the pre-amp circuit can be seen in Figure 2.10. Where the VDCMON output is shown, a splitter is installed to direct the output into the ECM. This has to be manually done for each individual pixel, and although it is possible to reconfigure which pixels are being monitored, the process is too long to practically transition configurations in the same night.

Once the pre-amplification circuit has been connected with the ECM, the signal is sent via Ethernet to a separate control PC located in the central building. From here the proprietary data acquisition software for the DATAQ instrument is used. The ECM files are not prohibitively large (~150 Mb for 30 min of observation) and as such are stored in the PC memory and archived weekly. The ECM is only active

[3] https://www.dataq.com/

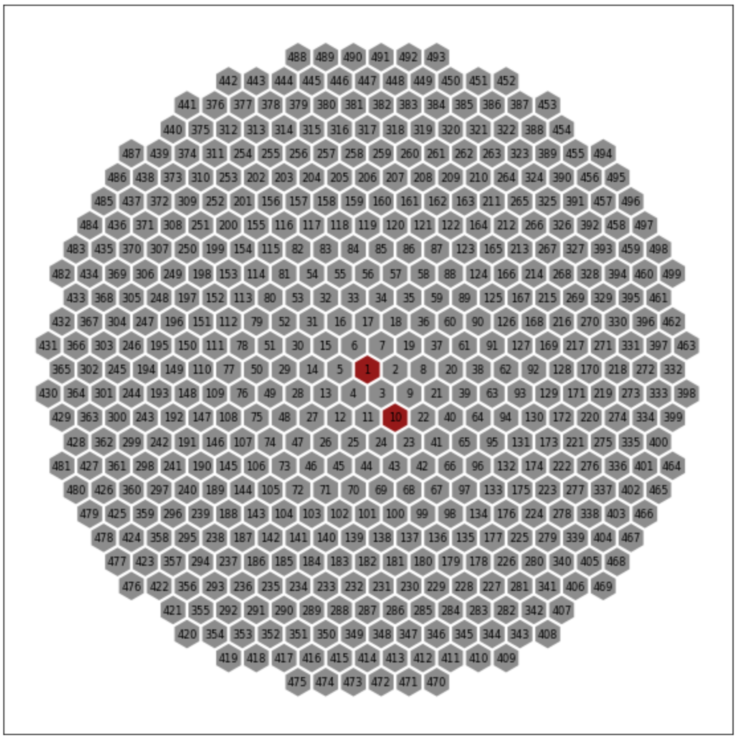

FIGURE 2.8: Two pixel ECM configuration at VERITAS. Labelled channel numbers are shown. Each hexagon corresponds to a PMT in the camera. The pixels being monitored by the ECM are shown in red.

for runs that have been specifically flagged as requiring optical data. This includes the FRB runs, but also programs like optical SETI.

The ECM can sample at a rate of 4800 Hz but this has to be shared by the number of pixels monitored. This means an effective maximum sample rate of 2400 Hz, with one signal pixel and one background pixel being monitored (two PMTs). This configuration is shown in Figure 2.8. The signal pixel is the PMT located at the center of the telescope. Different configurations are possible at VERITAS such as the monitoring of 4 pixels at 1200 Hz. This configuration is shown in Figure 2.9. Prior to 2018, there was no standardization of which pixels were being monitored. Through 2019-2020 one telescope has 4 pixels being monitored and the other three telescope in the array have 2 pixels monitored.

More detailed information about the ECM performance is discussed in Chapter 3.

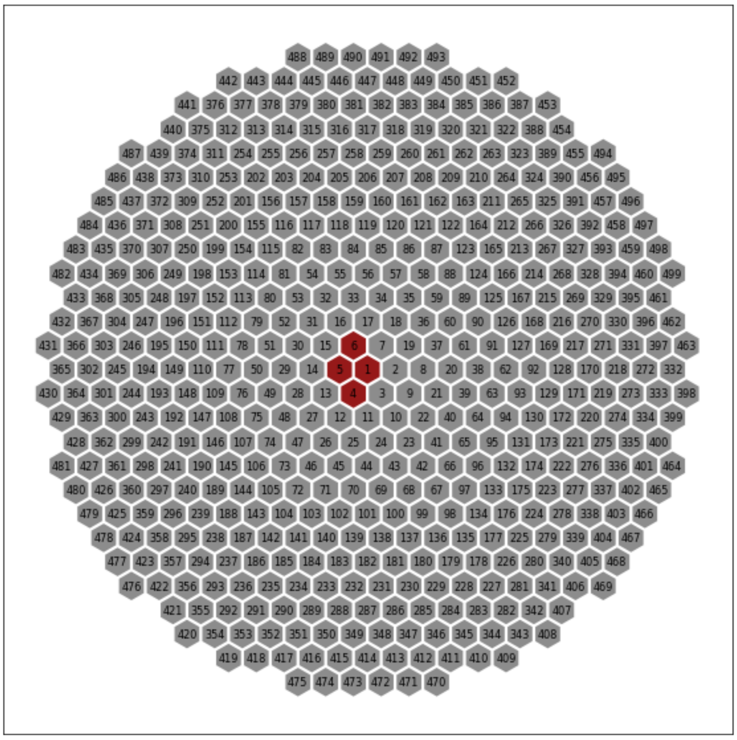

FIGURE 2.9: Four pixel ECM configuration at VERITAS. See Figure 2.8.

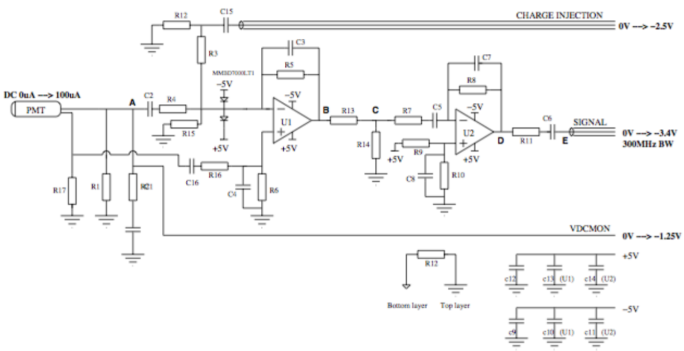

FIGURE 2.10: The pre-amplifier circuit for the VERITAS upgraded pixels are shown. Each pixel has such a pre-amp attached to the PMT. The VDCMON output can be seen on the right; this is where the ECM is parasitically attached (Internal VERITAS Communication, 2011).

Chapter 3

The VERITAS ECM

3.1 Introduction to the ECM

The Enhanced Current Monitor (ECM) is the newest addition to the VERITAS back-end. The system integrates commercial components in order to create an optical back-end. This is not VERITAS's first attempt to detect optical transients, but this new system contains many advantages over older systems which will be highlighted here.

The earliest study of optical transients can be attributed to the Whipple Observatory located at the FLWO prior to the construction of VERITAS (Cook et al., 1980). Whipple was a single dish IACT with a mirror diameter of ≈10 m. The original optical monitor design involved directly coupled PMTs reading out to a 6 pen chart recorder (an older analog recorder). This original study was used primarily to detect micro-meteorites and other small terrestrial transients and had a sensitivity down to 12th magnitude. A sample of the meteors detected by Whipple is shown in Figure 3.1.

At VERITAS, further developments were made using the VERITAS Transient Detector (VERy TRenDy) system (Griffin, 2011). The VERy TRenDy was an FPGA-based rate-meter. It relied on monitoring the L1 trigger systems to count PMT pulses. It monitored the central seven pixels of one VERITAS camera. The device acted more as a proof-of-concept than a science device. Many calibration tests were performed with the instrument including drift scans where stars of known brightness transit through the FOV of the optical instruments. The most notable result of VERy TRenDy was the detection of the Crab pulsar during a period of bright moonlight

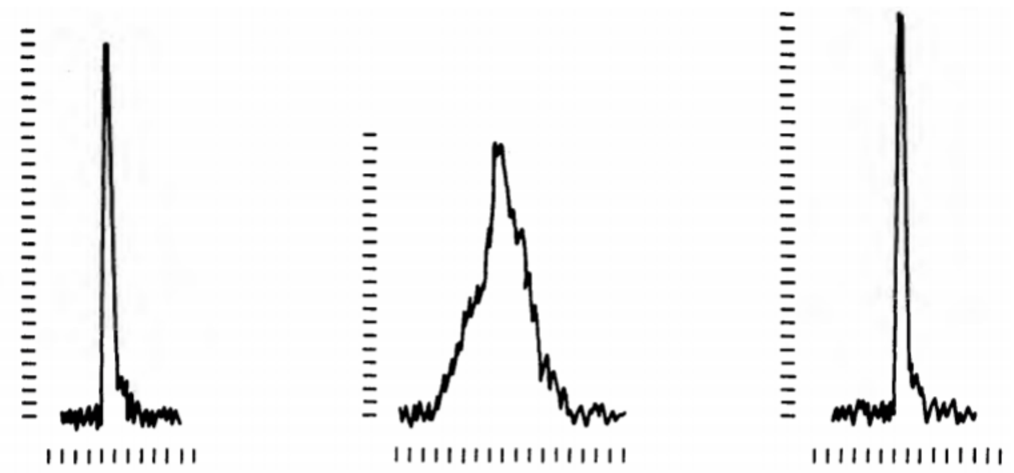

FIGURE 3.1: A sample of larger light pulses from the Whipple Observatory. The vertical divisions are such that two divisions are the threshold value. One horizontal division is 40ms. The optical transients are attributed to meteors. Figure is a trimmed selection from Cook et al., 1980.

on 2010/11/19. The total observing time was approximately 40 min. This result is shown in Figure 3.2. It was one of the first observations on VERITAS that illustrated its ability to detect millisecond transients. The major issue with the system was that it could not be used simultaneously with the gamma-ray DAQ. This meant that optical observations required dedicated time.

The next optical transient project at VERITAS dates from 2016-2017 (Chernitsky, 2017). This project tried to utilize the archival gamma-ray data for a search for optical transients. A study showed that there was a tight linear correlation between the current measured in the current monitor and the variance in the samples of event traces. Thus, the technique was referred to as the "pedestal variance technique". This means that for every array event that is triggered one can find the current in all the pixels of the camera. This translates to a measurement of the optical intensity across the camera. This method has the advantage over VERy TRenDy that it does not require dedicated observations to be taken. All VERITAS observations are archived which means that the method can be applied to years of archival data. The method can also be applied to all pixels in all cameras which means that it has a much wider field of view than VERy TRenDy. Due to both of these facts, to complete a large optical survey it appears as if all one would have to do is provide computing resources.

The method does have a few weaknesses. The largest of these are the sensitivity

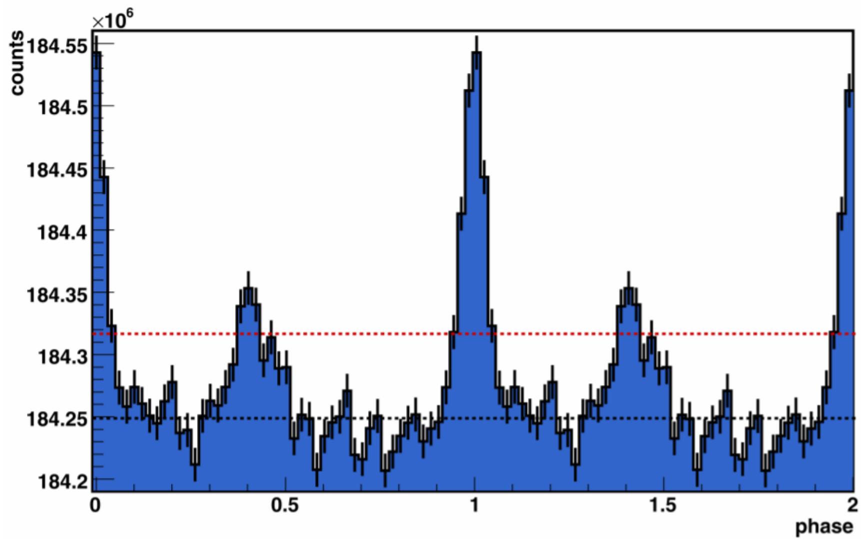

FIGURE 3.2: The detection of the Crab pulsar using the VERy TRenDY system. The plot shows the detected event counts stacked by phase bin. The black dashed line shows the mean value of the bins. The red line shows the 5 σ threshold. Both the major and minor pulses are significantly above the background (Griffin, 2011).

and the sample rate. Because the sample rate is equal to the L3 trigger the sample rate can be affected by factors including elevation, temperature, and seasonal changes in atmosphere. On average the trigger rate is ~300 Hz. This is significantly below the kHz sample rates of the older method. At 300 Hz, the minimum detectable flux is also only ~8 mag, approaching the limit of simple and inexpensive optical telescopes with fast CCD cameras (Griffin, 2011). In addition, triggering events contain Cherenkov light which provides an irreducable background. Averaging over many events will help to reduce this, but the cadence is decreased meaning that transients that are more rapid than 0.1 s become difficult to probe. This results in a method that has a cadence of below 10 Hz and can effectively probe events at ~6-7 mag.

The ECM strives to be the most effective optical monitor on VERITAS to date. It tackles the problems faced by VERy TRenDy by having a fixed sample rate that is continuous throughout the observations. It also allows for parasitic observations which solves many of the scheduling and operational issues caused by instrument changeover.

The improvement over the pedestal variance technique is in sensitivity and sample rate. The increase in both makes the instrument competitive when compared to optical telescopes. The sensitivity of the ECM is 11th magnitude when sampling at a rate of 1.2 kHz. This rate is far faster than most traditional CCD cameras and the sensitivity is deeper than all-sky video systems, which is typically 5 mag. This combination allows VERITAS to probe phenomena that are beyond the capabilities of many traditional optical telescopes.

One example of the capabilities of the system is shown by the asteroid occultation measurements performed using the ECM in a recent VERITAS study (Benbow et al., 2019). As an asteroid occults a star, there are visible effects due to the diffraction fringes that depend on the angular size of the star. If one has a parallax distance measure of the star then this allows the reconstruction of the radius of the star. An ECM light curve from a recent VERITAS observation of this type is shown in Figure 3.3. The diffraction fringes cause variations on the scale of tens of milliseconds so one must have a minimum sample rate on the order of milliseconds to detect the fringes. The sensitivity of VERITAS at this rapid sample rate allows VERITAS to measure on sub-milliarcsecond scales. This shows how opening up a new parameter space in rapidity and sensitivity with the ECM, has already begun to provide useful measurements.

3.2 ECM Spectral Response

An important consideration of the VERITAS ECM is its spectral response. Currently the ECM operates without a filter, so the spectral response is identical to the underlying PMT spectral response. This can be compared to traditional optical systems. The Johnson-Morgan photometric system has been adapted and implemented as a photometric standard (Binney et al., 1998). The U filter peaks around the same wavelength as the maximum PMT sensitivity (365 nm) but the PMT sensitivity extends well into the B filter range (peak wavelength 445 nm and FWHM of 94 nm). The PMT also extends well below the U filter cutoff but in practice atmospheric absorption will provide a natural cutoff bellow 250 nm.

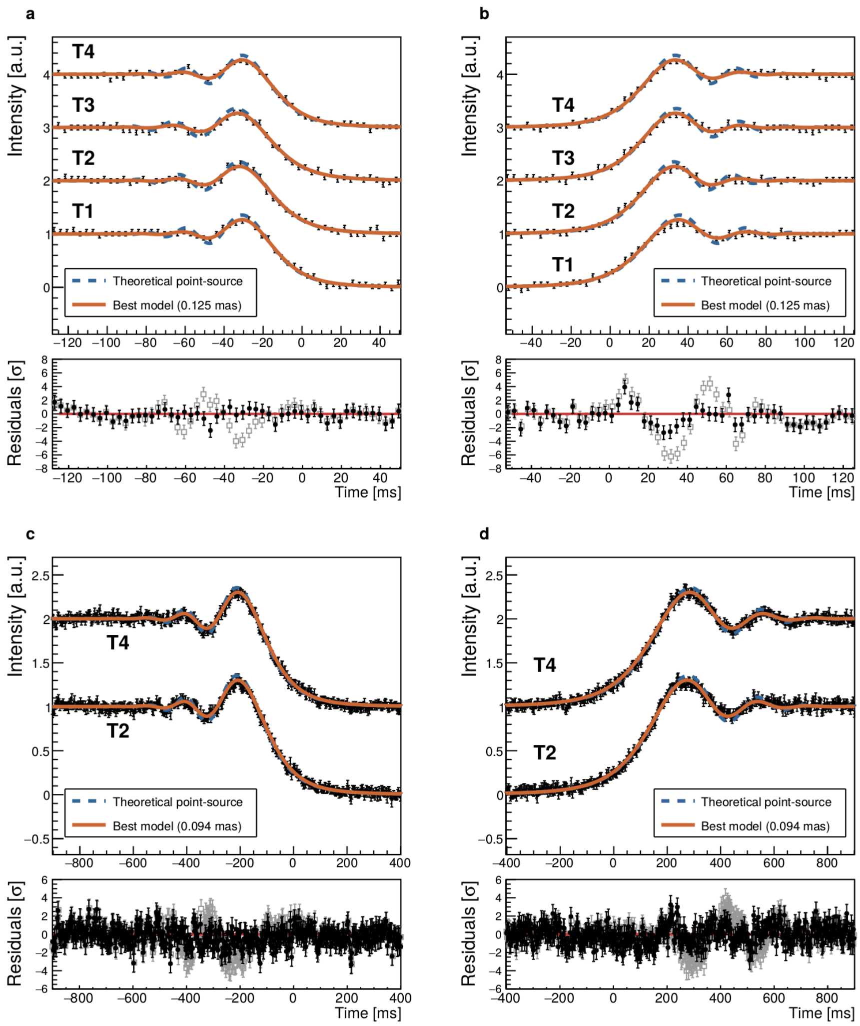

FIGURE 3.3: Light curves for two asteroid occultations measured using the ECM. a) and b) show the ingress and egress of the (1165) Imprinetta / TYC 5517-227-1 occultation. The best-fit diffraction pattern is shown with the red line and theoretical point-source model is shown with the dashed blue line. All light curves are normalized and shift between telescopes is artificially introduced. The residual with respect to the point-source is shown below with grey empty squares and likewise the best-fit residuals are shown with black filled circles. Simile figures are shown for (201) Penelope / TYC278-748-1 in c) and d). Figures are taken from Benbow et al. (2019).

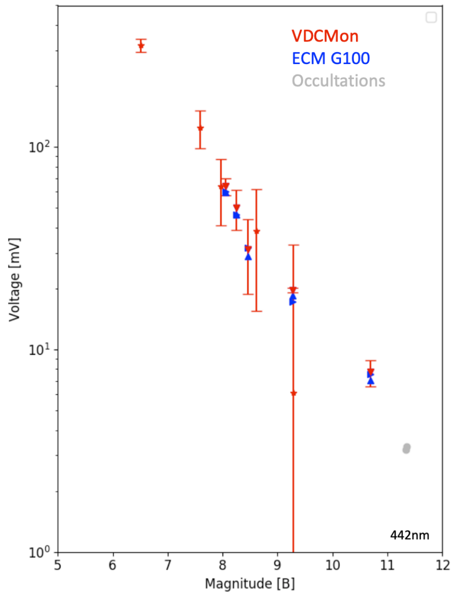

FIGURE 3.4: The flux calibration of the ECM device as compared to the VDCMON. ECM points for the fields observed during the asteroid occultation observations are also included. Magnitude data is collected from SIMBAD (Wenger et al., 2000).

3.3 ECM Flux Calibration

An absolute voltage to magnitude conversion is require for energetics calculations and to understand the sensitivity of the instrument. In order to investigate the sensitivity of the instrument, calibration runs were undertaken where multiple regions of sky were selected where the sum of the stars had a range of effective magnitudes. This has only been completed once and as such it does not take into account variation due to the atmosphere from night to night. The results of this calibration is shown in Figure 3.4. The older VDCMON is shown alongside the ECM with the ECM results for runs used for asteroid occultation studies. The error on the flux calibration is approximately $\sim$10% and an effective limit of the device is $\sim$11 mag but this will change nightly. The ECM has a voltage response linear with brightness.

3.4 ECM Timing Calibration

For previous detection methods timing calibration was not an issue as the FADCs at VERITAS is synchronized with a GPS clock such that all events are labelled with a GPS time-stamp. With the ECM the time-stamps are synced with the CPU clock of the control PC which is neither accurate nor precise. Thus an additional layer needs to be applied to the clock. This timing precision is crucial. Due to the poor spatial resolution of VERITAS as compared to other optical telescopes, a strong temporal association is one of the best ways that a claim can be made. Although the sample rate is precise, the absolute timestamp is what is needed or at a minimum knowledge of the time shift between telescopes.

The best way to synchronize this timestamp is by utilizing the FADC GPS clock timestamp. By finding common events in the FADC data and the ECM data we can synchronize the two clocks. In the early days (2016 to 2019) of data collection this problem was not identified. As such we have to use natural signals in the data for this alignment. In later runs (2019-2020) we can trigger an event in both the FADC and the ECM. Light based triggers were attempted but it was difficult to trigger the FADC while not saturating the ECM. This saturation caused large error in the synchronization. Instead, if the high voltage being supplied to the PMT is reduced then both the current and the traces drop to zero. Since the rest of the pixels in the camera will still be active, events will still be triggered and so there will be events where we can measure this zero trace. This will also occur naturally in a run if a bright star passes through the pixel. Due to the altitude and azimuthal (Alt-Az) VERITAS mount, the camera does experience a field rotation. This means that pixels beyond the center will not be looking at the same patch of sky during an observation. This allows bright stars to pass in and out of the FOV. For gamma-ray observations, having a bright star in a pixel negatively affects shower reconstruction and triggering so there is an automatic threshold that suppresses pixels in software.

The other method that is used is synchronization with meteors in the course of a run. This method works similar to the previous method in that we are correlating the signature in the FADC traces and the ECM. In this case, naturally occurring meteors provide a bright pulse that should be visible in both. The low sensitivity of the FADC requires that these be very bright meteors. The meteor rate will vary throughout the year and the time of night. This means that it is unreliable to use this technique for all runs but it does provide validation and precision in runs where such bright meteors are present.

To actually calculate the time shift one can provide a simple linear interpolation between the points in the FADC and then apply a cross-correlation between the two and take the maximum of the function. A study was conducted to asses this against a method of minimizing residuals in the pedestal variance light curve and treating the ECM as a template and it was found that method was more robust in the cases of large noise in the pedestal variance measurements. However both methods are found to have sub-second precision ($\mathcal{O}(0.1\ \mathrm{s})$).

Due to the unreliably of stars or meteors being present in the field of view, many of the archival ECM runs cannot be calibrated. Once the issue with the CPU clock was discovered, and after initial tests with light based triggering, it was decided that a manual pixel suppression was the ideal form of calibration. The way that this works is that after the ECM data collection is started and the gamma-ray data collection is ongoing, using the HV control it is possible to manually suppress a pixel reducing the HV supplied. The suppression produces a repeatable signature in the data that can be used for the timing calibration. A suppression is triggered at the beginning and end of every run. A suppression event not only provides four points to measure the shift (since both the rise and fall due to the pixel being suppressed and restored can be treated as independent points of reference) but it also provides a measurement of the clock drift throughout the run. For all runs this effect is measured to be less than the systematic error due to calibration.

There is one additional issue which is that the signature of this pixel suppression in the pedestal variance will not be exactly the same as what the ECM is measuring. If we define the pedestal variance as σ^2 then the components that make up the pedestal variance come from the NSB, and the electronic noise such that we can define:

$$\sigma^2 = \sigma^2_{NSB} + \sigma^2_{Elec} \tag{3.1}$$

Now the ECM intensity measurements (I) should only be proportional to the NSB. If we rearrange the above definition and include a linear scaling constant then we find the following relationship:

$$\sigma^2_{NSB} = \sigma^2 - \sigma^2_{Elec} \tag{3.2}$$

$$I = A\sigma^2_{NSB} = K(\sigma^2 - \sigma^2_{Elec}), \tag{3.3}$$

where K can be calculated using data from the run by equating the ranges:

$$K = \frac{< I_{On} > - < I_{Off} >}{< \sigma^2_{On} > - < \sigma^2_{Off} >}, \tag{3.4}$$

where the On and Off define the phases where the pixel is powered and suppressed respectively. The conversion then simply becomes:

$$\sigma^2 = \frac{I}{K} + \sigma^2_{Elec}. \tag{3.5}$$

When the high voltage is lowered there is an additional correction term that needs to be applied. The PMT relative gain (G) will scale as the high voltage is lowered. This is the gain relative to the PMT gain with the HV on. This gain factor can be defined as:

$$I = \frac{K\sigma}{G} \tag{3.6}$$

since G should scale along with the intensity measurements in the ECM. This adds an additional term to the normal conversion:

$$G = \frac{I}{< I_{On} >}, \tag{3.7}$$

$$\sigma = \frac{GI}{K} + \sigma^2_{Elec}, \tag{3.8}$$

$$\sigma = \frac{I^2}{KI_{On}} + \sigma^2_{Elec}. \tag{3.9}$$

One will note that there is an additional intensity term which means that there is a non-linear conversion that needs to be applied to data that occurs during the suppression whereas the normal linear conversion can be applied to the rest of the data. This does induce a timing error $\mathcal{O}(0.1\text{s})$ when it is not taken into account.

For the run taken on November 25th 2017 and example of the timing calibration can be seen in Figure 3.5.

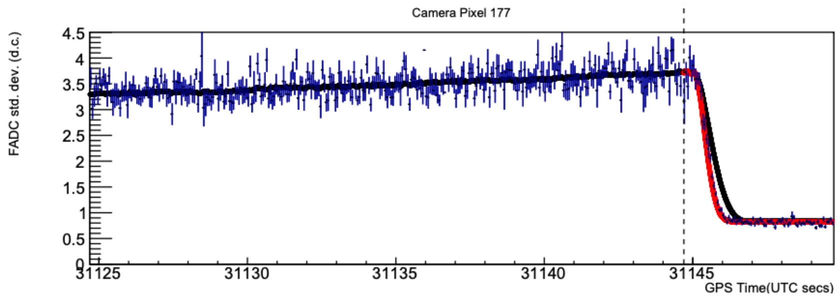

FIGURE 3.5: The alignment of pedestal variances with the ECM data for a pixel suppression event. The uncorrected ECM data is shown in black. The corrected ECM data is shown in red. The pedestal variances are shown in blue. The event shows the ECM after it has been shifted to the GPS time (Holder, Private Communication, 2019).

3.5 ECM Signal Detection

A technique used for the VERITAS signal detection in the ECM is the "matched filter" which in the case of stationary Gaussian noise has been shown to be the optimal detection strategy for transients signals (Helstrom, 1968). In this context stationary refers to a stochastic process whose probability distribution does not change with time. Given a template for an underlying signal in a time series of data, one might expect a cross-correlation to be an effective way of detecting the location of a signal. Although this does work in many cases, a more sensitive technique is to instead take the cross correlation in the noise-weighted frequency domain to help remove the impact of targeted noisy frequencies. This is a well known technique in signal processing known as the matched filter. In order to implement this technique in the context of our optical photometry, we modified the FINDCHIRP algorithm used in the LIGO/VIRGO pipeline (Allen et al., 2012). A description of this is shown in Appendix A.

The key to creating a complete search is the construction of useful templates to use in the correlation. The signal to noise ratio (SNR) should be viewed as the best fit amplitude of the template. This means that templates which do not accurately represent the underlying signal will have erroneous (and possibly meaningless) SNR. This could mean missed signals due to improper templates. In practice the impact of these effects can be mitigated.

For FRB searches the form of the expected optical signal is still not known so to construct templates we use a generic Gaussian. This is motivated by the prompt emission of other systems being well approximated by a Gaussian as well as the prompt emission from the SGR bursts being well modelled by a series of Gaussian templates. We also survey a variety of timescales by using logarithmically spaced Gaussian widths. That is, we take a Gaussian of the form:

$$g(x) = \frac{1}{\sigma\sqrt{2\pi}} e^{-\frac{1}{2}\left(\frac{t}{\sigma}\right)^2} \tag{3.10}$$

,

then we can generate templates of σ =[0.01,0.1,1] seconds. The number of templates is limited to three so as to minimize the impact of the look-elsewhere effect. There is a loss in detection sensitivity due to using an improper template; one could eliminate this by just having an arbitrarily dense grid of templates to optimize over. Using a series of logarithmically spaced bins over a range of templates and accounting for the look-elsewhere effect, we found that increasing beyond three templates had a significant trials penalty that was greater than the benefit of a finely sampled grid of templates. As such we opted to use only three templates for all ECM transit searches. The results of the matched filter for one template can be seen in Figure 4.8.

The above section describes the optimal matched filtering method that is used. A simpler method is used as a cross-check to ensure that assumptions about the template do not miss transients that would be obvious to a less sensitive but more robust search. This takes the form of generic "mean filtering". This technique simply considers the noise to be normally distributed over small time periods: large non-stationary effects should not dominate on small time scales as compared to prompt transients and so we can treat the noise as stationary and normally distributed within these small windows. With this assumption, one can assess the significance of a data point by subtracting the mean value and dividing the remainder by the standard deviation in the window. Each window has a width of 1000 points (roughly $\pm$ 1s in our standard ECM sampling rate).

Chapter 4

Results

4.1 Observations

Data for the FRB survey at VERITAS was accumulated between September 2016 and February 2020. The data is not evenly distributed across this time period, and instead heavily favors the later years. The data comes from all periods in a year except the summer months, as VERITAS is routinely closed in the summer due to the weather. This data is accumulated by daily monitoring on each of the repeaters for the duration of their transit through the CHIME FOV. Thus, based on right ascension (RA), some sources will have longer exposures than others. Each of these runs lasts $\mathcal{O}(10\text{ minutes})$. These runs are taken in ON mode: the object is centered in the VERITAS FOV. Five FRB repeaters are studied here. The selection criteria of these sources was based on the observed burst rate in CHIME. The properties of these sources can be seen in Table 4.1. A cumulative summary of the observations can be seen in Table 4.2.

In this data set there exist two runs with a CHIME FRB occurring during the run. One burst originates from FRB 180814.J0422+73 on 2019-10-29 09:41:58.675691 (UTC). The second originates from FRB 180916.J0158+65 on 2019-12-18 04:09:27.633 (UTC). In addition there were three "near misses" for bursts from FRB 180916.J0158+65. "Near misses" are bursts that occur within 15 minutes of a VERITAS observations. "Near misses" were primarily due to runs ending before a source fully exited the CHIME FOV. These bursts occurred at the following times: 2019-10-30 07:33:56.995676

TABLE 4.1: Properties of the FRBs Observed by VERITAS.

FRB Name	RA[c]	Dec[c]	Number of Bursts[a]	DM (pc cm^{-3}) [b]
FRB 121102	05:31:58.70	33:08:52.5	19	565
FRB 180814.J0422+73	04:22	+73:40	6	189.5 ± 4.9
FRB 180916.J0158+65	01:58	+65:44	38	349.8 ± 2.8
FRB 181030.J1054+73	10:54	+73:44	2	103.5 ± 1.7
FRB 190116.J1249+27	12:49	+27:09	2	443.8 ± 0.7

[a] Burst numbers are taken from FRBCAT, where many published bursts are organized. It is not a comprehensive list and so this should be viewed as a lower limit on the number of bursts.
[b] Dispersion measures are taken from FRBCAT, and from CHIME. In the case where a burst is well localized, the DM is selected from the well localized burst. In all other cases the automated CHIME DM is used.
[c] Coordinates are taken from the best localized burst in FRBCAT, or in the case that no precise localization has been made, the CHIME automated coordinates are used.
Data in this table taken from: (Andersen, K. Bandura, et al., 2019, Amiri, Andersen, K. M. Bandura, Bhardwaj, P. J. Boyle, Brar, Chawla, T. Chen, Cliche, Cubranic, Deng, Denman, Dobbs, Dong, Fandino, et al., 2020b, Amiri, K. Bandura, Bhardwaj, Boubel, Boyce, Boyle, . Brar, et al., 2019a)

(UTC), 2019-10-30 07:41:52.755579 (UTC), 2020-01-20 01:49:14.068 (UTC). For the simultaneous burst with FRB 180814.J0422+73, since the repeater has not been localized to a host galaxy, it is unclear if the optical data overlaps with the source position. For FRB 180916.J0158+65, the optical data was taken prior to localization, and the pixels monitored do not overlap with the source position. Optical data for both sources were taken with a sampling rate of 2400 Hz with two pixels being monitored.

An additional series of observations of FRB 121102 were taken simultaneously with the Green Bank Telescope (GBT). During this time eighteen bursts were observed by GBT. Of these, seventeen have simultaneous VERITAS ECM and gamma-ray data. The ECM at this time was only installed on the first telescope, T1. The ECM was monitoring 12 channels, at a 300 Hz sampling rate.

All analysis is completed using a combination of the VERITAS data analysis software (VEGAS) and a series of custom python scripts. All the subsequent analysis uses "soft" cuts, which are a series of cuts to optimize gamma/hadron separation for sources with soft spectra. In gamma-ray astronomy most spectra are well modeled by a power law. The index of that power law is often described as soft if it is greater than 2. We expect FRB spectra to be soft as many of the photons will be scattered as they propagate through extragalactic space.

TABLE 4.2: Summary of VERITAS Observations of FRBs.

FRB Name	Exposure (min)	On Counts	Off Counts	Significance(σ)
FRB 121102	1216.64	1681	14134	-0.61
FRB 180814.J0422+73	1013.22	966	8955	-0.62
FRB 180916.J0158+65	397.45	522	4907	-0.06
FRB 181030.J1054+73	226.26	277	2650	-0.33
FRB 190116.J1249+27	45.00	111	768	0.83

4.2 Gamma-ray Significances

In order to place limits on gamma-ray emission one must first recognize what physical quantities we are actually trying to constrain. This may seem trivial but is sometimes poorly tackled in the literature and leads to misinterpreted limits and conflicts. A common example of this is taking integrated limits over a long observing period and interpreting it as constraining all bursts of that given flux value occurring throughout the period of the observation. A simple misunderstanding like this can be alleviated by clarifying one's assumptions and outlining one's technique which we explicitly attempt to do in the subsequent sections.

All of the analysis here relies on background data collected through the ring background method (RBM). A ring of equidistant background regions is taken around the source location. The size of the regions is defined by the PSF of the instrument, equal in size to the ON region around the source. An α parameter is calculated, which is the ratio of sizes between the central region and the sum of the background regions (an α of 0.2 corresponds to 5 background regions equal in size to the region of study). References to OFF counts are to counts that fall in these background regions. Once these background regions are defined, and α is calculated, significances are determined according to the equation outlined by T. Li and Ma (1983).

4.2.1 Persistent Emission Upper Limits

A test for persistent emission is a test of the time-averaged flux over the entire duration of the observation. For variable sources this test does not constrain short periods of high activity. This means that sources can exceed this upper limit (UL) during the observation while the average still remains below the limit. Instead of a test for prompt emission, this tests whether FRBs occur in the proximity of persistent VHE sources (like AGN). A summary of the persistent analysis significance for all FRBs studied is shown in Table 4.2. In the case of well-localized FRBs this significance is reported at the location of the host galaxy. If the source has only been detected by CHIME, then the best fit position is used instead.

None of these sources showed significant emission in the visible range (being defined as an excess of 5σ). Sky maps are shown for all sources in Appendix B. Examples of these figures are shown in Figures 4.1, 4.2.

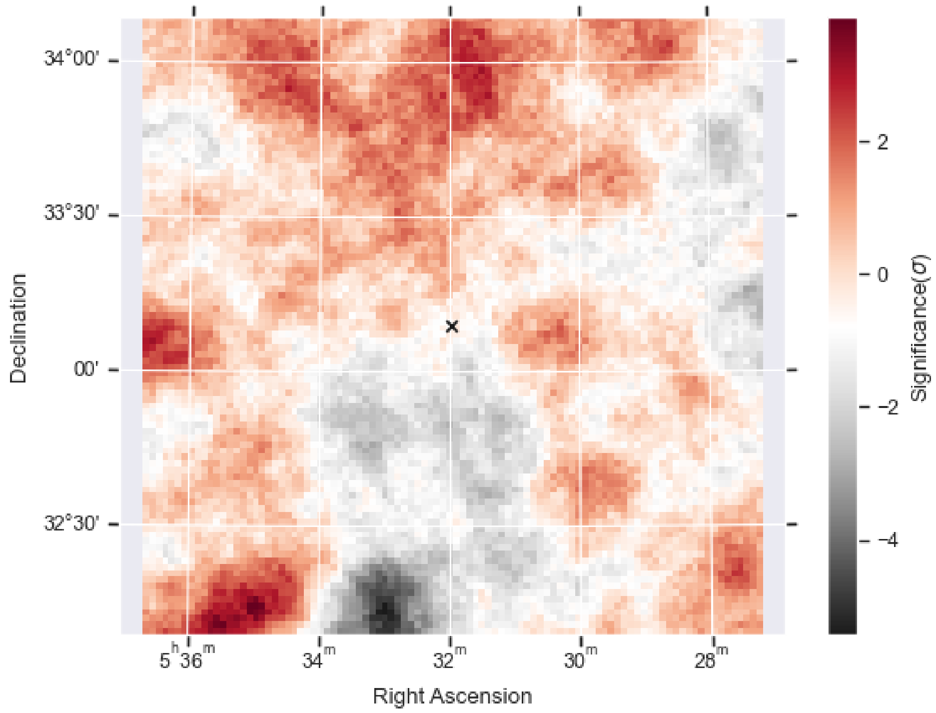

FIGURE 4.1: Significance map of FRB 121102. More information on this figure is shown in Appendix B.

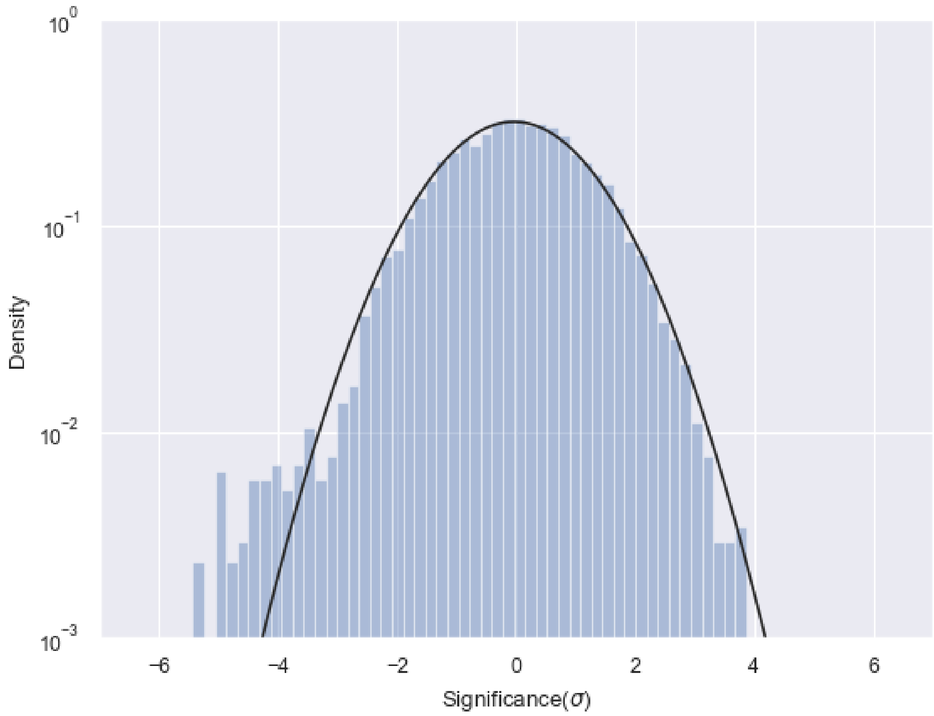

FIGURE 4.2: Significance distribution of FRB 121102. More information on this figure is shown in Appendix B.

In these sky maps, it is also shown that for non-localized sources there is no significant emission at any point within the error region provided by CHIME. In the case of an empty field, these should be normally distributed. In these figures it is clear that all of the distributions are well modeled by a Gaussian.

When it comes to translating these non-detections into upper limits one needs to take into account the effective area of the VERITAS instrument and the observation time. New VERITAS effective areas have been computed every time the instrument has had a major upgrade. Unfortunately, due to degradation of the instrument over time, the current generation of effective areas do not accurately reflect the true performance of the instrument. This causes systematic error in flux calculations on the order of ∼50%. There is currently work ongoing in the collaboration to model and account for this degradation in future analyses, but this is still in progress. As such, no precise flux calculations will be presented in this thesis due to the large systematic errors that affect the results. Instead we present order of magnitude upper limits in Table 4.3.

TABLE 4.3: VERITAS upper limits for the persistent emission from the FRB repeaters.

FRB Name	Integral Upper Limit ($m^{-2}s^{-1}$)
FRB 121102	$\sim 10^{-8}$
FRB 180814.J0422+73	$\sim 10^{-8}$
FRB 180916.J0158+65	$\sim 10^{-7}$
FRB 181030.J1054+73	$\sim 10^{-7}$
FRB 190116.J1249+27	$\sim 10^{-6}$

4.2.2 Burst Significance Upper Limits

Issues arise when placing limits on the prompt gamma-ray emission from a burst, primarily because the cuts one applies require model dependent assumptions. Many unknowns exist about the nature of high-energy FRB counterparts, which means a large range of possible cut values. In order to minimize background we place a time cut on the region investigated within a run. Ideally, one would want the duration time cut to match the expected duration of the emission. Since the duration of the expected emission is unknown, one must instead scan over multiple time scales. This causes a sacrifice to the sensitivity due to the "look elsewhere effect". The "look elsewhere effect" is a statistical statement that the larger the range of parameter space one considers, the more likely one is to encounter a large statistical fluctuation that mimics a real signal.

Due to this "look elsewhere effect" one cannot simply quote the significance of an event without stating the number of observations one has made. One approach, commonoly used in particle physics is to evaluate the so-called "trials factor", and to incorporate a penalty to the significance of the test depending on the number of subtests (trials). This give:

$$P_{\text{post-trial}} = 1 - (1 - P_{\text{pre-trial}})^{N_T}, \tag{4.1}$$

where $P_{\text{pre-trial}}$ is the pre-trial probability and N_T is the number of trials. This formula is derived assuming binomial statistics. As this post-trial probability increases, the significance will decrease. If one Taylor expands in the limit of small probabilities then $P_{\text{post-trial}} \sim N_T \times P_{\text{pre-trial}}$. The number of trials within this thesis will directly correspond to the number of cuts used.

Because there is now a penalty on the number of cuts, the optimal search involves minimizing the number of trials while still ensuring they adequately probe the unknown parameter space. In the burst-limit analysis we investigate five logarithmically scaled times around each burst (0.1 s, 1 s, 10 s, 100 s, full-run). After taking the burst time, applying a barycentric correction using Astropy (Astropy Collaboration et al., 2018) and applying a DM timing correction we can then apply each time cut. This corresponds to five trials.

There is currently only one run where it makes sense to apply this burst analysis. This is the burst simultaneous with FRB 180916.J0158+65 on 2019-12-18 04:09:27.633 (UTC). For the burst from FRB 180814.J0422+73 one could apply the analysis to the region of best fit, but since the gamma-ray PSF is only $\sim$0.13° in diameter and the error region provided by CHIME is over half a degree in size it is not certain that the FRB would fall in the ON region selected. This being said, a preliminary burst analysis was performed and no significant emission was detected in any time bin for this burst. Analysis similar to what will be shown for FRB 180916.J0158+65 will be performed on FRB 180814.J0422+73 if it becomes localized.

For the burst from FRB 180916.J0158+65, we can be confident in our ON region and OFF regions. The OFF event rate over the run was calculated to be 0.019 ± 0.001 events/s. We will assume that over the course of this short run (900 s) that this rate does not change. This can be confirmed by looking at the L3 trigger rate which does not vary by over 5% throughout the entire run. A plot showing the temporal distribution of the ON events can be seen in Figure 4.3. A summary of each of the time bins can be seen in Table 4.4. As no significant emission can be seen in any of the bins, a photon upper limit is placed in each of the time bins in the same table. For the same reason that only order of magnitude ULs are presented earlier, the upper limits in this analysis will not be converted into an energy flux.

4.2.3 Significance in the case of a burst forest

In the case of a burst forest analysis, assessing significance becomes more difficult. A "burst forest" in this context is when multiple distinct FRBs occur over a short period. In our case it is 17 bursts in under an hour during the coordinated campaign

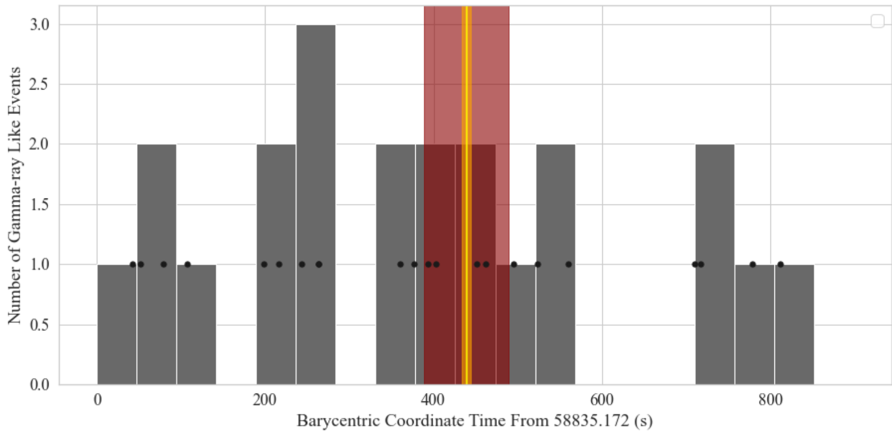

FIGURE 4.3: Burst analysis for FRB 180916.J0158+65. All times have been barycentered and DM corrected when appropriate. The times of ON events are shown as black circles. A gray histogram of the ON event times is shown for visual clarity of the density. The CHIME burst is shown as a yellow line. Surrounding that burst the regions selected for the time cuts are shown in red and orange (100s, 10s). The time cuts for 0.1 s and 1 s are not shown as no events fall in the 10 s bin.

Time Cut (s)	On Events	Off Events	Significance (σ)	95% Upper Limit (Counts)
0.1	0	0.0019	-0.05	3.0
1	0	0.019	-0.16	3.0
10	0	0.19	-0.51	3.0
100	4	1.9	0.87	9.43
900	22	19	0.47	32.8

TABLE 4.4: Summary table of the burst analysis for FRB 180916.J0158+65. Upper limits are calculated using the confidence intervals from Feldman and Cousins (Feldman et al., 1998) or Poissonian limits are taken when the background is considered negligible (below 0.5 events).

between VERITAS and GBT on FRB 121102. Due to the exceptional nature of the data set, a unique analysis was performed on this run.

When looking at each of these bursts individually, one cannot simply apply a series of time cuts around each burst to assess the significance of the emission, due to the trials factor. Since all of these cuts are being applied to the same data, proceeding in this was for every burst would significantly decrease the sensitivity of any detection. Instead, we seek to minimize the trials by analyzing the entire data set at once in order to maintain the sensitivity of the search.

To do this, the simplest approach is to stack the bursts. For each burst, we shift the events such that the burst time occurs at time zero; we then sum together each of these individually shifted event lists. In the case that all the events were independent, this owuld be sufficient. Because the events are correlated, issues arise due to over-counting events. Minor clustering will be amplified when FRBs occur in tight clumps. In order to account for this effect, we perform the same action on a measured background. While OFF events can provide such background, the low event rates cause statistical issues. The simplest approach would be to assume a constant background rate of OFF events throughout the run and assess the significance of each bin against that average rate. However, in the case of the burst forest data set, the rate of cosmic rays triggers is not constant over the course of the entire run and thus the background rate is also unlikely to be constant through the run. A more accurate approach would dynamically model the rate based on a proxy of the gamma-like event rate that has higher statistics.

To do this, we take the total number of OFF events from the RBM analysis and calculate an average rate. Then we generate a large number of random backgrounds from the cosmic ray events in the full camera that match this overall average rate. These are generated by selecting a random list of N_{off} events from the full event list. This normalization will ensure that the acceptance of the camera is taken into account. The OFF event rate should not be viewed as a rate of gamma-rays, but as the rate of gamma-like cosmic rays convolved with the acceptance of the camera. Thus, once the average rate is obtained from the OFF region using the full camera to increase the statistics is well motivated. If we repeat this process many times we can generate an accurate background estimate for a series of time-bins across the run.

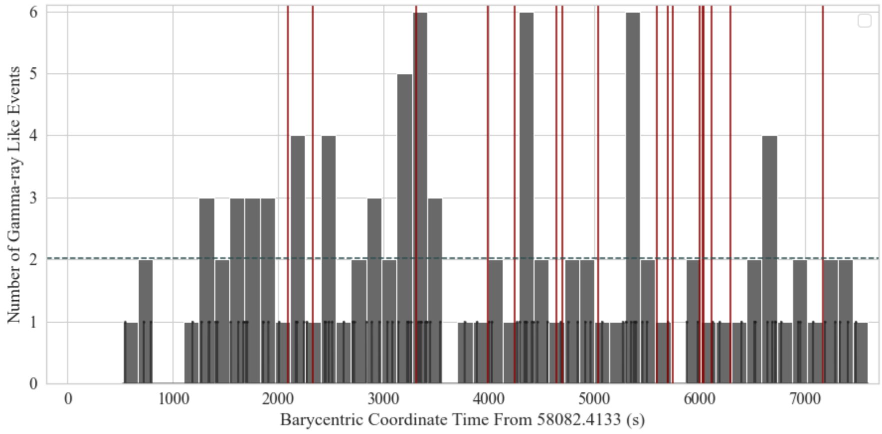

FIGURE 4.4: VERITAS gamma-ray candidate event counts for the FRB 121102 burst forest observed by GBT. Time is taken from MJD 58082.4133. The gray bars compose a histogram of the arrival times of the barycentric gamma-ray candidate event counts. The exact times of the events are shown in black. Red lines show the dispersion corrected barycentric arrival times of the FRBs observed by GBT. The dashed slate line shows the average background rate expected for each histogram bin.

Then, binning the data and this background in the same time bins, the significance of the emission can be assessed in each bin. The un-stacked background and data can be seen in Figure 4.4.

Once the data is shifted and stacked the significance of any excess, assuming a poissonian distribution in each bin, can be assessed (see Figure 4.5). An additional test can be performed by applying a Kolmogorov–Smirnov test to these two distributions. This test would reveal any emission, whether it be prompt or delayed, across any time scale contained between the minimum time bin and half the duration of the run. When such a test is performed for the data set we obtain a p-value of 0.20 indicating that these two distributions are drawn from the same PDF. Thus, here is no evidence for significant VHE emission associated with this cluster of FRBs at timescales less than $\sim$3500 s.

4.3 Optical limits

To set limits on optical emission using the ECM, we have to shift statistical regimes from the counting to the continuous regime. The large numbers of optical photons measured in the ECM means that we are no longer counting individual photons

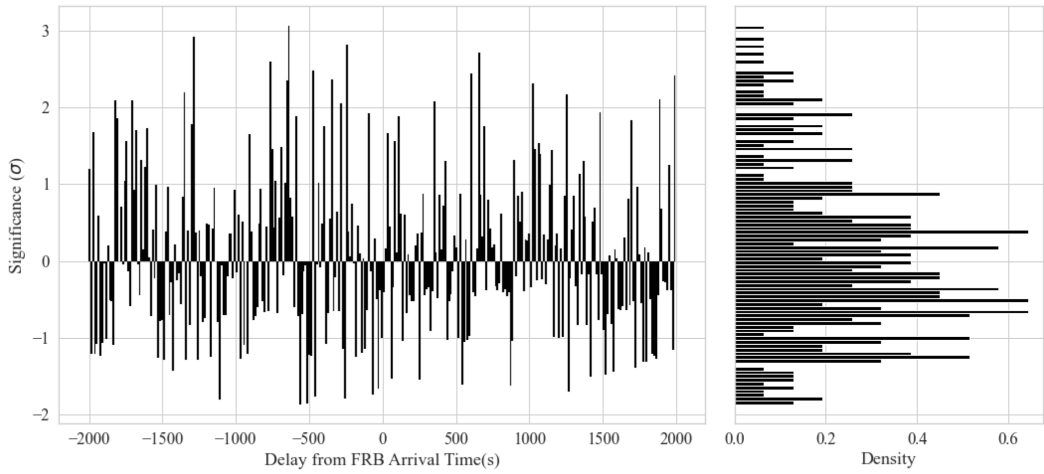

FIGURE 4.5: The VERITAS significance of delayed emission from the stacked analysis of the FRB 121102 burst forest. In the left panel, the significance of each bin between -2000s and 2000s is shown. In the right panel, the distributions of the binned significances is presented. In all bins, there is no evidence of significant prompt, or delayed emission.

but instead we are measuring a continuous signal. This means our techniques for measuring the upper limits will change as well depending on how we assess our background. Recall, that in the case of gamma-rays we used OFF regions with similar sensitivity to gamma-rays as our source locations as a proper measure of the background. In the ECM, there are broadly two classes of background we need to consider. These backgrounds can be seen in Figures 4.6 and 4.7. The first is dynamic backgrounds. Due to the large pixel size, the ECM measures an integrated signal over a large patch of sky containing many background sources. These, in addition to the changing night sky background (NSB), form a baseline below which we cannot probe. The level of this baseline will change depending on our pointing as new background sources enter the FOV and the sky conditions change. The sky cannot be considered isotropic at the resolution we are probing so selecting a spatial OFF region as in the case of the gamma-rays will not precisely probe this baseline. We can instead select a temporal OFF region, measuring the baseline in a period of time not under investigation. This assumes that the noise is stationary over time.

Numerous terrestrial or anthropogenic effects sometimes cause entire runs to be unusable. These are typically effects that slowly vary throughout a run and affect the entire camera. The most common of these backgrounds are clouds. Depending

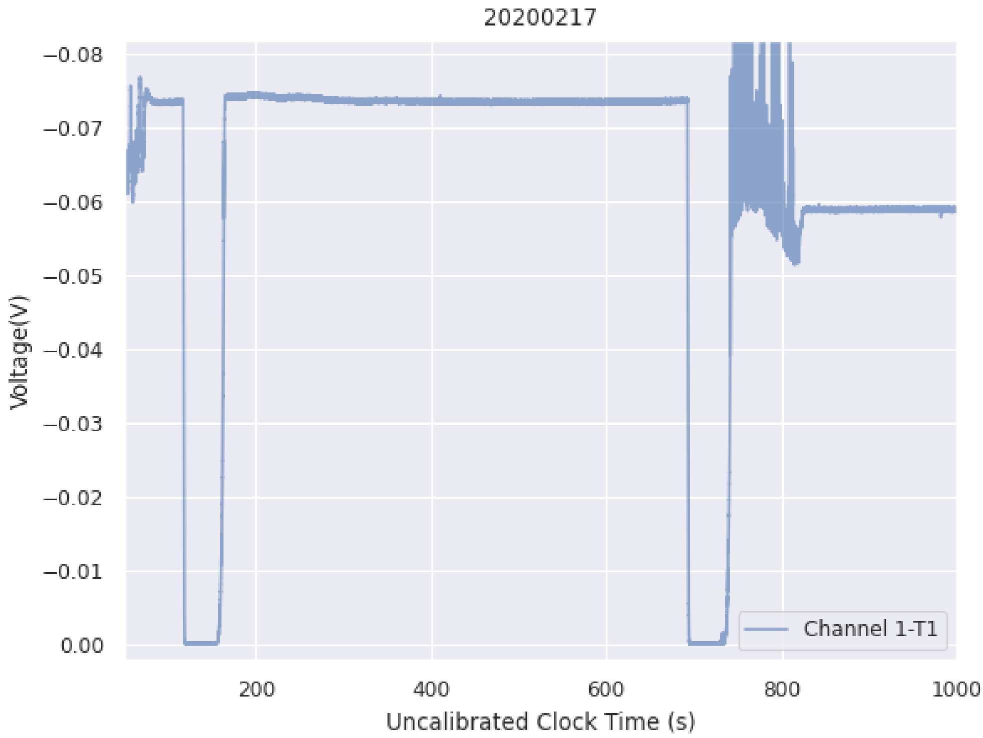

FIGURE 4.6: An ECM light curve for a typical low noise ECM run prior to corrections. The pixel suppression events are clear showing the time of the active region. The active region remains flat until the end of the run. The prominent gaps are caused by the manual pixel suppression that is used for timing calibration.

on the nature of the clouds the effects are can be varied. Clouds normally have a large spatial extent and so having a pixel outside of the ON region can help quantify these effects. Ideally one would like a complete "guard ring" composed of all of the pixels surrounding the ON pixel. With the current generation of the ECM this is not possible without a large sacrifice to the sample rate of the central pixel. A compromise was reached to instead select a single pixel as a background monitor.

The second type of background is instrumental. These are effects that last throughout the run and affect the sensitivity of the instrument. Instrumental backgrounds come from a variety of sources that do not need to be localized to be removed. These manifest themselves in the power spectral density of the run. An example is electrical noise causing a continuous 120 Hz signal to appear in the data. By modeling the power spectral density of a run and using a smoothing function we can quantify a noise matrix that encapsulates these persistent backgrounds and remove them.

The pixel used as a background monitor can be used in connection with normal

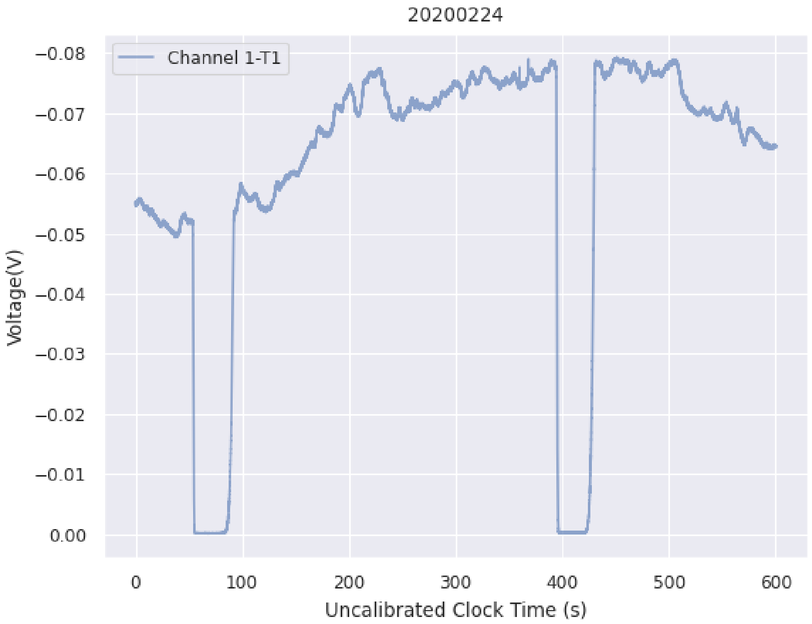

FIGURE 4.7: A light curve for FRB 121102 in a case where clouds dominate the background as indicated by the variance of the data series.

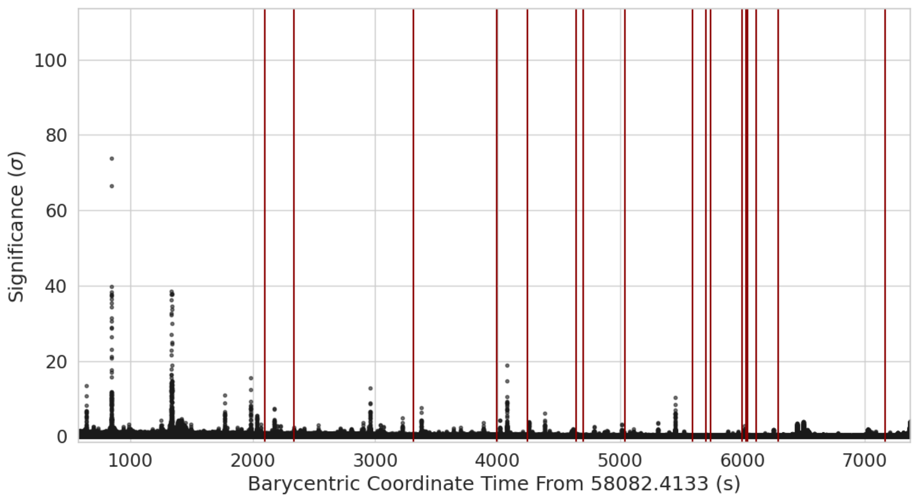

FIGURE 4.8: Results of applying the matched filter analysis on the FRB 121102 burst forest ECM data from the central pixel of VERITAS. Time is taken from MJD 58082.4133. The barycentric FRB times from GBT are shown in red.The results of the matched filter are shown in black.

weather monitoring to quantify what parts of a run are unusable due to weather. Runs in stable atmospheric conditions contain no large-scale correlated noise and so areas in a run with a large standard deviation of voltages can be targeted and removed as weather-related issues. In addition, at the VERITAS site there exists an array of equipment to monitor atmospheric conditions; manual labelling of conditions is done on a run-by-run basis to flag runs that require a more careful analysis due to weather. This equipment includes a lidar, an all sky CCD camera, and two infrared radiation pyrometers attached to separate telescopes.

Once the run is identified to contain no large dynamic background and the electronic backgrounds are removed the baseline is measured and the sensitivity of the instrument for that run can be calculated. This is done on a run by run basis and has a 15% error due to the variation in the flux calibration.

Currently, the only run with relevant analysis to be performed in terms of optical limits is the FRB 121102 burst forest (since the other two runs with bursts have an FRB that fell outside the central pixel or the FRB was not well localized). In this run the matched filter described in Chapter 3 has been applied after cleaning. The results are being shown in Figure 4.8. The transients seen in the figure can be attributed to meteors with the rate being consistent with the background pixel. There are 90 events over 10 σ in the central pixel which is consistent with the 91 events measured in the background pixel. Within a 10 s window of all the FRBs no significant outlier is detected. The sensitivity during this run was calculated to be $\sim$11 mag in the B band.

In this chapter we described some of the techniques used and limits placed by VERITAS on the optical and gamma-ray emission in FRBs. In all cases there was no significant emission detected by VERITAS. Depending on the data the challenges with assessing significance were also outlined. Integral upper limits placed on the persistent emission ranged from $10^{-6} \longrightarrow 10^{-8}$ m $^{-2}$ s^{-1} at 95% confidence level. No gamma-ray emission was observed simultaneously with a FRB burst with 95% upper limits on the counts ranging from 3.0 $\longrightarrow$ 32.8 in time bins of 0.1 s to 900 s. No optical bursts were detected above $\sim$11 mag in the B band. Context for these limits will be provided in subsequent chapters.

Chapter 5

Discussion

5.1 Other Observations

The closest comparison to the limits presented in this paper are the results from the MAGIC IACT (MAGIC Collaboration, Acciari, Ansoldi, Antonelli, Arbet Engels, Arcaro, et al., 2018). The MAGIC telescope observed FRB 121102 with dedicated Arecibo observations over several epochs from 2016 to 2017. Five FRBs were detected in by CHIME during their campaign. Their average integral flux upper limits in the VHE regime above 100 GeV (95% confidence level) were 6.6×10^{-12} photons cm^{-2} s^{-1}. The gamma-ray limits can be seen in context in Figure 5.1. In addition, the MAGIC central pixel optical monitor constrained the U-band flux to be below 8.6 mJy for 1-ms intervals. The challenge that MAGIC faces with these observations is scalability. Although our current limits are at comparable levels with the limits published by MAGIC, MAGIC requires dedicated pointed observation from large radio telescopes like Arecibo [1] or time on a comparable radio telescope in order to confirm how many FRBs occurred during their run. This requires the FRB to be a localized (due to the small FOV of these instruments) repeater. The method and techniques shown in this thesis have much greater potential. The limits are placed on a variety of repeaters across a range of distances without the need of dedicated radio telescope coordination. As this thesis demonstrates, these observations are already practical for VERITAS and are in the process of being collected.

The other major IACT, H.E.S.S., has also presented early FRB results (H. E. S. S.

[1] This may be even more challenging due to recent developments (http://www.naic.edu/ao/blog/broken-cable-damages-arecibo-observatory)

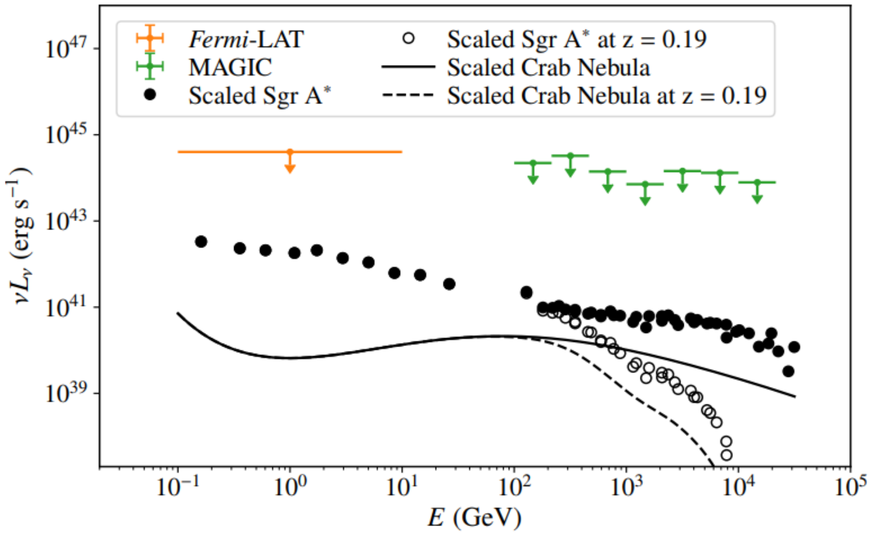

FIGURE 5.1: Upper limits of the luminosity of FRB 121102 from MAGIC. Limits from *Fermi*-LAT limits are shown in addition to several scaled references. Sources are scaled to the approximate distance of FRB 121102. The distance of FRB 121102 causes these scaled sources to fall well below the MAGIC limits. Figure is taken from (MAGIC Collaboration, Acciari, Ansoldi, Antonelli, Arbet Engels, Arcaro, et al., 2018).

Collaboration, Abdalla, Abramowski, Aharonian, Ait Benkhali, Akhperjanian, Andersson, et al., 2017). Unfortunately for H.E.S.S, which is located in the southern hemisphere, most of the recent FRB detections are being driven by telescopes located in the Northern latitudes. They followed up the early FRB 150418 for 1.4 hours, 14.5 hours after the FRB was detected by Parkes. Since most FRBs are not circulated in the GCN or a similar network, this delay is typical of alerts that are often released via Astronomical Telegrams. H.E.S.S. reported significant VHE emission. Therefore, 99% upper limits were placed above 350 GeV at $1.33 \times 10^{-8}\mathrm{m}^{-2}\mathrm{s}^{-1}$. This is an example of how delayed follow-up observation by IACTs are not very constraining. Since magnetar-like models should only have a prompt VHE emission, this upper limit does not help to constrain those models. Since that early work H.E.S.S. has only reported an observation during the SGR 1935+2154 burst forest. This observation did not overlap with the FRB burst.

Other instruments for comparison to the VHE results are the *Fermi*-LAT (Atwood et al., 2009) and the *Fermi*-GBM instrument (von Kienlin et al., 2020). Data from the *Fermi* instruments are publicly available for analysis. This has resulted in a large number of independent analyses that have attempted to detect FRBs. In spite of the number of studies there is no evidence that *Fermi* has detected a GeV counterpart to an FRB. The following section discusses some of these studies. The first type of survey investigates *Fermi*-LAT data around known FRB positions.

5.1.1 Some Selected *Fermi* Studies

- A search for emission from 38 non-repeating FRBs was done in *Fermi*-LAT (Martone et al., 2019). They found no significant emission from any of the sources in their sample. Fluence upper limits were placed in the energy range 8-1000 keV equal to 6.4×10^{-7} erg cm^{-2} for a 200 s integration time. In addition, a 1 s upper limit in the same energy regime was placed at 7.1×10^{-8} erg cm^{-2} (5 σ confidence level). This corresponds to a radio-to-gamma fluence ratio of $\eta > 10^8$ Jy ms erg^{-1}.

- A smaller targeted search investigated 3 bursts from FRB 121102 in the energy range 10-100 keV (Younes et al., 2016). They did not detect any significant emission. Assuming a 0.2 s pulse, they placed an upper limit of $1.0{\times}10^{-7}$ erg s^{-1} cm^{-2} (5 σ confidence level).

- An eight year study of FRB 121102 was also conducted. No significant emission was detected in the region of this FRB from 2009 to 2016. This led to a energy flux limit of 4.05×10^{-12} erg cm^{-2} s^{-1} at the 95% confidence level (B.-B. Zhang et al., 2017) on the persistent emission from 100 MeV to 10 GeV. Both the burst survey and the persistent analysis show no evidence of GeV emission from the region of FRB 121102.

- Other FRB repeaters have also been followed-up. This includes the second repeater, FRB 180814 J0422+73 (Yang et al., 2019). Using ten years of *Fermi* data, the survey did not detect any significant emission from 100 MeV-10 GeV. This resulted in an upper limit on the persistent emission of 2.35×10^{-12} erg cm^{-2}s^{-1} (95% confidence level). In addition, there was a upper limit placed on the emission in each 6 month interval ($\sim 10 \times 10^{-11}$erg cm^{-2}s^{-1}).

- FRB 131104, the potential *Swift* candidate, was also investigated for late afterglow emission in *Fermi*-LAT (Xi et al., 2017). Although the candidate was most likely a sub-threshold AGN flare, a detection in *Fermi* would have helped to confirm the burst location and properties. The burst was investigated ∼5000-s after the potential detection when it entered the *Fermi*-LAT field of view. No significant emission was detected, although the delay makes this an expected result. An upper limit was placed on the fluence of this burst afterglow at 29.2 $\times 10^{-7}$ erg cm^{-2} (95% confidence level).

- Although none of the follow-ups of known repeaters have yielded a detection, some studies have attempted to perform a blind candidate search using *Fermi*. In (Yamasaki et al., 2016) the search looked for candidates that were not previously associated with any known source and tried to associate them with FRBs. In cases where no candidates were found, the flux was assessed ratio based on the all-sky FRB rate. After the analysis was completed they noted that no event, was found in non-galactic latitudes that passed their candidate cuts. Since no candidates were found they placed an upper limit on the gamma-ray to radio flux ratio of $\eta = 12 \times 10^7$.

Another type of analysis that has been performed is using archival data from SGR 1935+2154. One can place limits on the fluence ratio between bursts from the gamma-ray side based on radio non-detections. A campaign using *Insight*-HXMT, BOOTES, and FAST measured the fluence ratio between detected bursts from SGR 1935+2154 (Lin et al., 2020). Since this survey recorded optical data simultaneously with the CHIME detected burst it is of particularly interesting. No radio or optical counterpart were detected for any of the 29 SGR bursts observed in the X-ray band. No optical emission was detected by BOOTES-3 simultaneous with FRB 200428 above 17.9 magnitude for a 60 s exposure. The 29 bursts seemed to be nominal for SGR 1935+2154, as was the *Insight*-HMXT burst simultaneously with FRB 200428. The radio fluence limit placed by FAST on bursts from 1-20 ms, was 10-50 mJy ms.

Another relevant study is related to neutrino associations. The non-thermal production of VHE gamma-rays may be tied to neutrino production through hadronic processes. Therefore, if one makes an assumption that the non-thermal emission in FRBs is hadronic, one can place limits on the neutrino production through the

VHE limits, or the reverse. The most sensitive neutrino experiment for astronomical TeV neutrinos is currently IceCube (IceCube Collaboration et al., 2006). IceCube conducted a survey of 28 FRBs and one repeater (FRB 121102) and found no significant detection of neutrinos in the MeV or at energies greater than ∼50 GeV (Aartsen et al., 2020). This allowed them to set (90% confidence level) upper limits at $E^2F < 2 \times 10^{-3}$ GeV cm^{-2} per burst. This analysis was performed using a 10 second window around the FRBs. This is not a constraining limit for the VHE observations, however, the limits presented in this thesis could be used to constrain the expected background neutrino rate from FRBs.

In summary, the results presented in this thesis are compatible with the literature and are not in tension with any of the surveys performed.

5.2 Comparison of our results with current SGR detections

Magnetars exhibit a variety of flares and due to the rarity of these sources and the different properties of these flares it is difficult to make absolute statements about the range of potential emissions from these sources. H.E.S.S. has a potential VHE detection in the vicinity of SGR 1900+14 and SGR1806-20 but no detections associated with contemporaneous flares (Hnatyk et al., 2020; H. E. S. S. Collaboration, Abdalla, Abramowski, Aharonian, Ait Benkhali, Akhperjanian, Angüner, et al., 2018). The detection by INTEGRAL and *Insight*-HMXT of a magnetar burst simultaneously with a FRB was particularly surprising in the context of previous limits on radio emission from magnetar giant outbursts (Mereghetti, Savchenko, Ferrigno, Götz, et al., 2020a). A comparison of the flux ratio from this detection along with previous non-detections is shown in Figure 5.2. It appears as if it is not a property of all SGR bursts to produce a FRB, but rather a unique subset. Although it appears as if the emission detected during these bursts is non-thermal, the underlying mechanism still remains ambiguous. TeV emission is suspected to be possible during magnetar flares (Halzen et al., 2005). VHE gamma-rays could be produced in hadronic interactions with thermal radiation produced during these flares. These interactions could occur in surrounding material or a fallback disk. The VHE flux predicted during "giant flares" is $\mathcal{O}(100\text{Crab})$ but it is less clear what is expected during smaller flares

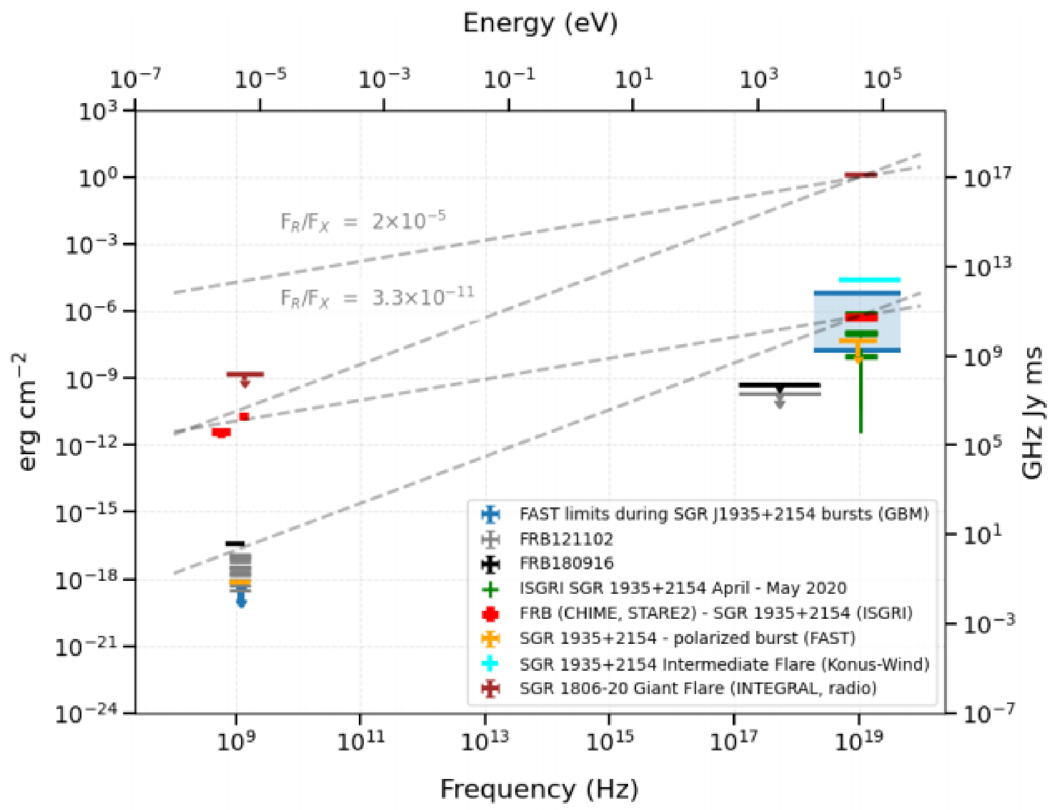

FIGURE 5.2: A comparison of the measured X-ray and radio measurements of SGR 1935+2154 compared to previous non-detections of related magnetars. The detection from CHIME and STARE2 are shown as red points. Dashed grey lines show flux ratios estimates. Figure taken from (Mereghetti, Savchenko, Ferrigno, Götz, et al., 2020a).

as the non-thermal modeling is still in its early stages (Halzen et al., 2005). As such, the detection of a smaller flare from SGR 1935+2154 is not in tension with our results but instead our result may help to constrain future non-thermal spectral modeling of the FRB emission mechanism that has come from this detection.

5.3 Potential Improvements to our Limits

Future VERITAS observations of FRBs can improve our limits significantly. There are currently observations that we are capable of but have not achieved. The principle one is 4 telescope ECM data recording simultaneously with a FRB. The reason for this discrepancy is that the current set up of the ECM only monitors a small portion of the VERITAS field view (2 pixels out of 49). Given the large error regions of non-localized FRBs, this means it is very unlikely that the portion of the sky monitored by the central pixel is the correct source position. The case of FRB

180916.J0158+65 demonstrates this. Prior to localization the highest probability location was at a position $\alpha \approx 01^{h}59^{m}, \delta \approx 65°49^{m}$ [2]. This was updated to $\alpha = 01^{h}58^{m}00.7502^{s} \pm 2.3$ mas , $\delta = 65°43'00.3142'' \pm 2.3$ mas when the EVN localized the FRB less than a year after its initial detection (Marcote et al., 2020). This slight difference of 0.14 degrees resulted in an off-pixel transient not being captured in the central pixel. Thus, although 4 telescope ECM data were collected during this run it did not overlap with the FRB.

The VERITAS data collected on FRB 121102 only involves the ECM on T1. This was the early stages of the ECM project, and later upgrades added optical monitoring capabilities to the other three telescopes. Having all four telescopes will improve the collecting area by a factor of 4, and allow the use of parallax to veto terrestrial transients and provide a more sensitive background rejection. This is currently a work in progress. VERITAS has the ability to collect 4-telescope ECM data, and as more repeaters continue to be localized to their host galaxies it becomes easier for VERITAS to ensure that these sources are contained within the monitored region of the FOV. It is expected in the upcoming season that VERITAS will collect 4-telescope ECM data for $\mathcal{O}(5)$ FRBs.

The limits presented in this thesis could also be improved if VERITAS were to collect simultaneous data for a galactic source because of the relative proximity of such a source. During the 2020 CHIME observation of SGR 1935+2154 bursts VERITAS was not operational due to COVID-19. CHIME observed one such event in two years of operation so this can act as a first estimate of the rate of galactic FRB-like events. H.E.S.S. triggered on this event through the GCN network[3]; a similar event would have triggered VERITAS had it been operational. Such an observation would have provided more constraining limits on the luminosity of the emission than what is presented here. The event rate of 0.5 events per year (from the one burst over two years) may also be reduced in the future due to dedicated radio follow-up campaigns of SGR bursts motivated by this detection, leading to non-CHIME detections of FRBs. Although observing a galactic source would be able to provide a deep luminosity limit, the burst attributed to the SGR was less luminous than typical FRBs

[2]https://www.chime-frb.ca/

[3]https://www.mpi-hd.mpg.de/hfm/HESS/pages/home/som/2020/06/

meaning that the limit of the gamma-ray to radio ratio may be worse (Margalit et al., 2020).

Chapter 6

Future Propsects and Conclusions

6.1 Future Studies

In this thesis it was shown that joint optical/gamma-ray observations are possible at VERITAS, and a program of observations was summarised. It was also shown that the ECM targets a unique parameter space with the ability to probe rapid optical transients. Although many observations can take advantage of just the rapid optical observations (projects like the asteroid occultation measurements to determine stellar radii), of particular interest are projects where the multi-wavelength capability of VERITAS can be leveraged. Fast Radio Bursts and related phenomena surrounding magnetars will be clear candidates for follow-up campaigns in the future, but there are also other understudied sources which are suspected to emit in the VHE and the optical regime.

One example are M-Dwarf flares. M-dwarfs are fully convective low mass main sequence stars. The fully convective nature of these stars gives them abnormally high magnetic fields which manifest as increased stellar activity. One of the properties of active M-dwarfs are bright, energetic "white light" flares. Unlike the typical M-dwarf spectra that peak deep into the IR these flares' spectra peak towards the UV. In the case of extreme flares, there is also expected to be VHE emission (Ohm et al., 2018). Flares from M-dwarfs have already been observed into the keV regime but remain undetected by Fermi-LAT or any major IACT (Osten et al., 2016). If IACTs are able to confirm VHE emission to be associated with flares from M-dwarfs then there will be major implications for the all-sky modeling of cosmic rays.

X-ray binaries also provide another potential source class to observe with VERITAS. HST observations in conjunction with RXTE data have shown that there exists flaring activity in these systems across the electromagnetic spectrum at sub-second timescales (Hynes et al., 2003). The poor timing resolutions of the previous optical measurements do not allow for an in-depth look at the optical structure of the flares. In addition, flares in micro-quasars have been observed to produce VHE gamma rays, such as in the Cygnus X-1 system (Albert et al., 2007). A high resolution optical/VHE study of the flares would be the first of its kind and is possible with the current generation of VERITAS.

6.2 Future VERITAS Upgrades

VERITAS has many potential upgrades that would allow for improvements to the joint optical/gamma-ray measurements. One of the most obvious VERITAS upgrades involves changing the FADCs to allow a precise current measurement without the ECM. Such an upgrade would allow for optical monitoring across the entire FOV. This would come with challenges in data processing and storage but the large FOV carries many benefits in background rejection/calibration. An expanded FOV would also allow for improved follow-up of poorly localized multi-messenger transients. The CHIME error region is large but still fully captured within the VERITAS FOV. Many of the repeaters still have not been well localized and having archival data of the full uncertainty region is the most promising way to ensure that an FRB is observed.

6.3 Future IACTs

In the near future the largest improvement on the limits in this analysis will arise from the construction of CTA, the Cherenkov Telescope Array (). CTA's construction has already started, with prototypes coming online as early as 2017 (CTA Consortium et al., 2019). A 10x increase of sensitivity is expected from the completed instrument compared to VERITAS. CTA will have two arrays, one in the southern hemisphere and one in the northern hemisphere. It will be composed of over 100 telescopes with an effective collecting area of over one million square meters. It will also expand the energy coverage compared to VERITAS, spanning from 20 GeV to 300 TeV. It is possible that the lower threshold may also benefit the sensitivity to FRBs if those sources have a soft spectra.

An optical program involving collaborators from H.E.S.S., VERITAS, and MAGIC is being developed for CTA. Source classes that will be under investigation will include all of the proposed sources in this thesis including FRBs. VERITAS does still carry an advantage over CTA in terms of location relative to CHIME. Since there is no comparable radio telescope near CTA, VERITAS will remain the only observatory that can probe the prompt emission of FRBs using simultaneous observations with CHIME.

6.4 Conclusion

The VERITAS telescope has new capabilities with the recent addition of the ECM to allow for joint optical/gamma-ray observations. Rapid transient phenomena in the optical regime remain under0studied and are of particular interest to the study of compact objects and non-thermal emission processes. In this thesis we have demonstrated the ability of VERITAS to perform such a study. We have outlined the techniques used to quantify and remove backgrounds. We also discussed the methods and technique's used to calibrate the ECM's flux, spectral response, and timing, and have demonstrated the techniques used in calculating prompt limits in the VHE. These techniques were used in the context of presenting the results of the VERITAS FRB campaign from 2016-2020. No significant VHE or optical emission was detected during this campaign and limits were set. VERITAS will continue to observe FRBs in both the optical and gamma-ray regime in the future to improve the limits presented in this paper. In addition to this, the flare detection analysis that was developed in the context of FRBs will find use in many projects involving phenomena ranging from meteors to X-ray binaries.

These novel observations will be useful not only in the future of VERITAS, as they explore many potential new source classes, but also for the optical program of the next generation of IACTs. In addition, upgrades to the VERITAS instrument itself may also improve the results of analyses similar to those presented here.

Appendix A

Matched Filtering

Here, the modified algorithm will be explained and some of the issues of the technique will be highlighted.

To begin, the conventional notation for Fourier transforms will be taken from (Allen et al., 2012), as follows. We start with a function $x(t)$ and:

$$\tilde{x}\left(f\right)=\int_{-\infty}^{\infty}x\left(t\right)e^{-2\pi ift}dt, \tag{A.1}$$

where $\tilde{x}\left(f\right)$ is the Fourier transform of $x\left(t\right)$. f is the frequency. One can show the continuous inverse Fourier transform can be represented as

$$x\left(t\right)=\int_{-\infty}^{\infty}\tilde{x}\left(f\right)e^{-2\pi ift}df. \tag{A.2}$$

In the following derivation of the matched filter we will use the continuous Fourier transform, but in the implementation we must use the discrete version. If we have points evenly spaced with a $1/\delta T$ sampling rate, then $x[j]=x(j\delta T)$ is the discrete version of x(t). Assuming N sample points $j=0,...,N-1$, with $\delta F=1/(N\delta T)$, we can then represent the discrete version of the forward and inverse Fourier transforms as:

$$\tilde{x}[k]=\delta T\sum_{j=0}^{N-1}x[j]e^{-2\pi ijk/N}, \tag{A.3}$$

$$x[j]=\delta F\sum_{k=0}^{N-1}\tilde{x}[k]e^{-2\pi ijk/N}. \tag{A.4}$$

As can clearly be seen by reference to the continuous Fourier transform, j acts as a time index and k acts as a frequency index. It should be noted that the above convention is normalized using the frequency and time spacing. This may differ from many fast Fourier transform (FFT) representations implemented in other discrete Fourier transform (DFT) packages.

Our data stream can be a represented as a function $s(t)$. This can be decomposed into signal and noise: $s(t) = n(t) + h(t)$ with $h(t)$ being the signal and $n(t)$ being a stationary Gaussian noise background. Assuming that we know the exact form of $h(t)$ we can also have a template $h_{temp}(t)$. The details of both the background and the signal will be discussed later, as these are critical in creating an accurate template. We can also define the power spectral density of the noise as follows:

$$< \tilde{n}(f)\tilde{n}^*(f') >= \frac{1}{2}S_n(|f|)\delta(f - f') \tag{A.5}$$

with S_n being the power spectral density. $\tilde{n}$ is the complex conjugate of the Fourier transform of the noise matrix. δ is a delta function.

The matched-filter output is of the form:

$$x(t_0) = 2\int_{-\infty}^{\infty} \frac{\tilde{s}(f)\tilde{h}^*_{template}(f)}{S_n(f)} df \tag{A.6}$$

where t_0 is the arrival time at the detector. The template will also implicitly depend on this t_0. Taking this implicit dependence we can rewrite the above formula:

$$x(t_0) = 4\mathbb{R}\int_{0}^{\infty} \frac{\tilde{s}(f)[\tilde{h}^*_{template}(f)]_{t_0=0}}{S_n(f)} e^{2\pi i f t_0} df, \tag{A.7}$$

$$z(t_0) = x_{re}(t) + ix_{im}(t_0)z(t_0) = 4\int_{0}^{\infty} \frac{\tilde{s}(f)[\tilde{h}^*_{template}(f)]_{t_0=0}}{S_n(f)} e^{2\pi i f t_0} df. \tag{A.8}$$

With $z(t_0)$ being the modulus of the complex filter. The amplitude of the SNR of the matched filter can be given by:

$$\rho(t) = \frac{|z(t)|}{\sigma} \tag{A.9}$$

with σ being a measure of the sensitivity of the instrument. This is constructed from the template and data by:

$$\sigma^2 = 4 \int_0^{\infty} \frac{|\tilde{h}_{template}(f)|^2}{S_n(f)} df \tag{A.10}$$

For purely stationary noise $< z^2(t) >$ will reduce to σ^2. For purely Gaussian noise, we expect most SNR to remain close to 1. So for transient event searches, a simple threshold on ρ will provide a list of event candidates with t_0 and SNRs.

Appendix B

Sky Maps

In this appendix the significance maps for the fast radio bursts studied with VERITAS are shown. Maps have been reduced to the central part of the VERITAS FOV. Black crosses mark the position of localized FRBs, whose position errors will be much smaller than the resolution of the images. Repeating FRBs monitored by CHIME have their error regions over-plotted as 10% contours in grey.

In addition, the significance distributions of the sky maps are also shown. In each case, a Gaussian fit to the histogram is over-plotted in black. The histograms have been normalized to have an area of 1.0.

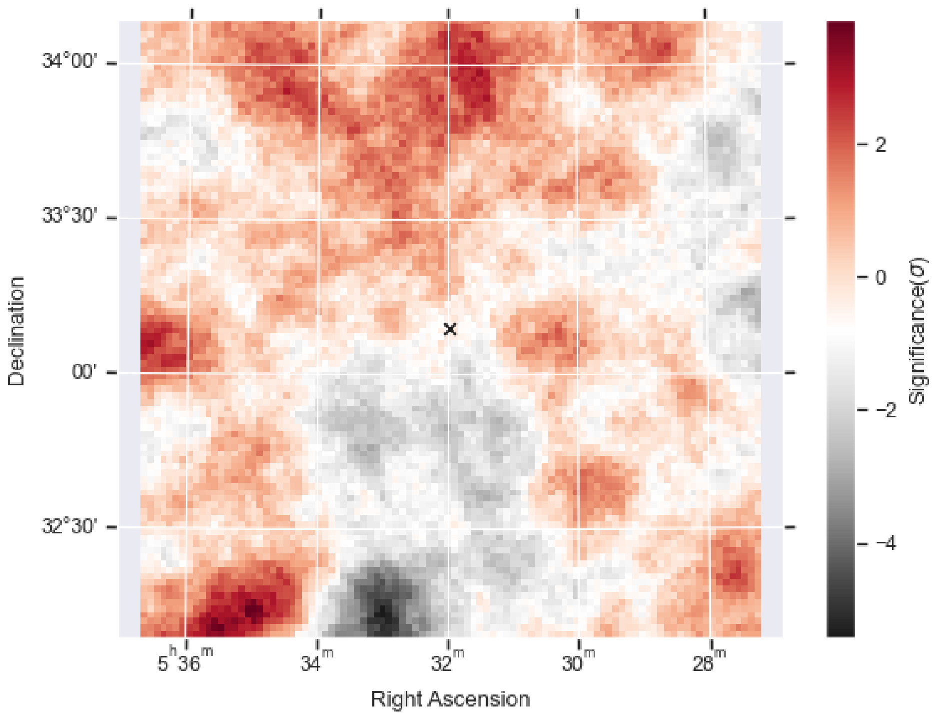

FIGURE B.1: Significance map of FRB 121102.

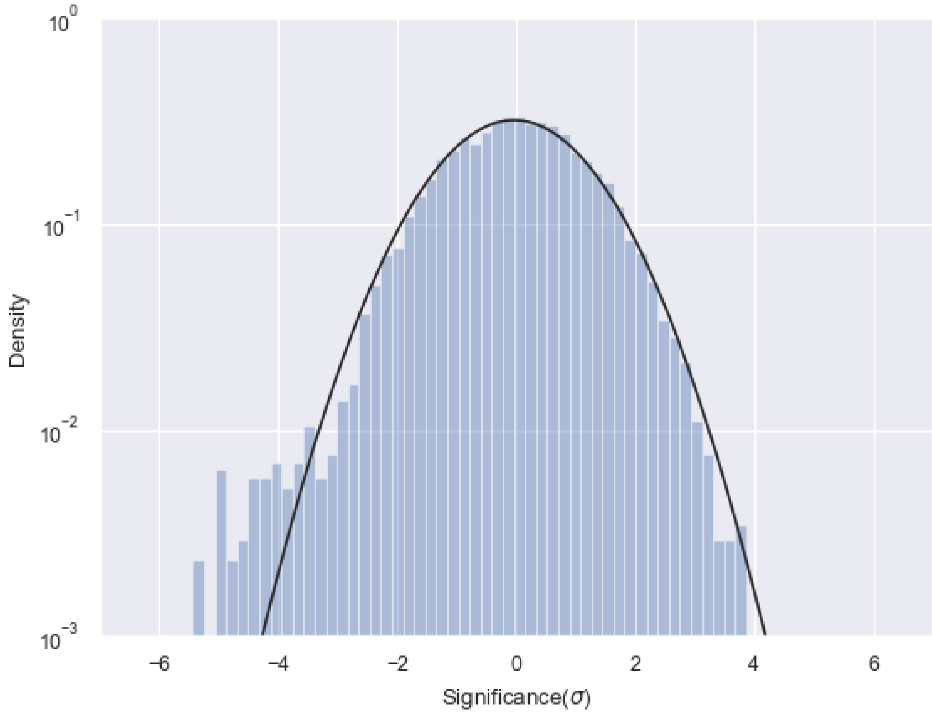

FIGURE B.2: Significance distribution of FRB 121102.

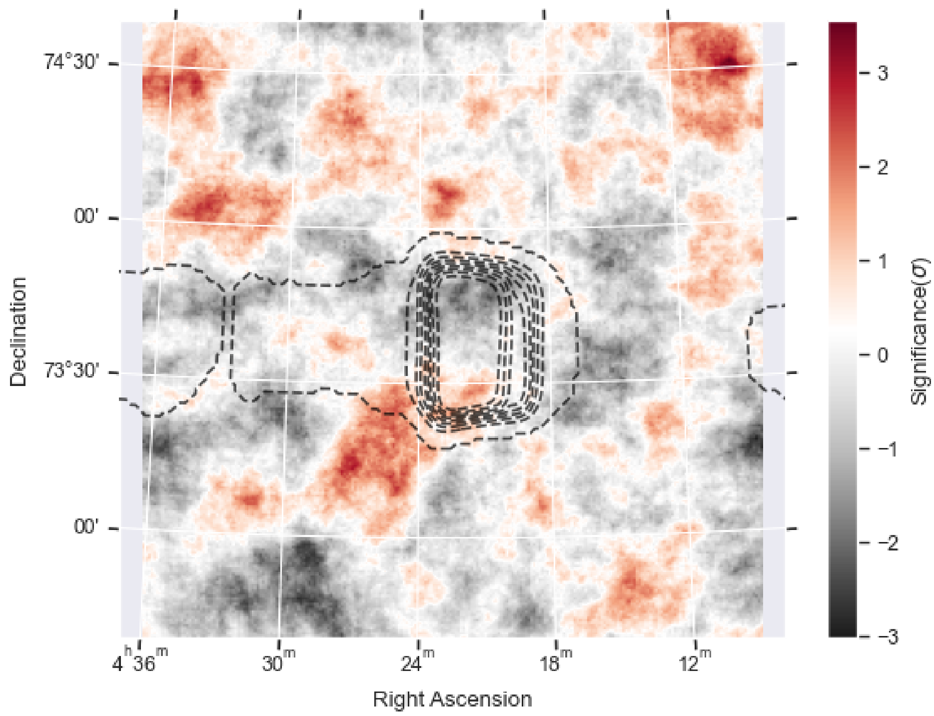

FIGURE B.3: Significance map of FRB 180814.J0422+73.

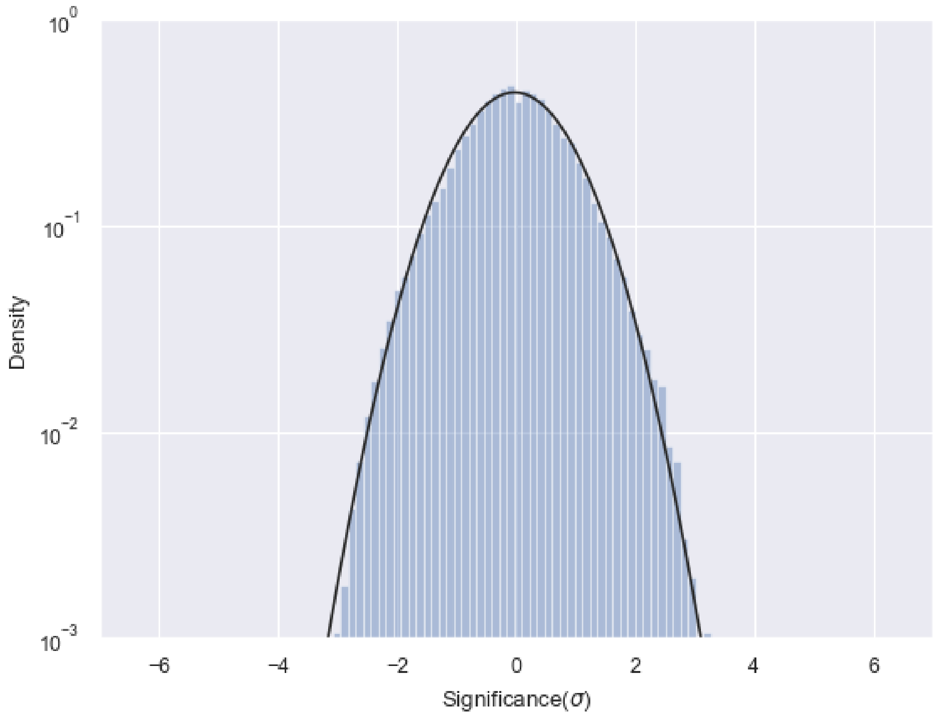

FIGURE B.4: Significance distribution of FRB 180814.J0422+73.

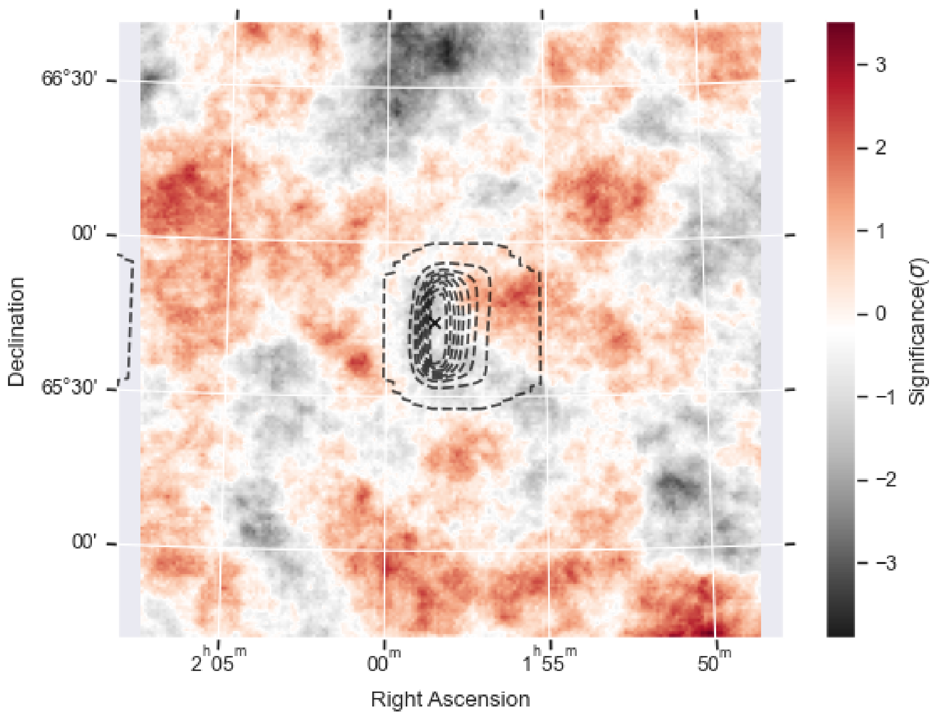

FIGURE B.5: Significance map of FRB 180916.J0158+65.

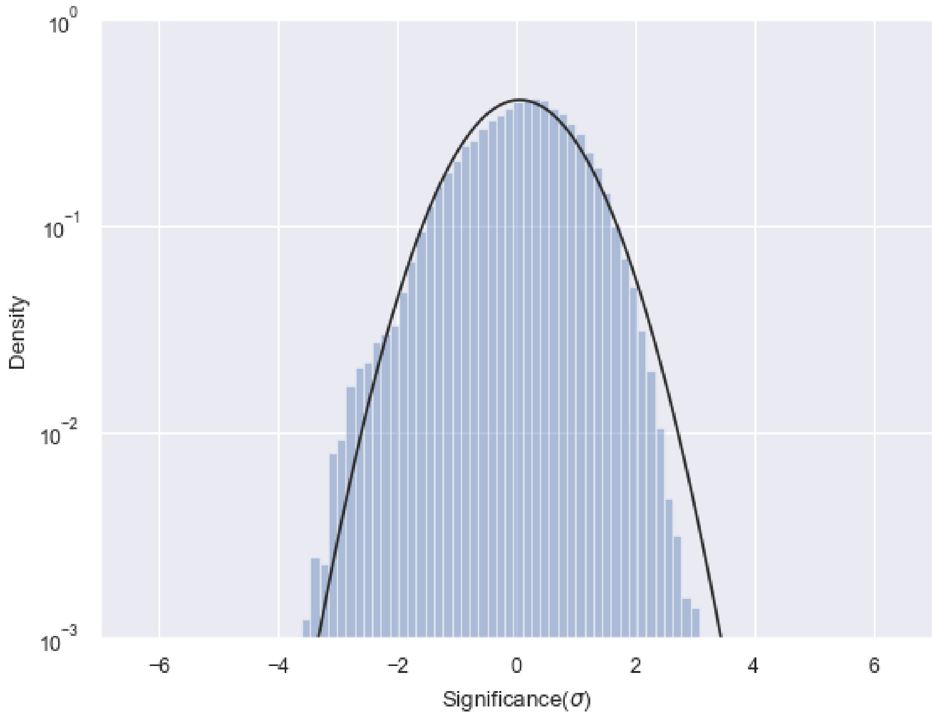

FIGURE B.6: Significance distribution of FRB 180916.J0158+65.

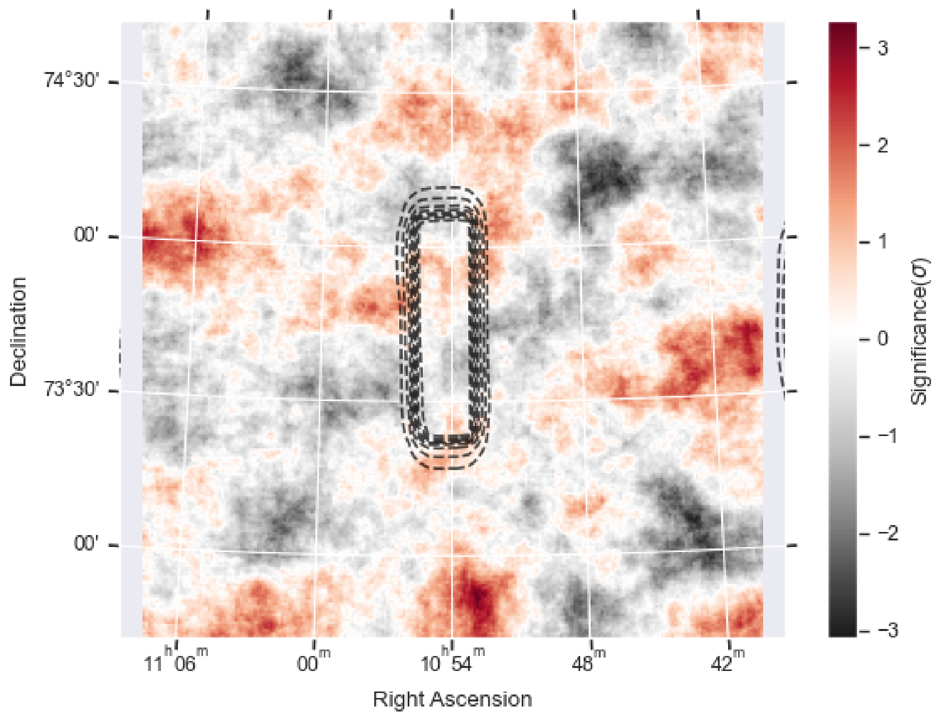

FIGURE B.7: Significance map of FRB 181030.J1054+73.

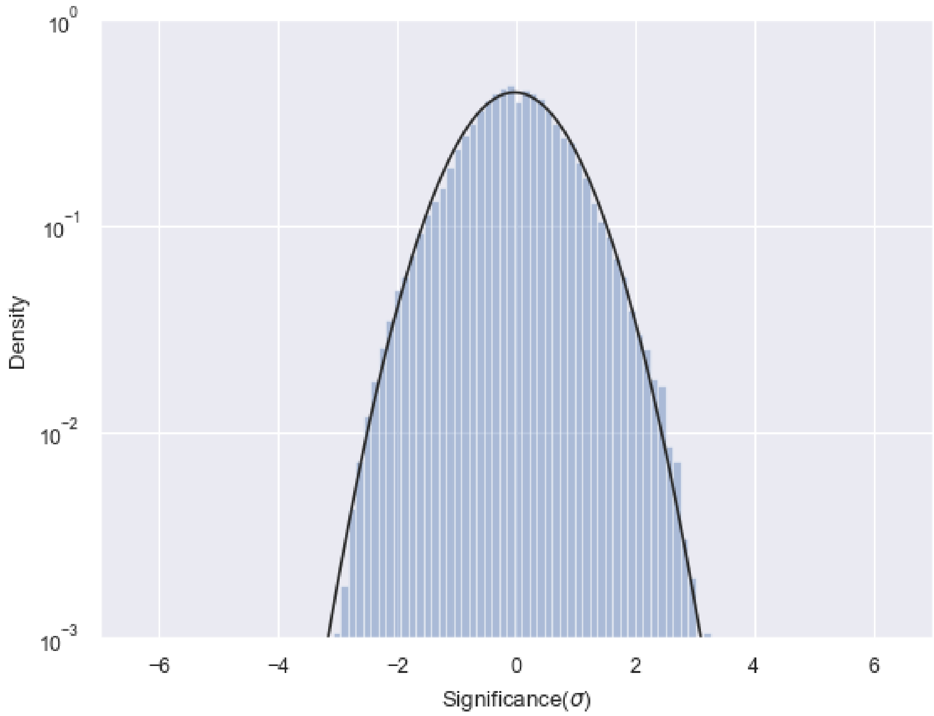

FIGURE B.8: Significance distribution of FRB 181030.J1054+73.

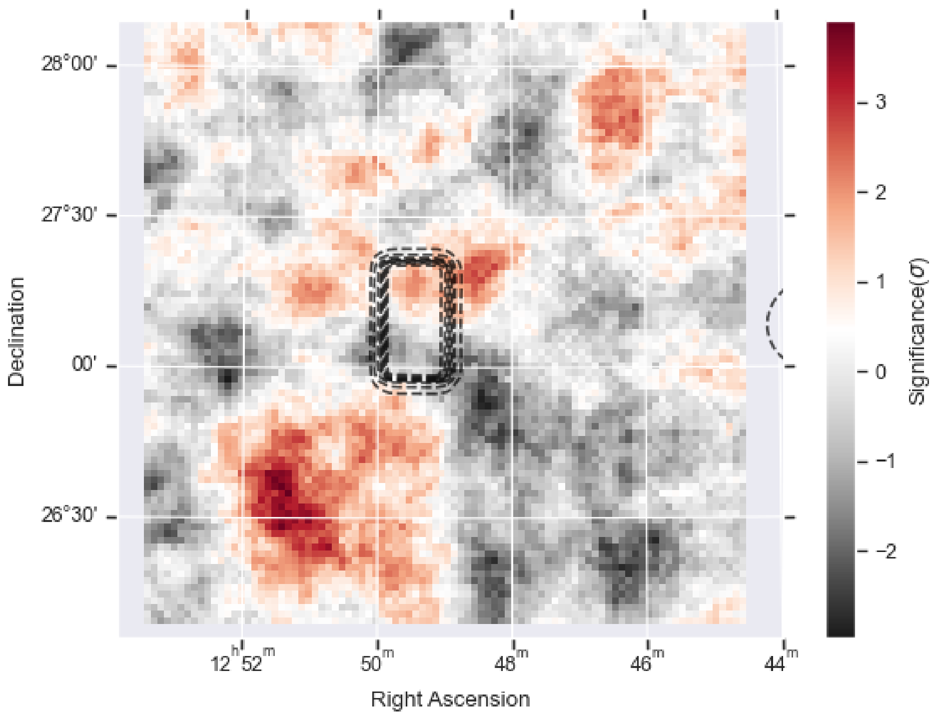

FIGURE B.9: Significance map of FRB 190116.J1249+27.

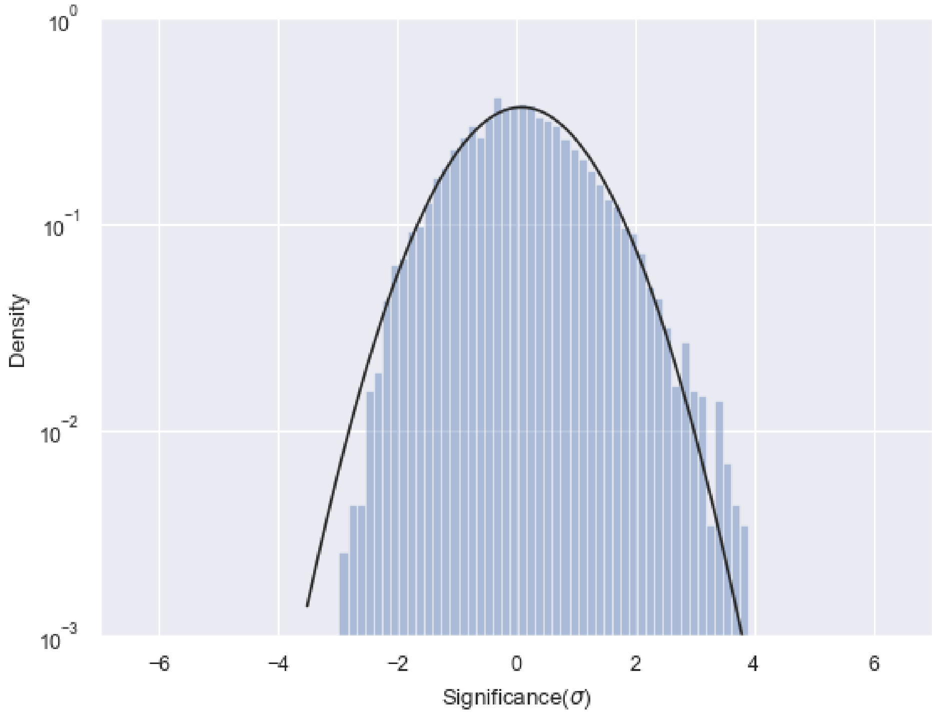

FIGURE B.10: Significance distribution of FRB 190116.J1249+27.

Bibliography

Aartsen, M. G. et al. (Feb. 2020). "A Search for MeV to TeV Neutrinos from Fast Radio Bursts with IceCube". In: ApJ 890.2, 111, p. 111. DOI: 10.3847/1538-4357/ab564b. arXiv: 1908.09997 [astro-ph.HE].

Abbott, B. P. et al. (Oct. 2017). "GW170817: Observation of Gravitational Waves from a Binary Neutron Star Inspiral". In: *Phys. Rev. Lett.* 119 (16), p. 161101. DOI: 10.1103/PhysRevLett.119.161101.

Abdalla, H. et al. (Nov. 2019). "A very-high-energy component deep in the γ-ray burst afterglow". In: Nature 575.7783, pp. 464–467. DOI: 10.1038/s41586-019-1743-9. arXiv: 1911.08961 [astro-ph.HE].

Abdollahi, S., F. Acero, et al. (Mar. 2020). "Fermi Large Area Telescope Fourth Source Catalog". In: ApJS 247.1, 33, p. 33. DOI: 10.3847/1538-4365/ab6bcb. arXiv: 1902.10045 [astro-ph.HE].

Abdollahi, S., M. Ackermann, et al. (Sept. 2017). "The Second Catalog of Flaring Gamma-Ray Sources from the Fermi All-sky Variability Analysis". In: ApJ 846.1, 34, p. 34. DOI: 10.3847/1538-4357/aa8092. arXiv: 1612.03165 [astro-ph.HE].

Albert, J. et al. (Aug. 2007). "Very High Energy Gamma-Ray Radiation from the Stellar Mass Black Hole Binary Cygnus X-1". In: ApJ 665.1, pp. L51–L54. DOI: 10.1086/521145. arXiv: 0706.1505 [astro-ph].

Aleksić, J. et al. (Jan. 2016). "The major upgrade of the MAGIC telescopes, Part I: The hardware improvements and the commissioning of the system". In: *Astroparticle Physics* 72, pp. 61–75. DOI: 10.1016/j.astropartphys.2015.04.004. arXiv: 1409.6073 [astro-ph.IM].

Allen, Bruce et al. (June 2012). "FINDCHIRP: An algorithm for detection of gravitational waves from inspiraling compact binaries". In: Phys. Rev. D 85.12, 122006, p. 122006. DOI: 10.1103/PhysRevD.85.122006. arXiv: gr-qc/0509116 [gr-qc].

Amiri, M., B. C. Andersen, K. M. Bandura, M. Bhardwaj, P. J. Boyle, C. Brar, P. Chawla, T. Chen, J. F. Cliche, D. Cubranic, M. Deng, N. T. Denman, M. Dobbs, F. Q. Dong, M. Fand ino, et al. (Jan. 2020a). "Periodic activity from a fast radio burst source". In: *arXiv e-prints*, arXiv:2001.10275, arXiv:2001.10275. arXiv: 2001.10275 [astro-ph.HE].

Amiri, M., B. C. Andersen, K. M. Bandura, M. Bhardwaj, P. J. Boyle, C. Brar, P. Chawla, T. Chen, J. F. Cliche, D. Cubranic, M. Deng, N. T. Denman, M. Dobbs, F. Q. Dong, M. Fandino, et al. (June 2020b). "Periodic activity from a fast radio burst source". In: Nature 582.7812, pp. 351–355. DOI: 10.1038/s41586-020-2398-2. arXiv: 2001.10275 [astro-ph.HE].

Amiri, M., K. Bandura, P. Berger, et al. (Aug. 2018). "The CHIME Fast Radio Burst Project: System Overview". In: ApJ 863.1, 48, p. 48. DOI: 10.3847/1538-4357/aad188. arXiv: 1803.11235 [astro-ph.IM].

Amiri, M., K. Bandura, M. Bhardwaj, P. Boubel, M. M. Boyce, Boyle, C. . Brar, et al. (Jan. 2019a). "A second source of repeating fast radio bursts". In: Nature 566.7743, pp. 235–238. DOI: 10.1038/s41586-018-0864-x. arXiv: 1901.04525 [astro-ph.HE].

Amiri, M., K. Bandura, M. Bhardwaj, P. Boubel, M. M. Boyce, Boyle, C. Brar, et al. (Jan. 2019b). "Observations of fast radio bursts at frequencies down to 400 megahertz". In: Nature 566.7743, pp. 230–234. DOI: 10.1038/s41586-018-0867-7. arXiv: 1901.04524 [astro-ph.HE].

Andersen, B. C., K. M. Bandura, et al. (2020). *A bright millisecond-duration radio burst from a Galactic magnetar*. arXiv: 2005.10324 [astro-ph.HE].

Andersen, B. C., K. Bandura, et al. (Nov. 2019). "CHIME/FRB Discovery of Eight New Repeating Fast Radio Burst Sources". In: ApJ 885.1, L24, p. L24. DOI: 10.3847/2041-8213/ab4a80. arXiv: 1908.03507 [astro-ph.HE].

Ansoldi, S. et al. (Aug. 2018). "The Blazar TXS 0506+056 Associated with a High-energy Neutrino: Insights into Extragalactic Jets and Cosmic-Ray Acceleration". In: ApJ 863.1, L10, p. L10. DOI: 10.3847/2041-8213/aad083. arXiv: 1807.04300 [astro-ph.HE].

Ashton, T. et al. (Mar. 2020). "A NECTAr-based upgrade for the Cherenkov cameras of the H.E.S.S. 12-meter telescopes". In: *Astroparticle Physics* 118, 102425,

p. 102425. DOI: 10.1016/j.astropartphys.2019.102425. arXiv: 2001.04510 [astro-ph.IM].

Astropy Collaboration et al. (Sept. 2018). "The Astropy Project: Building an Open-science Project and Status of the v2.0 Core Package". In: *aj* 156.3, 123, p. 123. DOI: 10.3847/1538-3881/aabc4f. arXiv: 1801.02634 [astro-ph.IM].

Atwood, W. B. et al. (June 2009). "The Large Area Telescope on the Fermi Gamma-Ray Space Telescope Mission". In: ApJ 697.2, pp. 1071–1102. DOI: 10.1088/0004-637X/697/2/1071. arXiv: 0902.1089 [astro-ph.IM].

Baiotti, Luca and Luciano Rezzolla (Sept. 2017). "Binary neutron star mergers: a review of Einstein's richest laboratory". In: *Reports on Progress in Physics* 80.9, 096901, p. 096901. DOI: 10.1088/1361-6633/aa67bb. arXiv: 1607.03540 [gr-qc].

Benbow, W. et al. (Apr. 2019). "Direct measurement of stellar angular diameters by the VERITAS Cherenkov telescopes". In: *Nature Astronomy* 3, pp. 511–516. DOI: 10.1038/s41550-019-0741-z. arXiv: 1904.06324 [astro-ph.SR].

Bessell, M. S. (Oct. 1990). "UBVRI passbands." In: PASP 102, pp. 1181–1199. DOI: 10.1086/132749.

Binney, James and Michael Merrifield (1998). *Galactic Astronomy*. Princeton: Princeton University Press.

Bochenek, Christopher D. et al. (2020). *A fast radio burst associated with a Galactic magnetar*. arXiv: 2005.10828 [astro-ph.HE].

Cano, Zach et al. (Jan. 2017). "The Observer's Guide to the Gamma-Ray Burst Supernova Connection". In: *Advances in Astronomy* 2017, 8929054, p. 8929054. DOI: 10.1155/2017/8929054. arXiv: 1604.03549 [astro-ph.HE].

Chen, Ge, Vikram Ravi, and Wenbin Lu (July 2020). "The Multiwavelength Counterparts of Fast Radio Bursts". In: *The Astrophysical Journal* 897.2, p. 146. ISSN: 1538-4357. DOI: 10.3847/1538-4357/ab982b.

Chernitsky, Gabriel (2017). "Search for fast optical transients using archival VERITAS data". PhD thesis. McGill University.

Cook, A. F. et al. (Dec. 1980). "Flux of optical meteors down to M_{PG} = +12". In: MNRAS 193, pp. 645–666. DOI: 10.1093/mnras/193.3.645.

Cordes, James M. and Shami Chatterjee (2019). "Fast Radio Bursts: An Extragalactic Enigma". In: *Annual Review of Astronomy and Astrophysics* 57.1, pp. 417–465. DOI: 10.1146/annurev-astro-091918-104501.

Crawford, F. et al. (May 2016). "A search for highly dispersed fast radio bursts in three Parkes multibeam surveys". In: *Monthly Notices of the Royal Astronomical Society* 460.3, pp. 3370–3375. ISSN: 1365-2966. DOI: 10.1093/mnras/stw1233. URL: http://dx.doi.org/10.1093/mnras/stw1233.

CTA Consortium and Rene A. Ong (Sept. 2019). "The Cherenkov Telescope Array Science Goals and Current Status". In: *European Physical Journal Web of Conferences*. Vol. 209. European Physical Journal Web of Conferences, p. 01038. DOI: 10.1051/epjconf/201920901038. arXiv: 1904.12196 [astro-ph.HE].

Dai, Z. G. (July 2020). "A Magnetar-asteroid Impact Model for FRB 200428 Associated with an X-Ray Burst from SGR 1935+2154". In: *The Astrophysical Journal* 897.2, p. L40. ISSN: 2041-8213. DOI: 10.3847/2041-8213/aba11b. URL: http://dx.doi.org/10.3847/2041-8213/aba11b.

Dai, Z. G. et al. (Sept. 2016). "Repeating Fast Radio Bursts from Highly Magnetized Pulsars Traveling through Asteroid Belts". In: ApJ 829.1, 27, p. 27. DOI: 10.3847/0004-637X/829/1/27. arXiv: 1603.08207 [astro-ph.HE].

Davies, John M. and Eugene S. Cotton (Apr. 1957). "Design of the quartermaster solar furnace". In: *Solar Energy* 1.2-3, pp. 16–22. DOI: 10.1016/0038-092X(57)90116-0.

de Naurois, M. and H. E. S. S. Collaboration (Aug. 2019). "GRB190829A: Detection of VHE gamma-ray emission with H.E.S.S." In: *GRB Coordinates Network* 25566, p. 1.

Deil, C. et al. (Mar. 2009). "Capability of Cherenkov telescopes to observe ultra-fast optical flares". In: *Astroparticle Physics* 31.2, pp. 156–162. DOI: 10.1016/j.astropartphys.2008.12.008. arXiv: 0812.3966 [astro-ph].

DeLaunay, J. J. et al. (Nov. 2016). "DISCOVERY OF A TRANSIENT GAMMA-RAY COUNTERPART TO FRB 131104". In: *The Astrophysical Journal* 832.1, p. L1. ISSN: 2041-8213. DOI: 10.3847/2041-8205/832/1/l1. URL: http://dx.doi.org/10.3847/2041-8205/832/1/L1.

Feldman, Gary J. and Robert D. Cousins (Apr. 1998). "Unified approach to the classical statistical analysis of small signals". In: Phys. Rev. D 57.7, pp. 3873–3889. DOI: 10.1103/PhysRevD.57.3873. arXiv: physics/9711021 [physics.data-an].

Geng, Jin-Jun et al. (2020). *FRB 200428: an Impact between an Asteroid and a Magnetar*. arXiv: 2006.04601 [astro-ph.HE].

Göttgens, Fabian et al. (June 2019). "Discovery of an old nova remnant in the Galactic globular cluster M 22". In: A&A 626, A69, A69. DOI: 10.1051/0004-6361/201935221. arXiv: 1904.11515 [astro-ph.SR].

Griffin, Sean (2011). "VERy TRenDy:The VERITAS Transient Detector". PhD thesis. McGill University.

H. E. S. S. Collaboration, H. Abdalla, A. Abramowski, F. Aharonian, F. Ait Benkhali, A. G. Akhperjanian, T. Andersson, et al. (Jan. 2017). "First limits on the very-high energy gamma-ray afterglow emission of a fast radio burst. H.E.S.S. observations of FRB 150418". In: A&A 597, A115, A115. DOI: 10.1051/0004-6361/201629117. arXiv: 1611.09209 [astro-ph.HE].

H. E. S. S. Collaboration, H. Abdalla, A. Abramowski, F. Aharonian, F. Ait Benkhali, A. G. Akhperjanian, E. O. Angüner, et al. (Apr. 2018). "Extended VHE γ-ray emission towards SGR1806-20, LBV 1806-20, and stellar cluster Cl* 1806-20". In: A&A 612, A11, A11. DOI: 10.1051/0004-6361/201628695. arXiv: 1606.05404 [astro-ph.HE].

Halzen, Francis, Hagar Landsman, and Teresa Montaruli (Mar. 2005). "TeV photons and Neutrinos from giant soft-gamma repeaters flares". In: *arXiv e-prints*, astro-ph/0503348, astro–ph/0503348. arXiv: astro-ph/0503348 [astro-ph].

Hamamatsu Photonics (2007). *Photomultiplier Tubes, Basics and Applications*. 3rd ed.

Hanna, D. et al. (Jan. 2010). "An LED-based flasher system for VERITAS". In: *Nuclear Instruments and Methods in Physics Research A* 612.2, pp. 278–287. DOI: 10.1016/j.nima.2009.10.107. arXiv: 0911.2015 [astro-ph.IM].

Hassan, T. et al. (Jan. 2017). "MAGIC sensitivity to millisecond-duration optical pulses". In: *35th International Cosmic Ray Conference (ICRC2017)*. Vol. 301. International Cosmic Ray Conference, p. 807. arXiv: 1708.07698 [astro-ph.IM].

Helstrom, Carl W. (1968). *Statistical theory of signal detection*. 2nd. Pergamon Press.

Hnatyk, B. et al. (Sept. 2020). "High-energy and very high-energy gamma-ray emission from the magnetar SGR 1900+14 neighbourhood". In: *arXiv e-prints*, arXiv:2009.06081, arXiv:2009.06081. arXiv: 2009.06081 [astro-ph.HE].

Holder, J. et al. (July 2006). "The first VERITAS telescope". In: *Astroparticle Physics* 25.6, pp. 391–401. DOI: 10.1016/j.astropartphys.2006.04.002. arXiv: astro-ph/0604119 [astro-ph].

Hynes, R. I. et al. (Oct. 2003). "The remarkable rapid X-ray, ultraviolet, optical and infrared variability in the black hole XTE J1118+480". In: MNRAS 345.1, pp. 292–310. DOI: 10.1046/j.1365-8711.2003.06938.x. arXiv: astro-ph/0306626 [astro-ph].

IceCube Collaboration et al. (Oct. 2006). "First year performance of the IceCube neutrino telescope". In: *Astroparticle Physics* 26.3, pp. 155–173. DOI: 10.1016/j.astropartphys.2006.06.007. arXiv: astro-ph/0604450 [astro-ph].

Ivezić, Ž. et al. (Mar. 2019). "LSST: From Science Drivers to Reference Design and Anticipated Data Products". In: ApJ 873, 111, p. 111. DOI: 10.3847/1538-4357/ab042c. arXiv: 0805.2366.

Jelley, John V. (1958). *Cerenkov radiation and its applications*. Pergamon Press.

Klebesadel, Ray W., Ian B. Strong, and Roy A. Olson (June 1973). "Observations of Gamma-Ray Bursts of Cosmic Origin". In: ApJ 182, p. L85. DOI: 10.1086/181225.

Li, T. and Y. Ma (Sept. 1983). "Analysis methods for results in gamma-ray astronomy." In: ApJ 272, pp. 317–324. DOI: 10.1086/161295.

Lin, L. et al. (May 2020). "Stringent upper limits on pulsed radio emission during an active bursting phase of the Galactic magnetar SGRJ1935+2154". In: *arXiv e-prints*. arXiv: 2005.11479 [astro-ph.HE].

Li et al. (May 2020). "Identification of a non-thermal X-ray burst with the Galactic magnetar SGR 1935+2154 and a fast radio burst with Insight-HXMT". In: *arXiv e-prints*, arXiv:2005.11071, arXiv:2005.11071. arXiv: 2005.11071 [astro-ph.HE].

Lorimer, D. R. et al. (2007). "A Bright Millisecond Radio Burst of Extragalactic Origin". In: *Science* 318.5851, pp. 777–780. ISSN: 0036-8075. DOI: 10.1126/science.1147532.

MAGIC Collaboration, V. A. Acciari, S. Ansoldi, L. A. Antonelli, A. Arbet Engels, C. Arcaro, et al. (Dec. 2018). "Constraining very-high-energy and optical emission from FRB 121102 with the MAGIC telescopes". In: MNRAS 481.2, pp. 2479–2486. DOI: 10.1093/mnras/sty2422. arXiv: 1809.00663 [astro-ph.HE].

MAGIC Collaboration, V. A. Acciari, S. Ansoldi, L. A. Antonelli, A. Arbet Engels, D. Baack, et al. (Nov. 2019). "Teraelectronvolt emission from the γ-ray burst GRB 190114C". In: Nature 575.7783, pp. 455–458. DOI: 10.1038/s41586-019-1750-x.

MAGIC Collaboration, V. A. Acciari, S. Ansoldi, L. A. Antonelli, A. Arbet Engels, et al. (Nov. 2019). "Observation of inverse Compton emission from a long γ-ray burst". In: Nature 575.7783, pp. 459–463. DOI: 10.1038/s41586-019-1754-6.

Marcote, B. et al. (Jan. 2020). "A repeating fast radio burst source localized to a nearby spiral galaxy". In: Nature 577.7789, pp. 190–194. DOI: 10.1038/s41586-019-1866-z. arXiv: 2001.02222 [astro-ph.HE].

Margalit, Ben et al. (May 2020). "Implications of a "Fast Radio Burst" from a Galactic Magnetar". In: *arXiv e-prints*. arXiv: 2005.05283 [astro-ph.HE].

Martone, R. et al. (Nov. 2019). "A cumulative search for hard X/γ-ray emission associated with fast radio bursts in Fermi/GBM data". In: A&A 631, A62, A62. DOI: 10.1051/0004-6361/201936284. arXiv: 1909.07165 [astro-ph.HE].

Mereghetti, S., V. Savchenko, C. Ferrigno, D. Götz, et al. (Aug. 2020a). "INTEGRAL Discovery of a Burst with Associated Radio Emission from the Magnetar SGR 1935+2154". In: ApJ 898.2, L29, p. L29. DOI: 10.3847/2041-8213/aba2cf. arXiv: 2005.06335 [astro-ph.HE].

Mereghetti, S., V. Savchenko, C. Ferrigno, D. Götz, et al. (2020b). *INTEGRAL discovery of a burst with associated radio emission from the magnetar SGR 1935+2154*. arXiv: 2005.06335 [astro-ph.HE].

Metzger, Brian D., Edo Berger, and Ben Margalit (May 2017). "Millisecond Magnetar Birth Connects FRB 121102 to Superluminous Supernovae and Long-duration Gamma-Ray Bursts". In: *The Astrophysical Journal* 841.1, p. 14. ISSN: 1538-4357. DOI: 10.3847/1538-4357/aa633d. URL: http://dx.doi.org/10.3847/1538-4357/aa633d.

Michilli, D. et al. (Jan. 2018). "An extreme magneto-ionic environment associated with the fast radio burst source FRB 121102". In: *Nature* 553.7687, pp. 182–185. ISSN: 1476-4687. DOI: 10.1038/nature25149. URL: http://dx.doi.org/10.1038/nature25149.

Nicholl, M. et al. (July 2017). "Empirical Constraints on the Origin of Fast Radio Bursts: Volumetric Rates and Host Galaxy Demographics as a Test of Millisecond Magnetar Connection". In: *The Astrophysical Journal* 843.2, p. 84. ISSN: 1538-4357. DOI: 10.3847/1538-4357/aa794d. URL: http://dx.doi.org/10.3847/1538-4357/aa794d.

Ohm, S. and C. Hoischen (Feb. 2018). "On the expected γ-ray emission from nearby flaring stars". In: MNRAS 474, pp. 1335–1341. DOI: 10.1093/mnras/stx2806. arXiv: 1710.09385 [astro-ph.HE].

Osten, R. A. et al. (Dec. 2016). "A Very Bright, Very Hot, and Very Long Flaring Event from the M Dwarf Binary System DG CVn". In: ApJ 832, 174, p. 174. DOI: 10.3847/0004-637X/832/2/174. arXiv: 1609.04674 [astro-ph.SR].

Perkins, Jeremy S., Gernot Maier, and The VERITAS Collaboration (Dec. 2009). "VERITAS Telescope 1 Relocation: Details and Improvements". In: *arXiv e-prints*. arXiv: 0912.3841 [astro-ph.IM].

Petroff, E., E. D. Barr, et al. (Sept. 2016). "FRBCAT: The Fast Radio Burst Catalogue". In: PASA 33, e045, e045. DOI: 10.1017/pasa.2016.35. arXiv: 1601.03547 [astro-ph.HE].

Petroff, E., J. W. T. Hessels, and D. R. Lorimer (May 2019). "Fast radio bursts". In: A&A Rev. 27.1, 4, p. 4. DOI: 10.1007/s00159-019-0116-6. arXiv: 1904.07947 [astro-ph.HE].

Petroff, E., E. F. Keane, et al. (Aug. 2015). "Identifying the source of perytons at the Parkes radio telescope". In: MNRAS 451.4, pp. 3933–3940. DOI: 10.1093/mnras/stv1242. arXiv: 1504.02165 [astro-ph.IM].

Platts, E. et al. (Aug. 2019). "A living theory catalogue for fast radio bursts". In: *Physics Reports* 821, pp. 1–27. ISSN: 0370-1573. DOI: 10.1016/j.physrep.2019.06.003. URL: http://dx.doi.org/10.1016/j.physrep.2019.06.003.

Rhodes, L. et al. (Apr. 2020). "Radio Afterglows of Very High Energy Gamma-Ray Bursts 190829A and 180720B". In: *arXiv e-prints*. arXiv: 2004.01538 [astro-ph.HE].

Ridnaia, A. et al. (2020). *A peculiar hard X-ray counterpart of a Galactic fast radio burst*. arXiv: 2005.11178 [astro-ph.HE].

Shannon, R. M. and V. Ravi (Mar. 2017). "Radio-interferometric Monitoring of FRB 131104: A Coincident AGN Flare, but No Evidence for a Cosmic Fireball". In: *The*

Astrophysical Journal 837.2, p. L22. ISSN: 2041-8213. DOI: 10.3847/2041-8213/aa62fb. URL: http://dx.doi.org/10.3847/2041-8213/aa62fb.

Spitler, L. G. et al. (Aug. 2014). "Fast Radio Burst Discovered in the Arecibo Pulsar ALFA Survey". In: *ApJ* 790.2, 101, p. 101. DOI: 10.1088/0004-637X/790/2/101. arXiv: 1404.2934 [astro-ph.HE].

The LIGO Scientific Collaboration et al. (Aug. 2019). "A gravitational-wave measurement of the Hubble constant following the second observing run of Advanced LIGO and Virgo". In: *arXiv e-prints*, arXiv:1908.06060, arXiv:1908.06060. arXiv: 1908.06060 [astro-ph.CO].

Thornton, D. et al. (July 2013). "A Population of Fast Radio Bursts at Cosmological Distances". In: *Science* 341.6141, pp. 53–56. ISSN: 1095-9203. DOI: 10.1126/science.1236789. URL: http://dx.doi.org/10.1126/science.1236789.

Veres, P. et al. (Nov. 2019). "Observation of inverse Compton emission from a long γ-ray burst". In: *Nature* 575.7783, pp. 459–463. ISSN: 1476-4687. DOI: 10.1038/s41586-019-1754-6. URL: http://dx.doi.org/10.1038/s41586-019-1754-6.

von Kienlin, A. et al. (Apr. 2020). "The Fourth Fermi-GBM Gamma-Ray Burst Catalog: A Decade of Data". In: ApJ 893.1, 46, p. 46. DOI: 10.3847/1538-4357/ab7a18. arXiv: 2002.11460 [astro-ph.HE].

Weekes, Trevor (2003). *Very High Energy Gamma-Ray Astronomy*. CRC Press.

Wenger, M. et al. (Apr. 2000). "The SIMBAD astronomical database. The CDS reference database for astronomical objects". In: A&AS 143, pp. 9–22. DOI: 10.1051/aas:2000332. arXiv: astro-ph/0002110 [astro-ph].

Xi, Shao-Qiang et al. (June 2017). "Search for GeV Counterparts to Fast Radio Bursts with Fermi". In: ApJ 842.1, L8, p. L8. DOI: 10.3847/2041-8213/aa74cf. arXiv: 1705.03657 [astro-ph.HE].

Yamasaki, Shotaro, Tomonori Totani, and Norita Kawanaka (Aug. 2016). "A blind search for prompt gamma-ray counterparts of fast radio bursts with Fermi-LAT data". In: MNRAS 460.3, pp. 2875–2880. DOI: 10.1093/mnras/stw1206. arXiv: 1604.03077 [astro-ph.HE].

Yang, Yu-Han, Bin-Bin Zhang, and Bing Zhang (Apr. 2019). "Second Repeating FRB 180814.J0422+73: Ten-year Fermi-LAT Upper Limits and Implications". In: ApJ 875.2, L19, p. L19. DOI: 10.3847/2041-8213/ab13af. arXiv: 1903.07329 [astro-ph.HE].

Younes, George et al. (Mar. 2016). "FERMI/Gamma-ray Burst Monitor upper limits assuming a magnetar origin for the repeating Fast Radio Burst source, FRB 121102". In: *The Astronomer's Telegram* 8781, p. 1.

Zhang, Bin-Bin and Bing Zhang (July 2017). "Repeating FRB 121102: Eight-year Fermi-LAT Upper Limits and Implications". In: ApJ 843.1, L13, p. L13. DOI: `10.3847/2041-8213/aa7633`. arXiv: `1705.04242 [astro-ph.HE]`.

Zhang, Bing and Peter Mészáros (Jan. 2004). "Gamma-Ray Bursts: progress, problems & prospects". In: *International Journal of Modern Physics A* 19.15, pp. 2385–2472. DOI: `10.1142/S0217751X0401746X`. arXiv: `astro-ph/0311321 [astro-ph]`.